7-31-2018

Electrocatalytic Properties of Ni-Fe BasedAlloys Toward Oxygen Evolution Reaction

Xiaodan Cui
Louisiana State University and Agricultural and Mechanical College

ELECTROCATALYTIC PROPERTIES OF Ni-Fe BASED ALLOYS TOWARD OXYGEN EVOLUTION REACTION

A Dissertation

Submitted to the Graduate Faculty of the
Louisiana State University and
Agricultural and Mechanical College
in partial fulfillment of
the requirements for the degree of
Doctor of Philosophy

in

The Department of Mechanical and Industrial Engineering

by
Xiaodan Cui
B.S. Tianjin University, 2012
M.S. University of Illinois at Chicago, 2015
December 2018

ACKNOWLEDGMENTS

First of all, I would like to extend my deepest gratitude to my advisor, Dr. Shengmin Guo, for his selfless help and encouragement when I was in difficulties. I am so inspired by his profound knowledge and noble personality, which guide me to become a better person.

Next, I would like to extend my gratitude to my committee members Dr. Dorel Modolvan, Dr. Thomas Corbitt and Dr. Manas Gartia. I greatly appreciate the financial support for this research by NSF EPSCoR CIMM. Also I would like to express my thanks to my collaborators: Dr. Boliang Zhang, Hong Yao, Congyuan Zeng, Hao Wen and Ali Hemmasian.

At last, I would like to express gratitude to my beloved families: my parents, Mr. and Mrs. Jianhui Cui and Qiuzhi Zhao, my parents-in-law, Mr. and Mrs. Huijun Wang and Xifeng Tan, and my late grandmother, Mrs. Guimin Zhang. Foremost, I would like express my gratitude to my husband, Dr. Zi Wang, for his understanding and love in the past ten years.

TABLE OF CONTENTS

LIST OF TABLES

LIST OF FIGURES

ABSTRACT

In this dissertation, laser-based manufacturing was applied to develop NiFe-based alloys, with focus on their electrochemical characteristics toward oxygen evolution reaction during water electrocatalysis. The targeted electrocatalysts were designed by combining catalysis principles of absorption energy, electronic effect and geometry effect. Firstly, a one-step laser-based manufacturing method was applied to prepare a thin layer of NiFe-based electrodes with varied Ni to Fe ratios to replace high-cost noble metals as the electrocatalyst for oxygen evolution reaction (OER). Since each Ni has 0.6 d-vacancy and each Fe atom has 2.2 d-vacancies. The alloying of Ni-Fe allows electrons flowing from Ni to Fe, causing the increase of d-vacancy, resulting in a catalyst matching better to the reaction electron transfer coordination. The formation of ultra-small secondary $FeNi_3$ phases effectively increased active sites, as well as the average lattice spacing to match better with the geometries of species involved in OER reactions. Secondly, laser processed alloys usually experience special thermal cycles that could produce anisotropic and heterogeneous microstructures significantly different from parts made by traditional casting. The electrocatalytic performances of laser-processed alloys differ significantly from traditionally processed alloys and provide interesting insights on novel electrocatalyst. The laser processed Ni-Fe alloys are prepared by varied laser scanning speeds as the electrocatalyst toward OER. In addition Ni-Fe alloys prepared by arc melting and spark plasma sintering are also prepared for comparison. Thirdly, monolithic nanoporous NiFe electrocatalyst is developed by dealloying $Ni_6Fe_4Al_{10}$ prepared by laser-based manufacturing for the first time. The resulted nanoscale pores provided high surface areas and more active sites for catalytic reactions, while the microscale pores provided sufficient channels for gas and ion diffusion. Compared to the bulk NiFe electrode, the nanoporous NiFe electrode exhibits an improved electrocatalytic activity. At last, Ni, Fe based high entropy alloys (HEAs), including FeNiMnCrCu and FeCoNiCrAl, were synthesized via arc melting and their electrochemical performance was studied. Due to the varied atomic radius and structure configurations of the elements in an HEA, the lattice parameters in the crystalline are usually seriously distorted and severe defects exist in the lattice with changed valence electron concentration, which are advantageous properties for catalyst performance.

1 OVERVIEW

1.1 Motivations

Nowadays, due to the fast development of technology and rapid consumption of fossil fuels, the exploration of renewable and clean energy sources becomes more urgent.[1-5] Hydrogen, as a highly sustainable and dense specific energy carrier, has long been considered as an excellent replacement for fossil fuels. Electrochemical water splitting is one of the most attractive methods for hydrogen generation since it can be achieved at a large scale with water as a convenient raw material.[6-8] However, due to the sluggish reaction kinetics of oxygen evolution reaction (OER), electrochemical water splitting requires high overpotentials. It's well known that lowering down overpotentials can effectively increase the water electrolysis efficiency.[9] To convert electrical energy to chemical energy stored in hydrogen efficiently, an electrocatalyst with excellent electrocatalytic activity toward OER is of high demand[10-12]. Currently, noble metal-based electrocatalyst, such as Iridium and ruthenium are still dominating OER electrocatalys.[13-14] The high activity of noble metals is attributed to their empty d orbitals, leading to the s, p, d band hybridization and a high d band occupancy. Also, the minimum energy required to transmit an electron from the top edge of the Fermi level into vacuum (work function) of noble metals is higher than that of transition metals, which allows a higher potential to accept electrons for donor reactions such as OER. In addition, the lattice spacing of those noble elements matches better with OER process species. For example, the lattice spacing of the Rh {111} plane is 0.268 nm, Ir is 0.270 nm, very close to the optimal spacing for M-OH formation and O-O desorption (in the range of 0.250 nm to 0.280 nm). Nevertheless, the commercialization of water splitting is severely hindered by the scarcity and high cost of the noble materials.

Recently, more and more effort has been devoted to explore low-cost electrocatalyst materials, especially those earth-abundant and eco-friendly materials [15-17]. Among these materials, Ni stands out as the most promising candidate.[18-21] This is because d character factor (d%, the percent of d orbitals in the s, p, d or d, s, p hybridization orbitals), work function and crystal structure of Ni are most similar to noble metals, as well as its top position on the volcano plot of catalytic activity vs. the absorption energy of adsorbed atomic oxygen among all transition metals. It is also discovered that the reactant, product and intermediate absorption affinities on Ni can be effectively altered by combining with Fe. This alloying process can significantly improve the performance of Ni[11, 19]. This is because each Ni has 0.6 d-vacancy; each Fe atom has 2.2 d-vacancies. The alloying of Ni-Fe will allow electrons flow from Ni to Fe, causing the increase of d-vacancy of Ni, resulting in a catalyst matching better to the reaction electron transfer coordination of OER (2 electrons) without affect the Fermi level of Ni. In addition, the alloying process could promote the formation of ultra-small secondary phase grains to effectively increase the ratio of active sites and alter the average lattice spacing. Therefore, a NiFe alloy possesses a great potential as low-cost, high-performance OER electrocatalyst.

Besides an ideal composition, further improving OER catalysis performance requires a high active surface area, [22-23] which is significantly affected by the microstructure. [24-25] The most effective and straightforward strategy to increase the surface area of a catalyst is to develop nanostructures with decreased particle size and increased porosity. With particle size reducing, more kink and step structure starts exposing to the surface as catalytic active centers. The nanostructure is usually seeded by the nucleation center from aggregation of atoms, which can give rise to different nanostructures. Dealloying is one of the most efficient strategies to develop monolithic metal or alloy nanostructures [26-28] The nanoscale pores derived from dealloying process can provide high surface areas and more active sites for catalytic reactions. At the same time the microscale pores can provide sufficient channels for the gas and ion diffusion. Compared to traditional powder-based electrode, a monolithic electrode/electrocatalyst can facilitate the electron conduction and eliminate the use of substrate binders.

As a rapid prototyping manufacturing method emerged in the late 1980s, laser-based manufacturing has lately become an established fabrication technique to 3D-print a variety of functional materials.[29-30] Lately, printing materials for energy applications, especially materials with specific energy storage or conversion activities have attracted a lot of attentions, such as phase change materials for thermal energy storage applications[31], lithium ion battery anode materials[32], photoanode material for dye sensitized solar cells[33], and catalyst platform for water splitting [34]. Compared to traditional electrocatalyst preparation methods, which not only require a tedious synthesis to receive desired catalyst composition and structure, but also need a careful control of supporting platform/electrode and binder properties, laser-based manufacturing is an excellent technique to prepare self-supported electrode or base/template for further process. Therefore, laser-based fabrication method can manufacture monolithic electrocatalyst easily with great advantages in simplifying the electrode assembling process and avoiding performance degradation.

In addition, laser processed alloys usually experience special thermal cycles that could produce anisotropic and heterogeneous microstructures significantly different from parts made by traditional casting method. Due to the rapid cooling rate and directional solidification, the laser-processed alloys may contain highly metastable microstructures, elongated crystalline, high porosity, gas trapping and balling, molten tracks, protruding particles and small concaves, which display advantages in preparing complex microstructures. The electrocatalytic performance of laser-processed alloys may differ significantly from traditionally processed alloys and provide interesting insights on novel electrocatalyst. Firstly, the surface imperfectness, such as corners, edges and kinks effectively increase the number of active sites on the catalyst surface. Secondly, laser-processed alloys usually have an exposed surface with molten tracks, protruding particles and small concaves that contribute to higher specific surface area. Thirdly, during the rapid solidification process, metastable crystal phases that are more favorable for certain electrochemical reactions may precipitate. Therefore, the laser processed Ni-Fe alloys prepared by varied laser scanning speeds could display apparent difference in the electrocatalytic activity.

Moreover, high-entropy alloys (HEAs), a new type of alloy, constructed of five or more metallic elements at equal or near-equal molecular ratios, are emerging into an attractive category of functional metallic materials.[35-36] Due to the varied atomic radius and structural configurations of the elements in an HEA, the lattice in the crystalline are usually seriously distorted, which leads to the special mechanical properties of HEA materials. Due to the severe defects existing in the lattice and combination of hypo-d and hyper-d in earth abundant transition metals, the valence electron concentration are possibly significantly changed.[37-39]Compared to traditional metals, HEAs are metastable with metal atoms staying in a high energy state with serious lattice distortions, which is one advantageous property for catalyst performance. Unfortunately, in the state of art, little results have been reported on the catalytic performance of HEAs.

1.2 Objective and Research Outline

The objective of this research is to develop Ni-Fe based electrocatalyst through laser-based manufacturing with focus on studying their chemical/electrochemical characteristics toward OER in the water electrocatalysis process.

In chapter 2, hydrogen energy and water splitting process are discussed on the aspects of electrochemistry thermodynamics and kinetics with catalysis fundamentals on absorption energy, electronic effect and geometry effect introduced. In addition, laser-based manufacturing is briefly introduced.

In chapter 3, a one-step laser-based manufacturing method is applied to prepare thin layers of NiFe alloys with varied Ni and Fe ratios as the electrocatalyst toward OER. Their crystal structures, morphologies and compositions are examined by XRD, XPS and SEM prior and after electrochemical testing. This chapter focuses on the study of the electron effect and crystal structure effect on electrochemical performance of NiFe alloy

In chapter 4, the laser processed Ni-Fe alloys are prepared by varied laser scanning speeds. Their microstructures and morphologies are examined by XRD and SEM. Their electrocatalytic performance toward OER electrocatalyst is studied. In addition Ni-Fe alloys prepared by arc melting and spark plasma sintering are also prepared for comparison.

In chapter 5, nanoporous NiFe electrocatalyst is developed by dealloying laser-based manufactured Ni-Fe-Al in a concentrated alkaline solution. This chapter focuses on the study of the nanostructure effect on the active surface area, electron transfer process, mass diffusion rate of NiFe alloy electrocatalyst and focuses on the development strategies to fabricate monolithic nanoporous electrode for energy conversion reactions.

In chapter 6, Ni, Fe and other earth-abundant metal based HEAs are synthesized via arc melting. The effect of lattice distortion, surface defect and individual element performance are studied and correlated to their electrochemical characteristics.

In chapter 7, the achievements and potential of this dissertation are concluded and potential topics for future work related to this dissertation are provided.

1.3 References

1. Cui, X.; Xu, W.; Xie, Z.; Wang, Y., Hierarchical SnO2@SnS2 Counter Electrodes for Remarkable High-efficiency Dye-sensitized Solar Cells. *Electrochimica Acta* **2015,** *186*, 125-132.

2. Wang, Z.; Mai, K.; Kumar, N.; Elder, T.; Groom, L. H.; Spivey, J. J., Effect of Steam During Fischer–Tropsch Synthesis Using Biomass-Derived Syngas. *Catalysis Letters* **2016**, 1-9.

3. Cui, X.; Xu, W.; Xie, Z.; Wang, Y., High-performance dye-sensitized solar cells based on Ag-doped SnS2 counter electrodes. *Journal of Materials Chemistry A* **2016,** *4* (5), 1908-1914.

4. Xu, W.; Xie, Z.; Cui, X.; Zhao, K.; Zhang, L.; Dietrich, G.; Dooley, K. M.; Wang, Y., Hierarchical Graphene-Encapsulated Hollow SnO2@SnS2 Nanostructures with Enhanced Lithium Storage Capability. *ACS Applied Materials & Interfaces* **2015,** *7* (40), 22533-22541.

5. Wang, Z.; Mai, K.; Kumar, N.; Elder, T.; Groom, L. H.; Spivey, J. J., Effect of Steam During Fischer–Tropsch Synthesis Using Biomass-Derived Syngas. *Catalysis Letters* **2017,** *147* (1), 62-70.

6. Greeley, J.; Jaramillo, T. F.; Bonde, J.; Chorkendorff, I.; Norskov, J. K., Computational high-throughput screening of electrocatalytic materials for hydrogen evolution. *Nat. Mater.* **2006,** *5* (11), 909-913.

7. Jaramillo, T. F.; Jorgensen, K. P.; Bonde, J.; Nielsen, J. H.; Horch, S.; Chorkendorff, I., Identification of Active Edge Sites for Electrochemical H2 Evolution from MoS2 Nanocatalysts. *Science (Washington, DC, U. S.)* **2007,** *317* (5834), 100-102.

8. Li, Y.; Wang, H.; Xie, L.; Liang, Y.; Hong, G.; Dai, H., MoS2 Nanoparticles Grown on Graphene: An Advanced Catalyst for the Hydrogen Evolution Reaction. *J. Am. Chem. Soc.* **2011,** *133* (19), 7296-7299.

9. Tisone, T. C.; Sundahl, R. C.; Chin, G. Y., Stacking fault energy in noble metal alloys. *Met. Trans.* **1970,** *1*, 1561-7.

10. Zhang, J.; Zhao, Z.; Xia, Z.; Dai, L., A metal-free bifunctional electrocatalyst for oxygen reduction and oxygen evolution reactions. *Nat. Nanotechnol.* **2015,** *10* (5), 444-452.

11. Trotochaud, L.; Young, S. L.; Ranney, J. K.; Boettcher, S. W., Nickel-Iron Oxyhydroxide Oxygen-Evolution Electrocatalysts: The Role of Intentional and Incidental Iron Incorporation. *J. Am. Chem. Soc.* **2014,** *136* (18), 6744-6753.

12. Trotochaud, L.; Ranney, J. K.; Williams, K. N.; Boettcher, S. W., Solution-Cast Metal Oxide Thin Film Electrocatalysts for Oxygen Evolution. *J. Am. Chem. Soc.* **2012,** *134* (41), 17253-17261.

13. Reier, T.; Oezaslan, M.; Strasser, P., Electrocatalytic Oxygen Evolution Reaction (OER) on Ru, Ir, and Pt Catalysts: A Comparative Study of Nanoparticles and Bulk Materials. *ACS Catal.* **2012,** *2* (8), 1765-1772.

14. Lee, Y.; Suntivich, J.; May, K. J.; Perry, E. E.; Shao-Horn, Y., Synthesis and Activities of Rutile IrO2 and RuO2 Nanoparticles for Oxygen Evolution in Acid and Alkaline Solutions. *J. Phys. Chem. Lett.* **2012,** *3* (3), 399-404.

15. Cui, X.; Zdunek, A. D.; Jursich, G.; Takoudis, C. G., Nanostructured Ni-YSZ by Atomic Layer Deposition. *ECS J. Solid State Sci. Technol.* **2015,** *4* (12), P429-P435.

16. Wang, Z.; Kumar, N.; Spivey, J. J., Preparation and characterization of lanthanum-promoted cobalt–copper catalysts for the conversion of syngas to higher oxygenates: Formation of cobalt carbide. *Journal of Catalysis* **2016,** *339* (Supplement C), 1-8.

17. Kumar, N.; Roy, A.; Wang, Z.; L'Abbate, E. M.; Haynes, D.; Shekhawat, D.; Spivey, J. J., Bi-reforming of methane on Ni-based pyrochlore catalyst. *Applied Catalysis A: General* **2016,** *517* (Supplement C), 211-216.

18. Yeo, B. S.; Bell, A. T., In Situ Raman Study of Nickel Oxide and Gold-Supported Nickel Oxide Catalysts for the Electrochemical Evolution of Oxygen. *J. Phys. Chem. C* **2012,** *116* (15), 8394-8400.

19. Wehrens-Dijksma, M.; Notten, P. H. L., Electrochemical Quartz Microbalance characterization of Ni(OH)2-based thin film electrodes. *Electrochim. Acta* **2006,** *51* (18), 3609-3621.

20. Chen, G.-F.; Ma, T. Y.; Liu, Z.-Q.; Li, N.; Su, Y.-Z.; Davey, K.; Qiao, S.-Z., Efficient and Stable Bifunctional Electrocatalysts Ni/NixMy (M = P, S) for Overall Water Splitting. *Adv. Funct. Mater.* **2016,** *26* (19), 3314-3323.

21. Zhao, J.; Zhang, W.; Huq, A.; Misture, S. T.; Zhang, B.; Guo, S.; Wu, L.; Zhu, Y.; Chen, Z.; Amine, K.; Pan, F.; Bai, J.; Wang, F., In Situ Probing and Synthetic Control of Cationic Ordering in Ni-Rich Layered Oxide Cathodes. *Adv. Energy Mater.* **2017,** *7* (3), n/a.

22. Esswein, A. J.; McMurdo, M. J.; Ross, P. N.; Bell, A. T.; Tilley, T. D., Size-Dependent Activity of Co3O4 Nanoparticle Anodes for Alkaline Water Electrolysis. *J. Phys. Chem. C* **2009,** *113* (33), 15068-15072.

23. Zhuang, Z.; Sheng, W.; Yan, Y., Synthesis of Monodisperse Au@Co3O4 Core-Shell Nanocrystals and Their Enhanced Catalytic Activity for Oxygen Evolution Reaction. *Adv. Mater. (Weinheim, Ger.)* **2014,** *26* (23), 3950-3955.

24. Masa, J.; Xia, W.; Sinev, I.; Zhao, A.; Sun, Z.; Gruetzke, S.; Weide, P.; Muhler, M.; Schuhmann, W., MnxOy/NC and CoxOy/NC Nanoparticles Embedded in a Nitrogen-Doped Carbon Matrix for High-Performance Bifunctional Oxygen Electrodes. *Angew. Chem., Int. Ed.* **2014,** *53* (32), 8508-8512.

25. Deng, X.; Tueysuez, H., Cobalt-Oxide-Based Materials as Water Oxidation Catalyst: Recent Progress and Challenges. *ACS Catal.* **2014,** *4* (10), 3701-3714.

26. Rosen, J.; Hutchings, G. S.; Jiao, F., Ordered Mesoporous Cobalt Oxide as Highly Efficient Oxygen Evolution Catalyst. *J. Am. Chem. Soc.* **2013,** *135* (11), 4516-4521.

27. Tueysuez, H.; Hwang, Y. J.; Khan, S. B.; Asiri, A. M.; Yang, P., Mesoporous Co3O4 as an electrocatalyst for water oxidation. *Nano Res.* **2013,** *6* (1), 47-54.

28. Zhao, Y.; Xu, L.; Mai, L.; Han, C.; An, Q.; Xu, X.; Liu, X.; Zhang, Q., Hierarchical mesoporous perovskite La0.5Sr0.5CoO2.91 nanowires with ultrahigh capacity for Li-air batteries. *Proc. Natl. Acad. Sci. U. S. A.* **2012,** *109* (48), 19569-19574, S19569/1-S19569/6.

29. Tancogne-Dejean, T.; Spierings, A. B.; Mohr, D., Additively-manufactured metallic micro-lattice materials for high specific energy absorption under static and dynamic loading. *Acta Mater.* **2016,** *116*, 14-28.

30. Ambrosi, A.; Pumera, M., Self-Contained Polymer/Metal 3D Printed Electrochemical Platform for Tailored Water Splitting. *Adv. Funct. Mater.* **2017**, Ahead of Print.

31. Nofal, M.; Pan, Y.; Al-Hallaj, S., Selective Laser Sintering of Phase Change Materials for Thermal Energy Storage Applications. *Procedia Manufacturing* **2017,** *10* (Supplement C), 851-865.

32. Chen, Y.-T.; Hung, F.-Y.; Lui, T.-S.; Hong, J.-Z., Microstructures and Charge-Discharging Properties of Selective Laser Sintering Applied to the Anode of Magnesium Matrix. *MATERIALS TRANSACTIONS* **2017,** *58* (4), 525-529.

33. Ming, L.; Yang, H.; Zhang, W.; Zeng, X.; Xiong, D.; Xu, Z.; Wang, H.; Chen, W.; Xu, X.; Wang, M.; Duan, J.; Cheng, Y.-B.; Zhang, J.; Bao, Q.; Wei, Z.; Yang, S., Selective laser sintering of TiO2 nanoparticle film on plastic conductive substrate for highly efficient flexible dye-sensitized solar cell application. *Journal of Materials Chemistry A* **2014,** *2* (13), 4566-4573.

34. Ambrosi, A.; Pumera, M., Self-Contained Polymer/Metal 3D Printed Electrochemical Platform for Tailored Water Splitting. *Advanced Functional Materials*,

1700655-n/a.

35. Miracle, D. B.; Senkov, O. N., A critical review of high entropy alloys and related concepts. *Acta Materialia* **2017,** *122*, 448-511.

36. Ye, Y. F.; Wang, Q.; Lu, J.; Liu, C. T.; Yang, Y., High-entropy alloy: challenges and prospects. *Materials Today* **2016,** *19* (6), 349-362.

37. Lv, Z. Y.; Liu, X. J.; Jia, B.; Wang, H.; Wu, Y.; Lu, Z. P., Development of a novel high-entropy alloy with eminent efficiency of degrading azo dye solutions. *Scientific Reports* **2016,** *6*, 34213.

38. Jakšić, J. M.; Krstajić, N. V.; Grgur, B. N.; Jakšić, M. M., Hydridic and electrocatalytic properties of hypo-hyper-d-electronic combinations of transition metal intermetallic phases. *International Journal of Hydrogen Energy* **1998,** *23* (8), 667-681.

39. Jaksic, M., *Hypo-hyper-d-electronic interactive nature of synergism in catalysis and electrocatalysis for hydrogen reactions*. 2001; Vol. 26, p 559-578.

2 INTRODUCTION

2.1 Hydrogen Energy and Water Electrolysis

2.1.1 Energy Crisis and Hydrogen Energy

Due to the fast developing modern technology since the industrial revolution, the demand for energy is rapidly growing, which is mainly supplied by fossil energies, such as petroleum, coal and natural gas. As it is known, fossil fuels are organic compounds formed by natural process of anaerobic decomposition that may take hundreds of millions of years.[1-2] The properties of a fossil fuel, such as the boiling point, viscosity and energy density mainly depend on the fuel mixture composition. The start of exploitation of petroleum in commercial scale was in the 19th century, since when petroleum oil and gas has taken the stage of history from animal oil. [3] Fossil fuels have played a crucial role in the past several decades. Fossil fuels produce a considerable amount of energy, which accounts for the vast majority of human activity energy requirement.

Nowadays, due to the rapid consumption of fossil fuels and the severe environmental and economic concerns, the exploration of renewable and clean energy sources becomes more urgent.[4-7] The product of combusting fossil fuels consists of a series of hazardous substances, which seriously impact the environment. Greenhouse gas (GHG) emission is the most direct impact caused by fossil fuel combustion for generating electricity, heat and transportation. GHG is gas phase materials in the environment that absorbs solar energy and emits radiations in the infrared wavelength, which causes the so-called greenhouse effect.[8] Greenhouse gases on earth are in the abundance order of water vapor (H_2O), carbon dioxide (CO_2), methane (CH_4), nitrous oxide (N_2O), ozone (O_3), chlorofluorocarbons (CFCs) and hydrofluorocarbons (incl. HCFCs and HFCs). World widely, greenhouse gas emissions are primarily from combustion of fossil fuels. Greenhouse emission keeps increasing since the industrial revolution. The GHG emissions in the U.S. have increased by ~ 4% since 1990, which fluctuate with the changes in the nature, economy, and political environments. And it is estimated that if the greenhouse gas emissions continue increasing at its current rate, the earth surface temperature might reach it historical highest value by 2047[9] and 2 °C global warming climate danger threshold by 2036[10], that may cause a major harm to human life, even the whole ecosystem. In addition, the combustion of fossil fuels generates a lot of acids, including carbonic acids, nitric acids and sulfuric acids, which could corrode the nature and cultural environment and harm human health in the form of acid rain. Especially for buildings contain marble and limestone, the calcium carbonate dissolved by acid rains. Moreover, many fossil fuels contain radioactive elements, such as thorium and uranium. In the most recent decade, thousands of tons of radioactive materials are released to the environment worldwide each year from fossil fuel combustion, especially from coal. Bottom ash and fly ash can also be resulted by burning solid state fossil fuels. 140 million tons of ashes are produced in the U.S. each year by fossil fuel combustion, which has become the second-largest waste stream after trash in the country. At last, extracting, processing and

transporting fossil fuels also generate severe economic and environmental burden. Fossil fuel sources are reserved in the ground. The world energy demand is expected to be doubled every fourteen years[11]. In the past two centuries, a great portion of fossil fuels have been consumed, which took millions of years to form. At current computation rate, the known oil will run out at 2052, known gas will run out at 2060 and known coal will run out at 2088. [12]

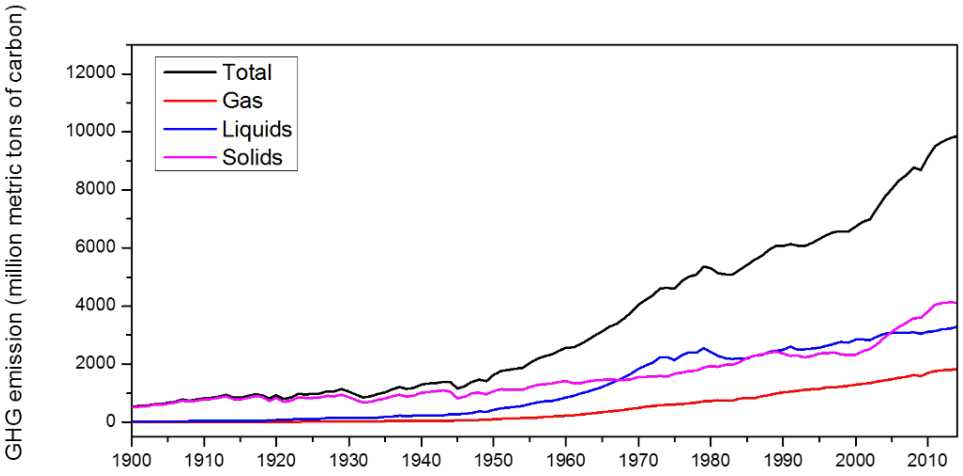

Figure 2.1 Greenhouse gas emissions from fossil fuels 1900 to 2014, data source is global, regional, and national fossil-fuel CO_2 emissions 2017. [13]

Due to the fast diminishing supply and increasing side effect of fossil fuel energy sources, renewable energies have become an economical alternative to exploit. To 2013, renewable energy consumption has reached 19% worldwide, with 78.4% fossil fuel and 2.6% nuclear energy.[14] Renewable energy distributes widely regardless of the geographical properties that both satisfies the energy demand and relieves the environmental burden. Hydrogen, as a highly sustainable, energy-dense and non-polluting energy carrier has long been considered as a promising fuel. As one of the most abundant element on earth, hydrogen is plentiful reserved in solid, liquid and gas phases. When burning hydrogen in air, almost no other byproducts besides water are produced, causing little side effects to environment and no harm to human health.

$$2H_2\,(g) + O_2\,(g) \rightarrow 2H_2O\,(l) + 572kJ \quad \text{(eq. 1)}$$

Under combustion conditions, hydrogen reacts with oxygen and forms water. Energy is released as a form of thermal radiation emission with water molecule transiting to its ground state. The equation indicates the combustion of 2 mol H_2 with 1 mol O_2 can release 572 kJ energy, with a hydrogen energy density of 143kJ/g. Due to its light weight and clean nature, hydrogen has started to become an important energy source for fuel cells engines to supply power to electrical vehicles and even aircrafts. For example, hydrogen is a main fuel for NASA space shuttle's onboard electric power generation units, with hydrogen combustion product a drinking water source for spacemen. In addition, many vehicle companies have started to explore hydrogen as the

onboard fuel, either through fuel cells reactions or directly convert chemical energy of hydrogen into mechanical energy through an automobile engine. There are already hydrogen cars in the markets, such as the Honda Clarity, the Toyota Mirani and the Hyundai ix35 FCEV.

Hydrogen is the first element in the parodic table. Due to the high chemical activity, hydrogen mostly exists in compound substances, including water and various hydrocarbons. Currently, the cost of hydrogen energy is challenged by the difficulty of extracting hydrogen from its compounds. To date, the majority of hydrogen gas is produced by steam-reforming of fossil fuels, including biomass, natural gas and coal. However, severe environmental side effects is observed and using fossil fuel raw material further aggravates the energy crisis.[15] Comparably, electrochemical water splitting is extensively promising for hydrogen generation from renewable energy sources, since it can be achieved at a large scale with water as a convenient raw material and cause almost zero-pollution[16-18]. When renewable energy, such as solar energy and wind energy is abundant, excessive electrical energy can be converted to hydrogen energy through water electrolysis process. Then hydrogen can be used to generate electricity in special forms or used directly.

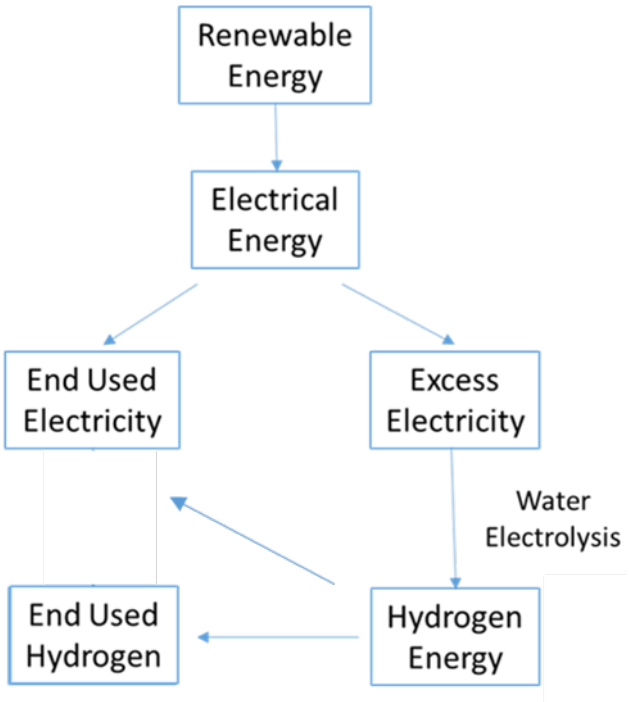

Figure 2.2 Energy system for water electrolysis

2.1.2 Water Electrolysis

Water electrolysis is to produce oxygen gas and hydrogen gas through splitting water molecule by applying a potential higher than standard potential for water decomposition. It has been used to both produce hydrogen fuels for energy supply and

high-purity oxygen for breath supply. It was firstly invented by William Nicholson and Anthony Carlisle in 1800. In 1869 Zenobe Gramme made generating hydrogen by water electrolysis an affordable method through inventing Gramme machine. In 1888, Dmity Lachinov industrialized water electrolysis.[19] The simplified setup of water electrolysis includes a container filled with pure water as the raw material with electrolyte to assist electron transfer, a cathode coated with hydrogen evolution reaction catalytic active materials, an anode coated with oxygen evolution reaction catalytic active materials, and a direct-current power applied at a certain overpotential.

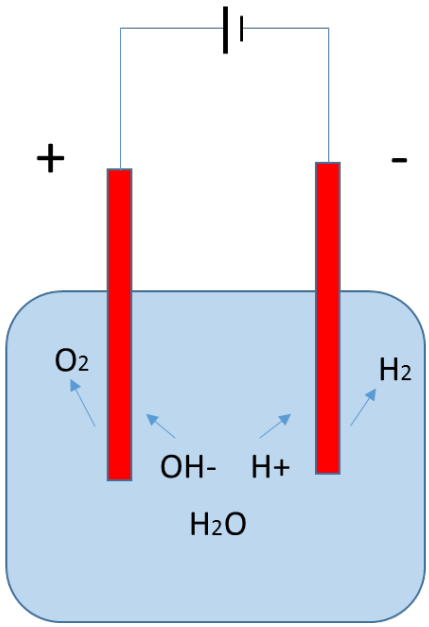

Figure 2.3 Demonstration of water electrolysis

During the water electrolysis process, if the electrolyte is balanced with acid, H^+ receives electrons (e^-) from cathode and forms hydrogen. The half reaction at cathode is:

$$H^+ + e^- \rightarrow \frac{1}{2}H_2 \quad \text{(eq. 2)}$$

At anode, H_2O is oxidized to generate oxygen gas and give out electrons to the outside circuit. The half reaction at anode is:

$$H_2O \rightarrow \frac{1}{2}\, O_2 + 2\, H^+ + 2e^- \quad \text{(eq. 3)}$$

If the electrolyte is balanced with base, at cathode, H_2O receives electrons to form H_2 and OH^-. The half reaction at cathode is

$$H_2O + 2e^- \rightarrow \frac{1}{2}H_2 + OH^- \quad \text{(eq. 4)}$$

At anode, OH^- is oxidized into O_2, H_2O and release electrons

$$2OH^- \rightarrow \frac{1}{2}O_2 + H_2O + 2\, e^- \quad \text{(eq. 5)}$$

In both case, the overall reaction is:

$$H_2O \rightarrow H_2 + ½O_2 \quad \text{(eq. 6)}$$

Ideally, the amount of H_2 generated is twice the amount of O_2. And the amount of molecules produced is proportional to electrons transferred in the circuit at ideal Faradic efficiency. [20] However, due to the non-ideal conditions of electrochemical cell operation and the existence of side reactions, lower faradaic efficiency is resulted. In pure water electrolysis process, hydrogen cations and hydroxide anions concentrate at the cathode and anode, respectively, resulting in a decreased PH close to cathode and an increased PH close to anode. However, most H^+ and OH^- ions meet each other before receiving electrons from or giving out electrons to the outside circuits and form H_2O molecules instead, which results in overpotentials at both cathode and anode. At standard conditions, water splitting is thermodynamically non-favored. Under ideal condition, water electrolysis requires a potential of 1.23 V to overcome the thermodynamic barrier. However, under real conditions, the water splitting potential is increased by kinetic factors. The series resistance, mass diffusion, surface active sites all affect the potential to overcome kinetic barriers, which results in an overpotential (the difference between the experimental potential and thermodynamic potential required for a half reaction to happen, which largely determines the electrochemistry cell efficiency).[21] At standard conditions, the electrical conductivity of deionized water is very low, causing a slow kinetic of electrolysis of pure water. Therefore an electrolyte can be disassociated into ions when dissolved in water is necessary to improve the electrical conductivity. Also, to avoid competitive reactions to H_2 or O_2 formation, the anion of the added electrolyte need to have a higher standard electrode potential than OH^- and the cation need to have a lower standard electrode potential than H^+. Therefore, in basic electrolyte, the selection of cations is mostly among active metals of higher activity than H^+, with Na^+, K^+ and Li^+ as commonly used ions. In acidic solutions, the acid radical most used is $(SO_4)^{2-}$, whose standard electrode potential is -2.05 V vs RHE, much more negative than -1.23 V. Overall, the most frequently used electrolyte includes sulfuric acid, potassium hydroxide and sodium hydroxide. Though water electrolysis is a good technique that can provide hydrogen fuel cleanly, its wide commercialization is still hindered by its high expense. In the history of water electrolysis, tremendous effort has been devoted in increasing the water electrolysis efficiency and lower the material cost, especially the cost on electrode materials. Traditionally, noble metal-based materials are most used for both hydrogen evolution reaction and oxygen evolution reaction, which significantly increases the material cost. Therefore the development of efficient electrocatalyst based on earth-abundant materials becomes very attractive.

Under standard condition (T = 298 K, P =1 atm), the water electrolysis is following the equation:

$$H_2O\,(l) \rightarrow H_2\,(g) + ½\,O_2\,(g) \quad \text{(eq. 7)}$$

The standard Gibbs free energy changes for liquid H_2O formation from vapor phase H_2 and O_2 is

$$\Delta H^{\circ}(H_2O(l)) = 285.8 \text{ kJ/mol} \quad \text{(eq. 8)}$$

$$\Delta S^{\circ}(H_2O(l)) = 163.1 \text{ J/mol}\cdot\text{K} \quad \text{(eq.9)}$$

$$\Delta G^{\circ}(H_2O(l)) = \Delta H^{\circ}(H_2O(l)) - T \cdot \Delta S^{\circ}(H_2O(l)) = 237.2 \text{ kJ/ mol} \quad \text{(eq.10)}$$

Where ΔH° ΔS° and ΔG° are enthalpy, entropy and Gibbs free energy standard changes for reaction

According to the law of conservation of energy, the standard electricity required to split one mole of water is

$$\Delta G^{\circ} - nFE^{\circ} = 0 \quad \text{(eq. 11)}$$

Where: n is the number of transferred electrons for one H_2O molecule splitting, n=2;

F is the Faraday constant, F=96485 C/mol;

E is the standard potential required for water splitting.

$$E^{\circ} = \frac{\Delta G^{\circ}}{nF} = \frac{237.2*1000}{2*96485} = 1.23 \text{ V} \quad \text{(eq. 12)}$$

The water splitting potential is independent of PH

To calculate the equilibrium cell potential of an electrochemical reaction, Nernst equation is used[22]

$$E_{eq} = E^{o} + \frac{RT}{nF} \ln \frac{Co}{CR} \text{ (eq. 13)}$$

Where: E_{eq} is the equilibrium cell potential;

E^{o} is the standard cell potential;

R is the universal gas constant;

T is the temperature;

F is Faraday constant; n is the number of transferred electrons;

C_O is the concentration of oxidizer;

C_R is the concentrations of reductant.

Under acidic conditions, according to Nernst equations,

The half reaction at cathode is: $H^{+} + e^{-} \rightarrow \frac{1}{2}H_2$ (eq. 14)

$$E^{-} = E^{\circ}_{H2/H+} + \frac{RT}{nF} \ln \frac{a^2_{H+}}{f_{H2}} = -0.06 \text{ pH (eq. 15)}$$

The half reaction at anode is: $H_2O \rightarrow \frac{1}{2} O_2 + 2 H^+ + 2e^-$ (eq. 16)

$$E^+ = E^\circ_{H2O/O2} + \frac{RT}{nF} \ln \frac{a_{H+}^2 f_{O2}^{1/2}}{a_{H2O}} = 1.23 \text{ V} - 0.06 \text{ pH} \quad \text{(eq. 17)}$$

$$E = E^+ - E^- = 1.23 \text{ V} \quad \text{(eq. 18)}$$

Where: a is the activity of protons, ions and molecules;

f is the fugacity of gas phase molecules.

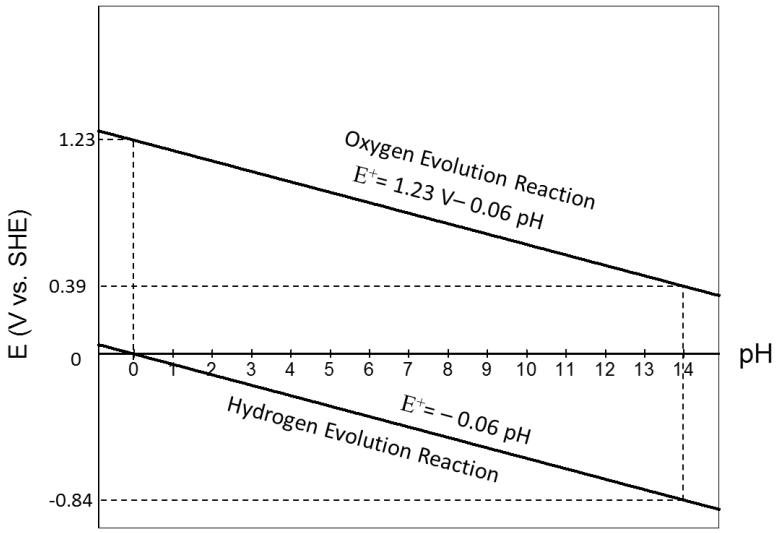

Figure 2.4 Equivalent water splitting potential vs. pH

At standard condition (T = 25 °C and P = 1 atm), water splitting requires an equilibrium cell potential of 1.23 V to overcome the thermodynamic barrier.

In acidic environment (PH = 0):

Cathode: $H^+ + e^- \rightarrow \frac{1}{2} H_2$ $E^o = 0.00$ V (eq. 19)

Anode: $H_2O \rightarrow \frac{1}{2} O_2 + 2 H^+ + 2e^-$ $E^o = 1.23$ V (eq. 20)

In basic environment (PH = 14):

Cathode: $H_2O + 2e^- \rightarrow \frac{1}{2} H_2 + OH^-$ $E^o = 0.39$ V (eq. 21)

Anode: $2OH^- \rightarrow \frac{1}{2} O_2 + H_2O + 2 e^-$ $E^o = -0.84$ V (eq. 22)

The water splitting potential is significantly affected by the temperature. Under atmosphere pressure:

$$H_i(T) = H_i^{\circ} + a(T - T_0) + \frac{b}{2} * 10^{-3} (T^2 - T_0^2) - c * 10^5 \left(\frac{1}{T} - \frac{1}{T0}\right) \quad (\text{eq. } 23)$$

$$S_i(T) = S_i^{\circ} + a(\ln T - \ln T_0) + b * 10^{-3} (T - T_0) - c * 10^5 \left(\frac{1}{T} - \frac{1}{T_0^2}\right) \quad (\text{eq. } 24)$$

$$\Delta H(T) = H_{H2}(T) + \tfrac{1}{2} H_{O2}(T) - H_{H2O}(T) \quad (\text{eq. } 25)$$

$$\Delta S(T) = S_{H2}(T) + \tfrac{1}{2} S_{O2}(T) - S_{H2O}(T) \quad (\text{eq. } 26)$$

$$\Delta G(T) = \Delta H(T) - T\Delta S(T) \quad (\text{eq. } 27)$$

$$E(T) = \frac{\Delta G(T)}{2F} = 1.518 - 1.542 * 10^{-3} * T + 9.523 * 10^{-5} * T * \ln(T) + 9.84 * 10^{-8} * T^2 \quad (\text{eq. } 28)$$

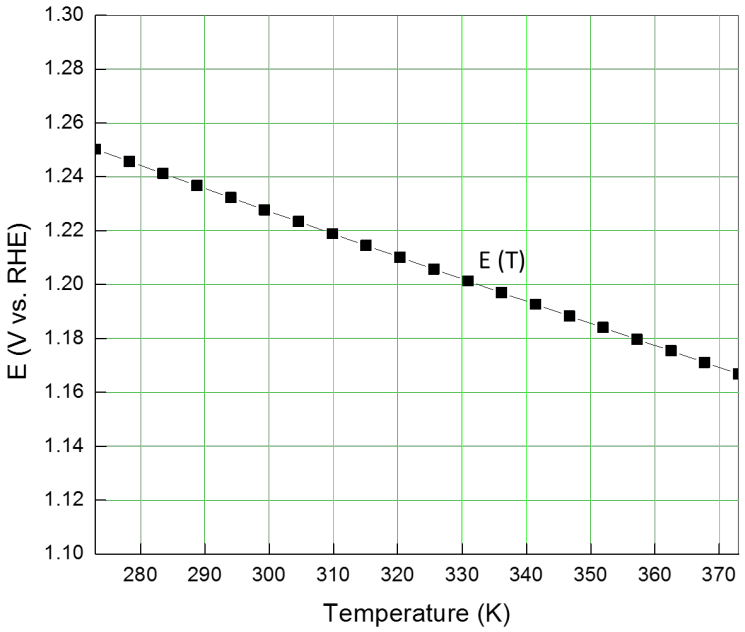

Figure 2.5 Thermodynamic water electrolysis voltage vs. temperature from 273K to 373K

Table 2.1 Gas temperature coefficients [23] for equation 28

	a	**b**	**c**
H_2 (g)	26.57	3.77	1.17
O_2 (g)	34.35	1.92	-18.45

It is observed, the voltage decreases from 1.23 V at 25 °C to 1.18 V at 100 °C, the water splitting potential decreases with increased temperature.

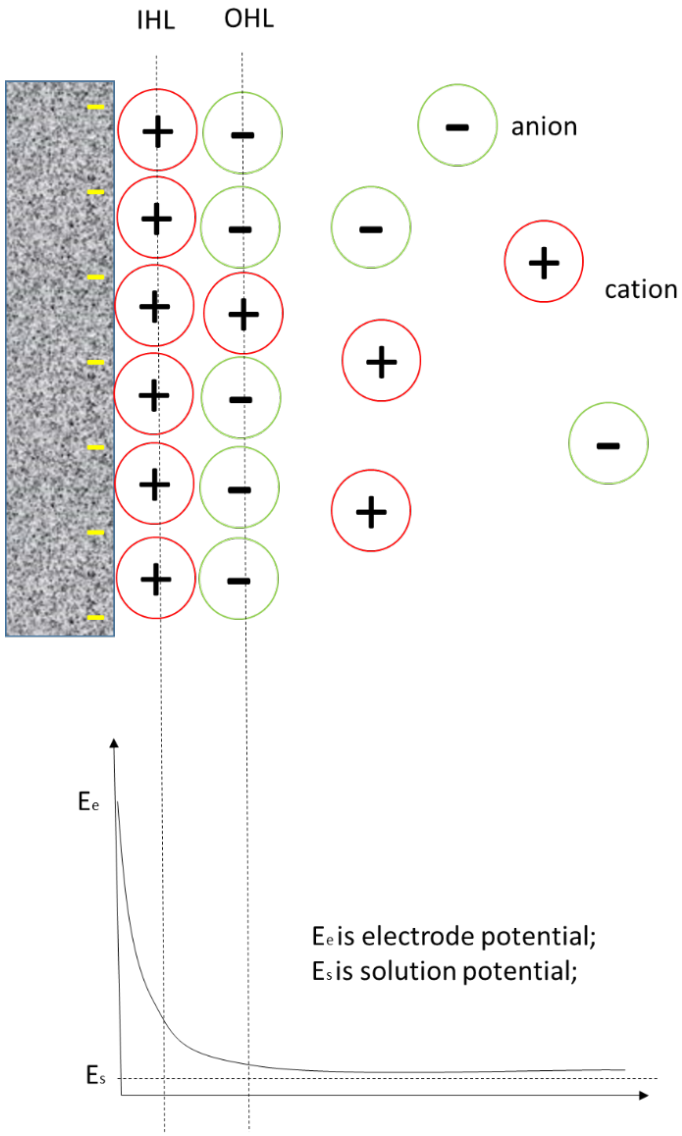

Figure 2.6 Illustration of double layer and potential distribution close to the electrode

Water electrolysis reactions are heterogeneous reaction happening on the interface between electrode and electrolyte. In the region close to the electrode region, a double-layer electrochemical boundary is formed in this region, which experiencing the discontinuous electrolyte velocity, chemical species concentration and potential gradient. As illustrated in Fig.2-6, the cations and anions form two mobile layers near the electrode surface, which are called inner Helmholtz layer (IHL) and outer Helmholtz layer (OHL), balanced by ions with counter charges in the area around the electrodes. It is also observed, the interfacial potential decays along the double layers. The existence of double layer causes the potential gradient between the electrode surface and electrolyte (ΔE), $\Delta E = Ee - Es$ serving as driving force for electron transfers, which is significantly affected by species adsorbed on the electrode surface. In addition, ΔE causes the localized driving force of the electrode/electrolyte interface reactions, which affects the reaction rate, electrode efficiency and product selectivity.

Due to the existence of kinetic barriers, the reactions need higher potentials than the equilibrium potential, which is the so-called overpotential (η). The overpotential is composed of anode overpotential (η_a), cathode overpotential (η_c) and other overpotential (η_o), such as the overpotential caused by series resistances.[24]

$$\eta = E - E^o \quad \text{(eq. 29)}$$

$$\eta = \eta_c + \eta_a + \eta_o \quad \text{(eq. 30)}$$

In alkaline environment, three elemental steps are involved for hydrogen evolution reaction on the cathode. The first step is the formation of adsorbed hydrogen on the electrode surface. The second step is the formation and chemical desorption of H_2 from the electrode surface. The last step is the formation and chemical desorption of H_2 from the electrode surface and electrochemical desorption of OH^-.

$$H_2O + e^- \rightarrow H_{ads} + OH^- \quad \text{(eq. 31)}$$

$$2\ H_{ads} \rightarrow H_2 \quad \text{(eq. 32)}$$

$$H_{ads} + H_2O + e^- \rightarrow H_2 + OH^- \quad \text{(eq. 33)}$$

The overpotential on the cathode side is decided by the hydrogen formation process close to the electrode surface, which is essentially affected by the binding strength between adsorbed hydrogen intermediate and the cathode surface. If the hydrogen atoms bind to the electrode surface too strongly, desorption of H_2 molecule is inhibited. On the contrary, if hydrogen atoms bind too weakly, it is becoming difficult to stabilize the hydrogen intermediate and inhibit the reaction too. Therefore a modest binding energy is favorable for an active electrode. The hydrogen evolution reaction mechanism is decided by the applied overpotential. At low potentials, the electron transfer is the slowest step. The hydrogen adsorption is the rate determining step. Under this condition, electrode with a high surface area allows more hydrogen adsorption. At high potential, with the hydrogen adsorption step is greatly facilitated, the hydrogen desorption is the rate determining step. Under this condition, electrode with rougher surface can effectively enhance hydrogen molecule repelling.

The most generally accepted oxygen evolution reaction mechanism in alkaline environment happening on the anode has three steps. The first step is the formation of adsorbed hydroxide on the anode surface. The second step is the formation of adsorbed oxide the anode surface. The last step is the formation and chemical desorption of O_2 from the anode surface.

$$OH^- \rightarrow OH_{ads} + e^- \quad \text{(eq. 34)}$$

$$OH^- + OH_{ads} \rightarrow O_{ads} + H_2O + e^- \quad \text{(eq. 35)}$$

$$O_{ads} + O_{ads} \rightarrow O_2 \quad \text{(eq. 36)}$$

Similar to the hydrogen evolution process, the overpotential on the anode side is determined by the oxygen formation process that is essentially affected by the binding strength between adsorbed oxygen intermediate atom and the cathode surface. If the oxygen atoms bind to the electrode surface too strongly, desorption of O_2 is inhibited. On the contrary, if oxygen atoms bind too weakly, it is becoming difficult to stabilize the oxygen intermediate and inhibit the reaction too. Therefore a modest binding energy is favorable for an active electrode. At low potentials, the electron transfer is the slowest step. The first step is the rate determining step. At high potential is, the chemical and electrochemical desorption is the rate determining step.

The overpotential at each electrode is directly determined by the formation of hydrogen and oxygen in the vicinity of the electrodes. The energy efficiency of water electrolysis is defined by the percentage of the energy output over the energy input. The Faradic efficiency is calculated by the ratio of effective voltage for water splitting over the total applied voltage:

$$\text{Faradic efficiency} = \frac{E^o}{E_{cell}} * 100\% \quad \text{(eq. 37)}$$

$$\text{Faradic efficiency} = \frac{E^o}{E^o + \eta} * 100\% \quad \text{(eq. 38)}$$

Therefore, lowering down overpotentials can effectively increase the water electrolysis efficiency. By accelerating the kinetics at anode / electrolyte and cathode / electrolyte interfaces, the η_a and η_c can be minimized to facilitate the oxygen evolution reaction and hydrogen evolution reaction, respectively. Herein, a development of advanced electrocatalyst materials is highly promising for improve the performance of overall water splitting. Electrocatalyst is a type of catalyst that can facilitate electron transfer at electrode and electrolyte interface in electrochemical processes. For hydrogen evolution reactions and oxygen evolution reactions, the most traditionally used electrocatalysts are noble metal catalysts, such as Pt, Ru and Ir.[25-26] The performance of the electrocatalyst is significantly affected by the morphology of the materials. Nevertheless, the commercialization of water splitting is severely hindered by the scarcity and high cost of these noble-metal materials. Therefore, developing affordable and efficient electrocatalyst to replace traditional noble metal catalysts for both hydrogen evolution reaction and oxygen evolution reactions is becoming more and more urgent. Sometimes, the electrode itself serves as the electrocatalyst to reduce the overpotentials for electrode/electrolyte interface reactions. In addition to material selection, electrode design is also crucial for electron and mass transportation, gas bubble removing.

Three-electrode system is most commonly used to characterize the electrochemical characteristics of the electrocatalyst. To setup an electrochemical circuit, at least two electrodes (working electrode and counter electrode) are needed. The working electrode is the electrode of interest, where the studied half-cell reaction occurs with the controlled potential applied on. The counter electrode is where the other half-cell reaction occurs with a known potential applied and the electron transfer balanced. However, it is not viable to maintain the electrode at a constant potential

when current passing the electrode due to redox half-cell reactions. Therefore, reference electrode is applied to providing a reference potential, who has a known reduction potential with no current passing through. Then the potential at the working electrode can be easily measured and controlled. The stable potential of the reference electrode is maintained by applying a system with constant potentials. There are several common used reference electrodes, including standard hydrogen electrode (SHE), normal hydrogen electrode (NHE), reversible hydrogen electrode (RHE), saturated calomel electrode (SCE), copper-copper (II) sulfate electrode(CSE), silver chloride electrode, PH-electrode, palladium-hydrogen electrode, dynamic hydrogen electrode (DHE) and mercury-mercurous sulfate electrode (MSE). In this dissertation, the saturated calomel electrode (SCE) is applied as the reference electrode. The SCE is based on the redox reaction between Hg and $HgCl_2$ in aqueous solution.

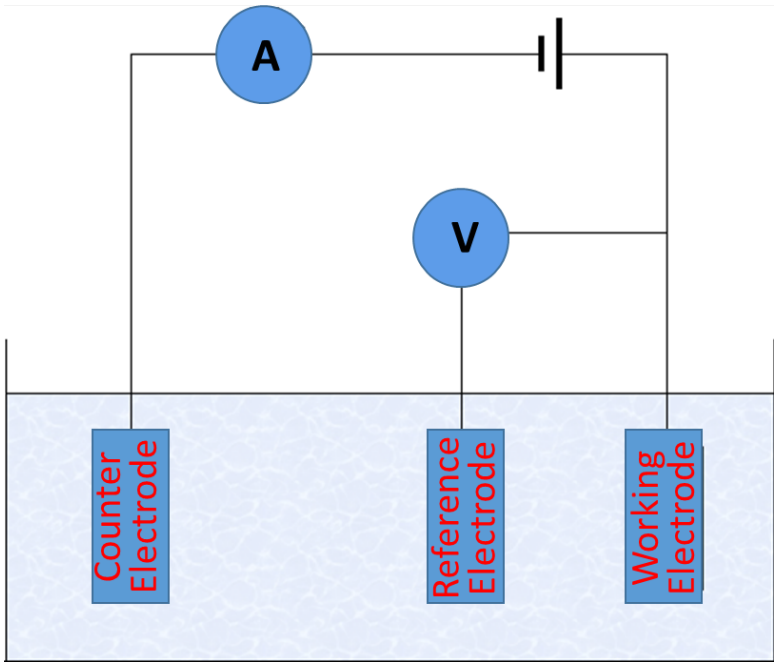

Figure 2.7 Illustration of three-electrode system

2.2 Electrocatalyst for Oxygen Evolution Reaction

2.2.1 Electrocatalysis Principles

Electrochemical reactions are redox reactions at electrode/electrolyte interfaces with only electrons transferred and the electrode surface unchanged. The reaction rates and adsorption/desorption equilibria strongly depend on the applied potential. So an electrochemical reaction is not only driven by chemical forces, such as temperature, pressure and reactant concentrations, but also significantly sensitive to electrical potentials. In addition, the adsorption and desorption of reactants and reaction intermediates are critical for the rate of electrochemical reactions. The slow kinetic of intermediate reactions is usually the control factor of an electrochemical reaction, but

can be effectively accelerated by applying suitable heterogeneous electrocatalysis. Electrocatalysis is the process during which reactants adsorb on the electrocatalyst surface followed by electrochemical interaction activations to more rapidly and selectively convert the adsorbed intermediates to product. After desorption of product, the electrocatalyst immediately recover to its original state. These electrocatalysis process allows an energy shortcut at much lower overpotentials than if no electrocatalyst is applied. For unspontaneous reactions, the minimum energy needed for an electrochemical reaction to happen is the activation energy. As illustrated in Fig. 2-8, all reactions need to go through a certain pathway, with a minimum energy required to break bonds in reactant molecules, which is called the activation energy ΔE. If the applied energy is larger than this minimum activation energy ΔE, the kinetic barrier is overcome. Through the formation of the product, the energy is released. The energy difference between the reactants and products is the thermodynamic energy ΔE°. In a catalyzed reaction, the activation energy is lowered, since the formation of intermediate state requires much lower energy, which reduces the kinetic energy barrier and accelerates the reaction rate.

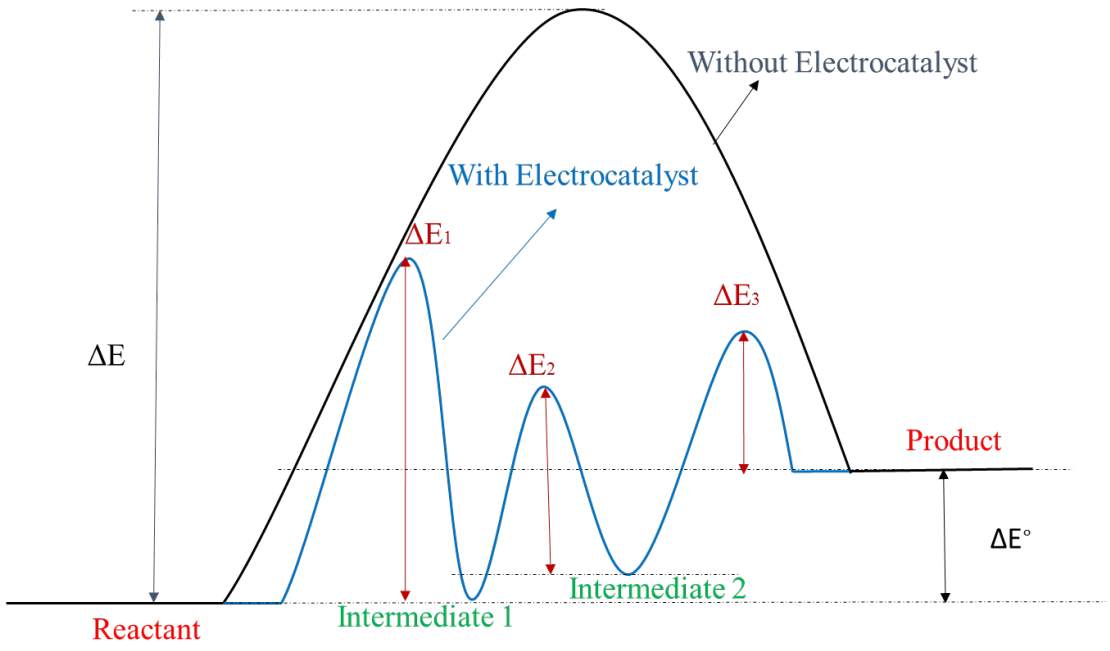

Figure 2.8 Schematic illustration of electrocatalytic reaction mechanism

The chemical/electrochemical absorption process is exothermic process. It is a crucial factor influencing electrocatalytic kinetics. To convert the reactant into the product, the reactant would be activated into intermediate states through adsorption on the catalyst surface. The strength of adsorption of the reactant determines the activity of the electrocatalyst: a moderate strength is optimal for a catalyst. If the binding is too strong, the final product or intermediate species would be very difficult to leave the catalyst surface, which hinders further reactions. On the contrary, if the absorption energy is too low, the binding between formed intermediates and catalyst surface would

be very weak, leading to a surface with a low coverage rate, making it very difficult to stabilize intermediates and hinders further reactions, too. Figure 2-9 displays the volcano plot of catalytic activity vs. the absorption energy of 1/4 monolayer of adsorbed atomic oxygen with selected metal catalysts. [27] The vertical axis gives the exchange current density of oxygen evolution reaction on a particular metal; the horizontal axis gives the Gibbs free energy of oxygen absorption on a particular metal. Metals with the highest electrocatalytic activities are located on the top of the volcano plot, which have a moderate binding strength. On these metals the reactants can bind on the catalyst surface rapidly, subsequently convert to final product and leave the catalyst without severe hinders. It can be seen, besides noble metals, Ni stands out as a promising candidates. Because Ni is reasonably close to the top of the volcano plot among all transition metals. Therefore, Ni is an excellent candidate as a base material to develop low-cost electrocatalyst material for OER.

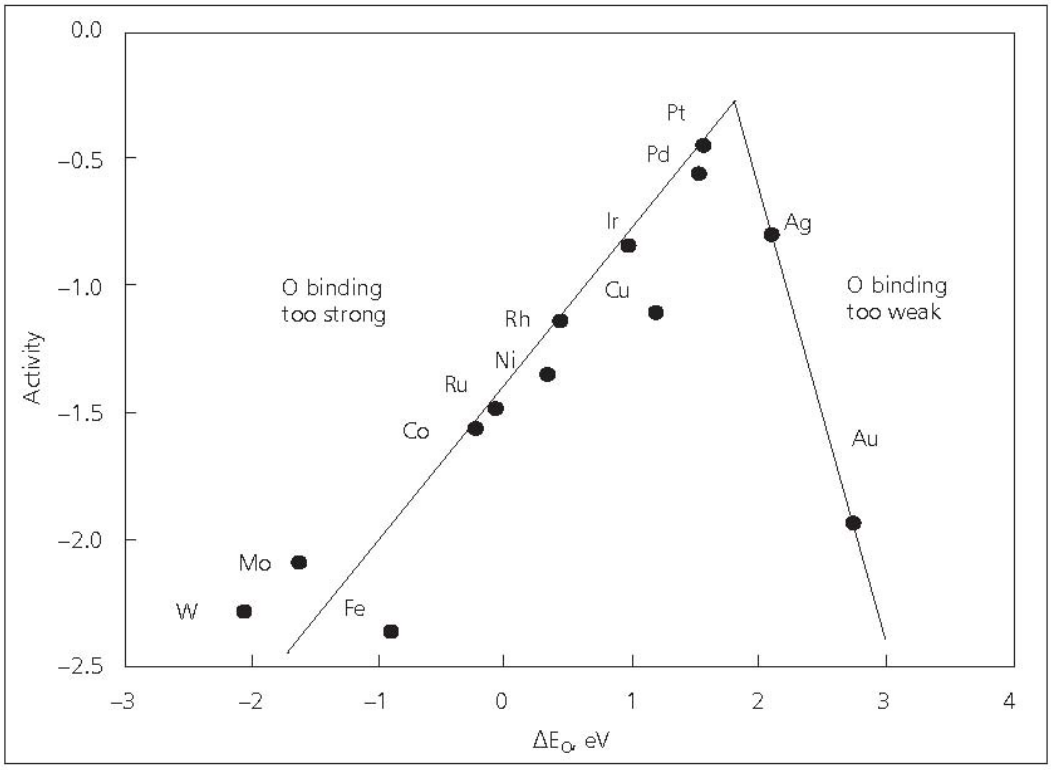

Figure 2.9 The volcano plot of activity vs. oxygen binding energy of ¼ monolayer of adsorbed atomic oxygen[27]

According to covalent bond theory, covalent bond is formed between the atoms by the hybridization of outer-layer s, p, d electron orbitals to bind electrons to a region and form energy bands with the inner orbitals and electrons unaffected. Basically, there are two types of electrochemical half-reactions: acceptor reactions and donor reactions. In a typical accepter reaction, electrons are received by the reactant from the electrode. In a donor reaction, electrons are received by the electrode from the reactant. The valence shells of metals are usually composed of s or d band. Most metals with s bands

are strong electron donors and bind strongly to electron acceptors to form very stable compound. On the contrary, d-block (IB, VIB, VIIB and VIIIB) elements are suitable electrocatalysts for many reactions. Because d-block elements have 1-2 s electrons on the outermost shell and 1-10 d electrons on the secondary outermost shell, there are unpaired electrons on the (n-1)d and/or ns orbitals. Moderate absorptions are formed between these orbitals to main group reactant with only s or p electrons, then convert the unstable intermediate into a stable state. Even for elements have fully filled d orbitals, such as Cu, Ag, Au, their d electrons can still transit to s orbital and leave an unfilled d bands. Therefore, d-block metals usually have a moderate chemical/electrochemical absorption. The percent of d orbitals in the s, p, d or d, s, p hybridization orbitals is d character factor (d %). A high d% indicate a high d band occupancy and low d band vacancy. The electrocatalytic activity is affected by the d occupancy, which is reflected by the absorption trend of the d-block metals. It is found, on the left side of a period, the binding to atomic species is strong; it was found that the rate of dissociative adsorption to molecular species increase with increasing atomic number of noble metals, which explained the volcano plots with the electronic factor.

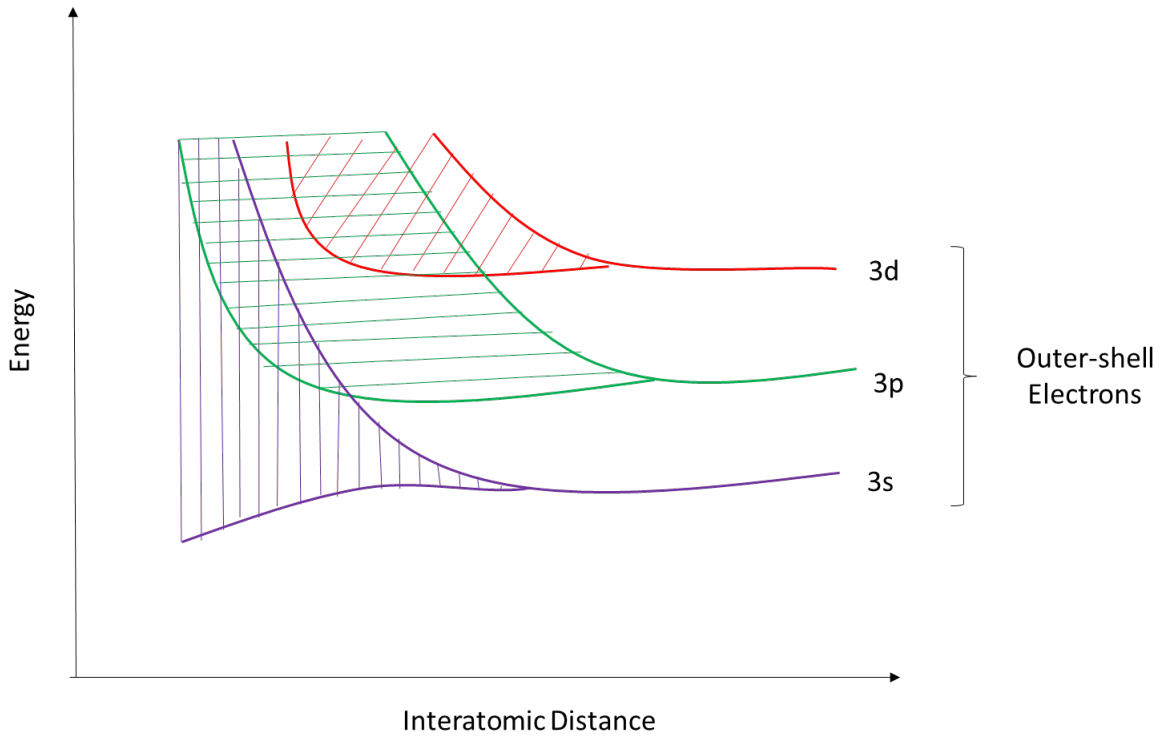

Figure 2.10 Illustration of orbital hybridization of a 3 period transition metal

Table 2.2 d% of selected d-block metals[28]

Element	Sc	Ti	V	Cr	Mn	Fe	Co	Ni	Cu	Y	Zr	Nb	Mo
d%	20	27	35	39	40.1	39.5	39.7	40	36	19	31	39	43
Element	Tc	Ru	Rh	Pd	Ag	La	Hf	Ta	W	Re	Os	Ir	Pt
d%	46	50	50	46	36	19	29	39	43	46	49	49	44

Fermi level is the top of the electron collection energy levels at 0 K. The minimum energy required to transmit an electron from the top edge of the Fermi level into vacuum is work function (Φ). Fermi level decides the strength of chemical/electrochemical absorption. For example, if the Fermi level is low, such as metals with high d-band vacancy, such as Cr, Mo, W and Mo, it has a very strong absorption to H_2 molecules, making it unsuitable for hydrogenation reactions. Metals with a low work function have a higher potential to donate electrons; metals with a high work function have a higher potential to accept electrons.

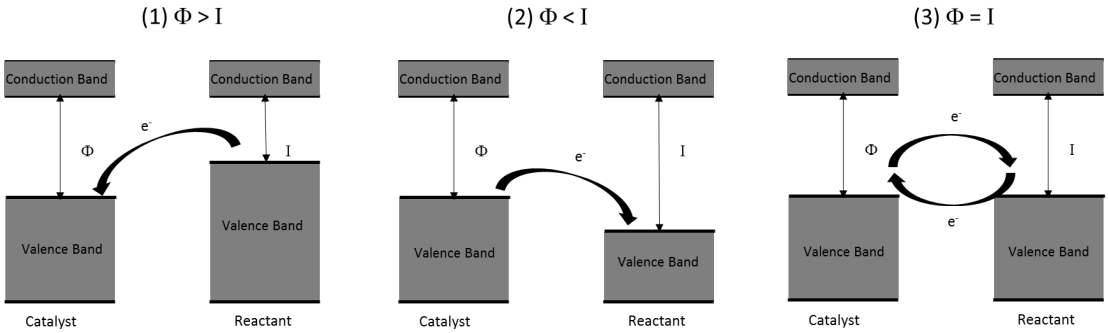

Figure 2.11 Schematic illustration of band model

The minimum energy required to transfer electrons from the reactant is I, representing the difficulty of losing electrons. When Φ > I, electrons transfers from the reactant to the surface of catalyst and reactant loses electrons. At the same time, ionic bonds form between reactant and electrocatalyst. The bond strength is determined by the difference between Φ and I. In addition, Φ is reduced by the formation of cations. On the contrary, when Φ < I, electrons transfer from the surface of catalyst to the reactant and reactant receives electrons. At the same time, ionic bonds form between reactant and electrocatalyst. The bond strength is determined by the difference between Φ and I. In addition, Φ is increased by the formation of anions. When Φ and I are very

close, complete electron transfer is unlikely to happen and valence bound forms with no absorption.

Table 2.3 Work function of selected metals[29]

Element	Sc	Ti	V	Cr	Mn	Fe	Co	Ni	Cu	Y	Zr	Nb	Mo
Work Function (eV)	3.50	4.33	4.30	4.60	4.10	4.48	4.41	4.51	4.10	3.10	4.05	3.95	4.36
Element	Al	Ru	Rh	Pd	Ag	La	Hf	Ta	W	Re	Os	Ir	Pt
Work Function (eV)	4.06	4.71	4.48	4.55	4.80	3.50	3.90	4.80	4.53	5.10	5.93	5.67	5.32

In the heterogeneous electrocatalysis reactions, only atoms on the surface are involved in interactions to reactant, with minority of the atoms serving as active centers. The interactions between catalyst atoms and reactant not only deform bonds within the reactant, but also activate some atoms and promote the formation of new bonds. Therefore, the geometric configuration of the catalyst and reactant should match. The most important steric effect on electrocatalysis is that the strength of chemical / electrochemical adsorption of reactant strongly depend on the lattice parameters. For electrocatalyst surface with large interatomic distances, the chemical bonds in the diatomic reactant have to be broken to adsorb on the electrocatalyst surface. On the contrary, if atoms are too closely packed, strong repulsion would impede adsorption. It can be seen that close packed structures usually has better activity toward oxygen evolution reaction. In addition, the coordination number of FCC and HCP are both 12 and the coordination number of BCC is 8. A higher coordination number is favorable for catalytic reaction. Therefore, it can be seen most metals with good performance for oxygen evolution reaction are in the FCC category. For single-atomic species, the lattice spacing has little effect on catalysis performance.

Table 2.4 Lattice spacing of most densely packed plane (nm) [30]

BCC {110}		**FCC {111}**		**HCP {1000}**	
Ta	0.286	Ce	0.366	Mg	0.320
W	0.272	Ag	0.288	Zr	0.312
Mo	0.272	Au	0.288	Cd	0.298
V	0.260	Al	0.286	Ti	0.292
α-Cr	0.246	Pt	0.276	Os	0.270
α-Fe	0.248	Pd	0.274	Zn	0.266
		Ir	0.270	Ru	0.266

(table cont'd)

BCC {110}	FCC {111}		HCP {1000}	
	Rh	0.268	β-Co	0.252
	Cu	0.256	Be	0.224
	α-Co	0.252		
	Ni	0.248		

The catalytic performance of an electrocatalyst also strongly depends on the nature and amount of structure defects. One typical type of s defects is point defect, including Frenkel defect and Schottky defect. Schottky defect is also called vacancy defect, whose lattice sites are vacant, but could be occupied to form perfect crystal. Frenkel defect is also called interstitial defect, where atoms occupy the areas supposed to be empty. In addition, linear defects and planar defects, also contribute to the activity of electrocatalyst. The formation of interfaces between grain boundaries enhances the electrocatalytic activities.[31-35] Another important defect source is surface imperfectness, such as corners, cavities, edges and kinks, that strongly affect the active area on catalyst surface. It has been reported the electrolysis kinetics increase with the surface step and kink intensity.[36-38]

The active surface area of solid catalyst is another important factor. The development of nanostructure can strongly enhance the activity of electrocatalyst. In the past decades, tremendous efforts have been advanced in exploring nanostructured electrocatalyst materials.[39-44] Compared to bulk materials, nanostructured materials can display improved catalytic activities due to their special morphologies.[39, 45-48] Owing to the minimization of particle sizes, the exposed surface area to volume ratio is increased, which allows the absorption of more reaction species. Therefore, the specific electrochemical current can be effectively magnified with the increased surface area. In addition, at the nanometer scale, the crystal structure tends to be more disordered. The activity of the electrocatalyst is enhanced by the multi-grained nature.[49-51] The first nanostructuring effect on electrocatalyst rising attentions was reported by Brown et al. It was discovered since the surface of alloys were usually higher than pure metal electrocatalyst, they provide higher surface area and more active catalytic sites.[52] Later on, the effect of nanostructuring on electrocatalytic activity has been demonstrated by many researchers on different material systems.[52] Moreover, it was discovered that in a gas-evolved electrochemical reaction, such as HER and OER, a nanostructured surface exhibited advantages in facilitating gas product repelling.[53-56]

2.2.2 Electrocatalyst Materials

Currently, noble metal-based electrocatalysts still play a dominating role as OER electrocatalysts, such as Iridium and ruthenium, due to their high activity toward OER both in acidic and basic environment, attributed to their empty d orbitals, leading to the s, p, d band hybridization and a high d band occupanc.[25-26] The performance of the electrocatalyst is significantly affected by the morphology of the materials. It is observed that RuO_2 is not very stable under high operating potential, and will be gradually dissolved into the electrolyte. Comparably, the stability of IrO_2 for OER is better than RuO_2.[57] To enhance the electrochemical durability of noble metal-based

OER electrocatalyst, a $Ru_xIr_{1-x}O$ compound material has been developed, resulting in an electrocatalyst possessing superior catalytic activity and durability.[58-59] In addition, hierarchical IrO_2@RuO_2 has also been studied.[60] Nevertheless, the commercialization of water splitting is severely hindered by the scarcity and high cost of these noble-metal materials. Therefore, developing affordable and efficient electrocatalyst based on earth-abundant is becoming more and more urgent.

Recently, transition metal has become an appealing category as electrocatalyst for energy conversion reactions. It is found that many transition metals are active toward OER, which are correlated to their work functions, crystal structures and electrical conductivity. For example, Wu et al. reported monolayer cobalt nanoparticle electrocatalyst on glassy carbon electrode. It presented high electron transfer facility.[61] Chaudhari et al. reported 3D nickel foam displayed great electrochemical performance due to the extended surface area and a conductive interconnected nanoporous network.[62] However, the performance of pure metals is restricted by their intrinsic properties. Research interests have been devoted to transition metal alloys, since the synergistic effect of two or more metals could change the affinity of a single metal toward reaction species. More specifically, through alloying two or more transition metals, the d-band occupancy, work function and crystal lattice spacing could be tuned.[63] Ni–Fe alloys displayed apparently advantages compared to pure metal electrocatalyst. For example, Hoang et al. reported -controlled electrodeposited NiFe films yielded and OER current density of 100 mA/cm^2 at an overpotential of ~300 mV and maintained for 72 hours.[64] Lu et al. reported electrodeposited hierarchical 3D Ni-Fe electrocatalyst only requires 200 mV onset overpotential and can receive a current density of 500 mA/cm^2 at an overpotential of 240 mV.[65]

Though transition metal oxides usually don't possess a good electrical conductivity and relatively unstable under water splitting, there are several successful families of transition metal oxide for OER. The first one is perovskite family, which has a chemical formula of ABO_3 with A representing alkaline or rare-earth metals and B representing transition metals. For example, Matsumoto et al. have developed a $La_{1-x}Sr_xFe_{1-y}Co_yO_3$ electrocatalyst system and found that its OER activity increased with increasing x and y. [66] The second one is the spinel family, which has a chemical formula of CD_2O_3 with C representing group 2 or group 13 metals and D representing transition metals. Spinel oxides usually possess good electrical conductivity and can maintain a good stability in alkaline environment. [67-68] The third one is the layer structured family. Layer structured oxides are composed of metal hydroxides and metal oxyhydroxides and its crystal structure is layered-stacking configuration with proton packed between layers, which can exhibit excellent electrocatalytic activity toward OER. For example, Gong et al. synthesized Ni-Fe layered double hydroxide nanoplates which displayed an improved catalytic activity and stability toward water oxidation compared to Ir-based electrocatalyst.[69]

Metal chalcogenides, metal pnictides and organometallic are also promising transition metal based OER electro-catalysts. Metal chalcogenides include metal sulfide and metal selenide. Most metal chalcogenide OER electrocatalyst are based on nickel or cobalt. For instance, Chen et al. have developed a NiS electrocatalyst on steel mesh

electrode and achieved a 11 mA/cm^2 current density at 297 mV with a Tafel slope of 47 mV/dec.[70] Metal pnictides consists of metal nitrides and metal phosphides. Their good performance toward OER to some degree attributes to their inert-nature under harsh chemical environment. A series of Co and Ni based metal pnictides have been tested for OER, such as Co_2N, Co_3N, Co_4N[71] and Ni_3N[72]. Organometallic is a complex system evolving oxygen and transition metals such as Mn, Fe and Co. For example, a manganese complex has been developed, exhibiting bifunctional catalytic properties toward both OER and ORR.[73]

Besides metal based electrocatalyst, non-metal electrocatalyst, especially carbon-based materials, also displays interesting behaviors in catalyzing OER. For example, nitrogen doped carbon has attracted a lot of attention. Zhao et al. developed N/C nanomaterials received 10 mA/cm^2 current density in alkaline media at an overpotential of 380 mV. [74] In addition, graphene based materials have also been tested. For example, Chen et al. fabricated a highly porous 3D graphene/CNT exhibited 5 mA/cm^2 current density at a 365 mV overpotential.[75] In addition to carbon based materials, black phosphorus is also very promising. For example, black phosphorus developed through the method of thermal vaporization transformation displayed a comparable performance to RuO_2 electrocatalyst.[39]

2.2.3 Challenges and Strategies

For OER electrocatalyst based on earth-abundant elements, to receive comparable performance to noble metal based electrocatalysts, there are several challenges in the front. Firstly, the material is required to have a good intrinsic catalytic activity. Though further composition and structure modifications could improve the performance to some degree, the material intrinsic activity is a decisive factor. Secondly, the material needs to be stable under the water electrolysis conditions to maintain a long-term performance without severe degradation. An ideal electrocatalyst could resist the corrosion both under bias voltage and standby conditions. Therefore, due to the high activity of most earth-abundant elements, the task of stable electrocatalyst is becoming even more difficult. However, this long-time stability issue might be relaxed for materials that is very low-cost and can be replaced easily. Thirdly, the materials should have excellent properties including good electrical conductivity, environmental compatibility and structural tunability. The electrocatalyst should have a rapid electron transfer to ensure the minimized ohmic efficiency losses. In addition, the earth-abundant elements based electrocatalysts should also be compatible to the water electrolysis environment to avoid corrosion and poisoning during operation, nor should they contaminate or degrade other. Fourthly, an ideal electrocatalyst should exhibit high activity and stability toward wide range of electrochemical reactions, like the some noble metals.

There are several strategies in achieving excellent electrocatalysts, that are aimed to increasing the activity or/and stability of the electrocatalyst. Firstly, nanostructure is the most straightforward strategy, since it can effectively improve the current by magnify active surface area to volume ratio of the electrocatalyst that results in a multiplied number of exposed active sites. In addition, the nanostructured surface can somewhat facilitate gas bubble release and promote mass diffusion. Moreover,

nanostructure electrocatalyst templates and substrates are also very important. Secondly, chemical composition modifications play a key role in improving the activity. Though the intrinsic activity of an element is unchangeable, the effects of a composite species in increasing the overall activity are significant. Doping, alloying are both effective in altering catalyst electronic structures, which can change the Fermi levels or oxidation state and improving electrocatalytic activity. Thirdly, modifying the microstructure is crucial to catalyst performance. The different crystallinities of a same material could contribute to sites with varied activity.

2.3 Laser-based Additive Manufacturing

2.3.1 Introduction to Laser-based Additive Manufacturing

Recently, laser-based additive manufacturing has received tremendous attention from both academia and industrial bodies[76-80]. As a prototyping manufacturing method, laser-based additive manufacturing is the process of joining materials to make 3D parts layer by layer. It has lately enormously progressed becoming an established fabrication technique to 3D-print a variety of functional materials.[81-82] Through a repeated layer-by-layer process, the laser-based additive manufacturing process is able to build a 3D-structured metal part. In a typical laser-based manufacturing process, a layer is formed by melting a selective area of powders. During irradiation of a laser beam, the powder is heated over its melting point and a liquid molten pool is formed. The molten pool solidifies quickly and forms a single sintered metal or alloy track. To build a 3D part, before starting the laser melting process, the first step is to load the 3D CAD design to the software to slice it into many layers with the same thickness of ~ 20-100 micrometers to generate a set of 2D plane image for each layer. Then each file is uploaded to the geometry control software sequentially. A layer of ~20-100 micrometers metal powders is uniformly laid on the substrate or the previous layer in the inert gas filled chamber. Then the laser with an ultrahigh energy density scans on the powder according to the geometry of each layer to melt the powder selectively. After one layer is melted, the stage will move down along the Z direction. This process is repeated layer by layer successively for 3D part construction until the last layer is printed. When the laser-based manufacturing process is finished, the unmelt powders are separated from the 3D part manually.[83-84] Currently, Yb:YAG crystal is one of the most used laser source due to its relatively higher absorption rate by metals. The quality of the part produced by laser-based manufacturing is affected by several parameters, including the energy density of the laser, the hatch space between each molten track, scanning speed, the thickness of each layer and the metallic power properties. Under the condition of a lower laser power, wider molten track spacing, faster scanning speed, insufficient melting might be resulted with significant balling and porousity.[85] On the contrary, excessive low scanning speed and high laser energy could cause increased manufacturing cost. Generally, powders have a much higher laser energy absorption rate compared to its bulk material, owing to its higher surface area to volume ratio and multi-direction wave refelection.[86] Also, a more even distributed laser beam could lead to wider molten pool.[87] To increase the layer density at the same laser power, decrease the powder diameter and the particle size variance are effective stratgies.[88] Balling is

another issue that occurs during laser-based manufacturing process, which severely decreases molten track uniformity and roughens the layer surface. It is reported the formation of surface oxide causing the wetting of liquid metal on the preceding layer very difficult that may lead to layer delamination. Therefore, minimizing oxygen content in the laser-based additive manufacturing chamber and repeating laser shining to reduce metal oxide layers are necessary processes. In addition, due to thermal properties of different metals, materials suffers from residue stress from the temperature fluctuation in the melting and cooling process.[89] To date, several strategies have been proved effective in reduce the residue stress of laser-based manufacturing components. The first one is post heat treatment at 600 to 700 °C for 1 hour, which can release 70% residue stress. The second one is scanning each layer with the same operating condition for a second time, which can release 55% residue stress. The third one is to preheat the stage to 160°C, which can reduce 40% residue stress.[90] Also, it is reported sectorial scanning is another effective strategy to reduce residual stress, which divides each scanning layer into many small square area and each square is scanned perpendicular to its neighbors. [91] In the past two decades, more and more research efforts have been devoted to the investigation of laser-based manufacturing techniques and materials. To date, the most studied laser-based manufactured materials include iron-based alloy, titanium-based alloy, nickel-based alloy and aluminum-based alloy. Different steels have been studied, such as SS316L, and inox904L, as well as many intermetallic materials such as FeNi alloy, FeAl alloy. Besides commercial Ti based material, such as pure titanium and Ti64, other titanium-bases alloy, such as Ti-6Al-7Nb and Ti-24Nb-4Zr-8Sn have also been printed by laser-based manufacturing. Compared to iron-based materials, titanium-based materials possess higher specific strength and elastic moduli that is more suitable for human body implants.[92-93] Nowadays, laser-based manufacturing has been applied to various applications to develop metal or alloy parts requiring complicated 3D structures, such as a structure consisting of small channels or a structure containing interconnected parts. Laser-based manufacturing also has some disadvantages. Firstly, the printing of 3D structure through laser-based manufacturing process usually needs a large amount of metal powders. The metal powders remaining in the un-selected areas will cause the waste of materials. Secondly, laser-based manufacturing is a time intensive technique, slower and more complicated compared to traditional casting.[94] Laser-based manufactured parts usually have a better strength and low malleability, due to its relatively more uniform structure at each laser spot.[95] However, the quality of laser manufactured parts is limited by its high surface roughness and porosity.[96-97] With the development of laser-based manufacturing technique, its application is becoming wider and wider. One main application for laser processed metal/alloy material is on biomedical and dental parts. Since laser-based additive manufacturing can directly develop metal parts for different individual's specific needs with materials biocompatible for human bodies. It is able to develop body implants to replace various body parts or serving as supporting structures.[98-99] Another application of laser-based manufacturing is to develop heat exchanger components, due to its high feasibility in achieving uniform heat exchanging channels to very small sizes with very complicated structures.[100] At the same time, laser-based additive manufacturing is able to develop 3D single cell or honeycomb structured lightweight parts with complex lattice and ultrathin wall thickness, allows the

possibility of lowering the weight of the product.[101-102] Lately, novel materials for energy applications, especially materials with specific energy storage and conversion activities have attracted a lot of attentions, such as phase change materials for thermal energy storage applications[103], lithium ion battery anode materials[104], photoanode materials for solar cells[105], catalyst platform for water splitting [106]. Compared to traditional electrocatalyst synthesis methods, which not only requires a tedious synthesis to receive desired catalyst composition or structure, but also needs a careful control of supporting platform/electrode and binder properties, laser-based additive manufacturing can develop 3D structures freely, and effectively enhance the adhesion between active layer and substrate, making the development of novel electrocatalyst more efficient and flexible. On modern photovoltaic market, thin film solar cell has gradually come to stage. Compared to first and second generation solar cells, thin film solar cells are more flexible and compatible to different constructions. Dye-sensitized solar cell is one of the most important third-generation solar cell, which using sensitized TiO_2 nanoparticle on FTO substrate as the photoanode. The preparation of TiO_2 photoanode requires a high temperature of 500 °C for electrode sintering, which limits its application on conductive polymer substrates. Laser-based manufacturing has been considered as a promising technique to post-anneal TiO_2 electrode on polymer substrate, which on one hand can provide through sintering of the nanoparticles with sufficient adhesion to the polymer substrate, on the other hand can perfectly protect the surface of the substrate from damaging. [105] Nowadays, lithium ion battery has become one of the most popular energy storage devices. Recently, the research interest on lithium ion battery electrode material has been moved to thin film structures, which have displayed higher charge capacity compared to powder-based electrode materials. [107-108] Compared to traditional powder electrode preparing process, which not only requires multiple-stepped chemical synthesis, but also requires a process for electrode ink preparation and electrode coating, laser-based manufacturing only needs one-step rapid printing process for self-stand electrode. Currently laser-based manufacturing is available to print materials with various components, which significantly facilitates the research on thin film battery electrode preparations. It has been reported, laser processed Mg based anode materials for lithium ion battery has displayed superior capacity and stability, which may pave a new way for the battery industry.[104] Laser-based manufacturing has also been researched on fabricating novel complex-structured metallic components, such as bulk metallic glasses (BMGs) for methyl- orange catalytic degradation.[109] Since BGM materials always require a fast cooling to develop amorphous structure, copper-mold casting is the most used fabrication method. However this method doesn't allow small and complex structure formation[110-111]. Furthermore, traditional manufacturing techniques are facing the problem of intrinsic brittleness and high hardness, and BGM materials made of the conventional techniques are lack of strength, elasticity and corrosion resistance.[112-113] Though squeezing casting and thermal plastic forming are able to produce BMGs, they haven't achieved BMG with complex three dimensional structures sucessfully.[114-115] During laser-based manufacturing process, the laser scanning is on a very thin layer, the cooling is usually very fast, which is higher than the critical cooling rate of amorphous structures for BMG romation.[116-117] In addition, laser-based manufacturing allows the development of very complex structures at very small scale. $Zr_{55}Cu_{30}Al_{10}Ni_5$ BGM has been successfully developed by laser-based

manufacturing with various structures and the nanoporous Cu derived by post dealloying process of BGM demonstrated superior catalytic activity and stability toward methyl-orange degradation.[109] In addition, applying laser-based manufacturing to print 3D conductive parts, which are either functional materials or platforms for functional layer coating to, is especially appealing in the chemical and electrochemical energy conversion areas. Recently a self-contained electrochemical platform has been developed for water electrolysis.[106] This system consists of electrodes and the cell printed by laser process, followed by electrodeposition of active material coating.

2.3.2 Microstructures and Defects

Laser processed alloys usually experience special thermal cycles that could produce anisotropic and heterogeneous microstructures significantly different from parts made by traditional casting. Firstly, a certain area absorbs energy from the laser source and heated to a temperature above its melting point rapidly. Then, the molten pool experiences a rapid solidification as the laser scan moving on. Later on, re-heating and re-cooling is processed on this area with the producing of following layers.[118-119]. Thus, due to the high cooling rate and directional solidification, the products from laser-based manufacturing may contain highly metastable microstructures, such as elongated crystalline, solute trapping and more metallurgical defects, such as high porosity, gas trapping and balling.[120] In additions, the laser processed alloys usually have an exposed surface with molten tracks, protruding particles and small concaves. Therefore, the electrochemical performance of laser-based manufactured alloy may differ significantly from traditionally processed alloys and can provide an interesting insight on novel alloy electrocatalyst fabrication.

A major source of structure defects is due to lack-of-fusion, which could results in defect size from 50 to 500 μm. [121]. A post heat treatment or slower cooling down rate are common methods to minimize such defects.[122]. Usually, at different locations of a laser-processed part, the phase constitution and geometry are varied. The microstructures depend on the manufacturing parameters and raw materials.[123-124] For example, the microstructure accuracy decreases with increasing cooling rate.[125] Pore defects with the size of 10 to 50 μm are found due to the trapped gas in the raw material.[120, 126] Decreasing the scanning speed can allow the escaping of trapped gas and effectively decrease the part porosity.[127] In addition, unmelted powders and layer gaps are also source of defects. The temperature gradient is affected by many factors such as laser energy density, thermal conductivity of each component in the alloy, the geometry of the produced part and the surrounding environment. Firstly, the laser beam size is decisive to the accuracy of the parts' geometry. [128] A larger beam size would result in more equiaxed grains due to the larger melting pool. Secondly, the surrounding environment is another important factor. The physical absorption and chemical bonding with surrounding gasses might impact the properties of the product. Therefore, inert gas environment are applied for the manufacturing process. Thirdly, substrate temperature can affect the microstructure. Usually, a low temperature can increase the homogeneity of the microstructure, but increase the residual stress.[129] Lastly, the raw material properties can also affect the density of the final parts. Apparently, the laser power

density is one of the most important factors. The relationship between porosity and laser energy density is shown is Fig. 2-12. The laser energy density is expressed as:

$$E = \frac{P}{vdt}$$

Where: E is the energy density per unit volume;

v is laser scan speed;

d is the hatch spacing;

t is the layer thickness.

As displayed in Fig. 2-12, at a high scan speed and lower laser power, the laser energy density is insufficient; the melting is highly uncompleted and a high porosity is formed (zone I). In zone II, the laser energy density is proper to produce a fully dense part. If the scan speed is too low, excess energy will cause an over melting.

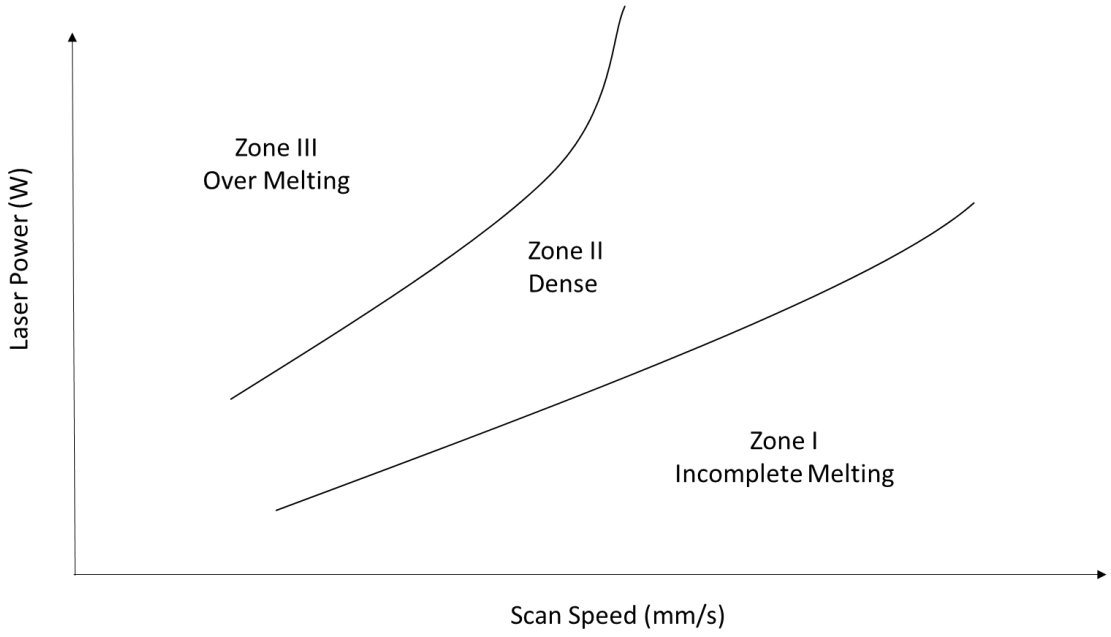

Figure 2.12 Melting zones of laser-based manufacturing

2.4 References

1. Sato, M., Thermochemistry of the formation of fossil fuels. *Spec. Publ. - Geochem. Soc.* **1991,** *2* (Fluid-Miner. Interact.), 271-83.

2. Halbouty, M. T.; Editor, *Giant Oil & Gas Fields of the Decade-1990-99*. AAPG: 2005; p 340 pp.

3. Ball, M. W., *This Fascinating Oil Business*. Bobbs-Merrill Co.: p 444 pp.

4. Cui, X.; Xu, W.; Xie, Z.; Wang, Y., Hierarchical SnO2@SnS2 Counter Electrodes for Remarkable High-efficiency Dye-sensitized Solar Cells. *Electrochimica Acta* **2015,** *186*, 125-132.

5. Cui, X.; Xie, Z.; Wang, Y., Novel CoS2 embedded carbon nanocages by direct sulfurizing metal-organic frameworks for dye-sensitized solar cells. *Nanoscale* **2016,** *8* (23), 11984-11992.

6. Wang, Z.; Spivey, J. J., Effect of ZrO2, Al2O3 and La2O3 on cobalt–copper catalysts for higher alcohols synthesis. *Applied Catalysis A: General* **2015,** *507* (Supplement C), 75-81.

7. Wang, Z.; Laddha, G.; Kanitkar, S.; Spivey, J. J., Metal organic framework-mediated synthesis of potassium-promoted cobalt-based catalysts for higher oxygenates synthesis. *Catalysis Today* **2017,** *298* (Supplement C), 209-215.

8. Last, J.; Guidotti, T. L., Implications for human health of global ecological changes. *Public Health Rev* **1990,** *18* (1), 49-67; discussion 69-72.

9. Mora, C.; Frazier, A. G.; Longman, R. J.; Dacks, R. S.; Walton, M. M.; Tong, E. J.; Sanchez, J. J.; Kaiser, L. R.; Stender, Y. O.; Anderson, J. M.; Ambrosino, C. M.; Fernandez-Silva, I.; Giuseffi, L. M.; Giambelluca, T. W., The projected timing of climate departure from recent variability. *Nature (London, U. K.)* **2013,** *502* (7470), 183-187.

10. Mann, M. E., Earth Will Cross the Climate Danger Threshold by 2036. *Scientific American* **2016**.

11. Hodgson, P. E., Global warming and nuclear power. *Nucl. Energy (Br. Nucl. Energy Soc.)* **1999,** *38* (3), 147-151.

12. https://www.ecotricity.co.uk/our-green-energy/energy-independence/the-end-of-fossil-fuels.

13. Boden, T. A., G. Marland, and R.J. Andres. , Global, Regional, and National Fossil-Fuel CO2 Emissions. Carbon Dioxide Information Analysis Center, Oak Ridge National Laboratory, U.S. Department of Energy, Oak Ridge, Tenn., U.S.A. **2017.**

14. https://en.wikipedia.org/wiki/Renewable_energy.

15. Bossel, U., Does a hydrogen economy make sense? *Proc. IEEE* **2006,** *94* (10), 1826-1837.

16. Greeley, J.; Jaramillo, T. F.; Bonde, J.; Chorkendorff, I.; Norskov, J. K., Computational high-throughput screening of electrocatalytic materials for hydrogen evolution. *Nat. Mater.* **2006,** *5* (11), 909-913.

17. Jaramillo, T. F.; Jorgensen, K. P.; Bonde, J.; Nielsen, J. H.; Horch, S.;

Chorkendorff, I., Identification of Active Edge Sites for Electrochemical H2 Evolution from MoS2 Nanocatalysts. *Science (Washington, DC, U. S.)* **2007,** *317* (5834), 100-102.

18. Li, Y.; Wang, H.; Xie, L.; Liang, Y.; Hong, G.; Dai, H., MoS2 Nanoparticles Grown on Graphene: An Advanced Catalyst for the Hydrogen Evolution Reaction. *J. Am. Chem. Soc.* **2011,** *133* (19), 7296-7299.

19. de Levie, R., The electrolysis of water. *Journal of Electroanalytical Chemistry* **1999,** *476* (1), 92-93.

20. Carmo, M.; Fritz, D. L.; Mergel, J.; Stolten, D., A comprehensive review on PEM water electrolysis. *Int. J. Hydrogen Energy* **2013,** *38* (12), 4901-4934.

21. Bard, A. J.; Faulkner, L. R., Electrochemical Methods: fundamentals and applications. *Dianhuaxue* **2001,** *7* (2), 255.

22. Fletcher, S.; Inzelt, G.; Scholz, F., Electrochemistry-past, present, and future. *J. Solid State Electrochem.* **2011,** *15* (7-8), 1295-1296.

23. Liu, R.-S.; Zheng, L.; Sun, X.; Liu, H.; Zhang, J.; Editors, *Electrochemical Technologies for Energy Storage and Conversion, Volume 1*. Wiley-VCH Verlag GmbH & Co. KGaA: 2012; p 382 pp.

24. Zou, X.; Zhang, Y., Noble metal-free hydrogen evolution catalysts for water splitting. *Chemical Society Reviews* **2015,** *44* (15), 5148-5180.

25. Reier, T.; Oezaslan, M.; Strasser, P., Electrocatalytic Oxygen Evolution Reaction (OER) on Ru, Ir, and Pt Catalysts: A Comparative Study of Nanoparticles and Bulk Materials. *ACS Catal.* **2012,** *2* (8), 1765-1772.

26. Lee, Y.; Suntivich, J.; May, K. J.; Perry, E. E.; Shao-Horn, Y., Synthesis and Activities of Rutile IrO2 and RuO2 Nanoparticles for Oxygen Evolution in Acid and Alkaline Solutions. *J. Phys. Chem. Lett.* **2012,** *3* (3), 399-404.

27. Nørskov, J. K.; Rossmeisl, J.; Logadottir, A.; Lindqvist, L.; Kitchin, J. R.; Bligaard, T.; Jónsson, H., Origin of the Overpotential for Oxygen Reduction at a Fuel-Cell Cathode. *The Journal of Physical Chemistry B* **2004,** *108* (46), 17886-17892.

28. http://webcache.googleusercontent.com/search?q=cache:BJBinglxVAcJ:staff.ustc.edu.cn/~huangwx/CN/courses-CN.files/chapter07-catalysisbymetals.ppt+&cd=1&hl=en&ct=clnk&gl=us.

29. https://wenku.baidu.com/view/8dbb4d8fcc22bcd126ff0c54.html.

30. Hagen, J., Heterogeneous Catalysis: Fundamentals. In *Industrial Catalysis*, Wiley-VCH Verlag GmbH & Co. KGaA: 2015; pp 99-210.

31. Sieben, J. M.; Duarte, M. M. E., Nanostructured Pt and Pt–Sn catalysts supported on oxidized carbon nanotubes for ethanol and ethylene glycol electro-oxidation. *International Journal of Hydrogen Energy* **2011,** *36* (5), 3313-3321.

32. Maillard, F.; Bonnefont, A.; Chatenet, M.; Guétaz, L.; Doisneau-Cottignies, B.; Roussel, H.; Stimming, U., Effect of the structure of Pt–Ru/C particles on COad monolayer vibrational properties and electrooxidation kinetics. *Electrochimica Acta* **2007,** *53* (2), 811-822.

33. Kuznetsov, A. N.; Simonov, P. A.; Zaikovskii, V. I.; Parmon, V. N.; Savinova, E. R., Temperature effects in carbon monoxide and methanol electrooxidation on platinum–ruthenium: influence of grain boundaries. *Journal of Solid State Electrochemistry* **2013,** *17* (7), 1903-1912.

34. Wang, G.; Takeguchi, T.; Muhamad, E. N.; Yamanaka, T.; Ueda, W., Investigation of grain boundary formation in PtRu/C catalyst obtained in a polyol process with post-treatment. *International Journal of Hydrogen Energy* **2011,** *36* (5), 3322-3332.

35. Ma, Y.; Wang, H.; Ji, S.; Linkov, V.; Wang, R., PtSn/C catalysts for ethanol oxidation: The effect of stabilizers on the morphology and particle distribution. *Journal of Power Sources* **2014,** *247*, 142-150.

36. Kuzume, A.; Herrero, E.; Feliu, J. M., Oxygen reduction on stepped platinum surfaces in acidic media. *Journal of Electroanalytical Chemistry* **2007,** *599* (2), 333-343.

37. Gómez–Marín, A. M.; Feliu, J. M., Role of oxygen-containing species at Pt(111) on the oxygen reduction reaction in acid media. *Journal of Solid State Electrochemistry* **2015,** *19* (9), 2831-2841.

38. Maciá, M. D.; Campiña, J. M.; Herrero, E.; Feliu, J. M., On the kinetics of oxygen reduction on platinum stepped surfaces in acidic media. *Journal of Electroanalytical Chemistry* **2004,** *564*, 141-150.

39. Qianqian, J.; Lei, X.; Ning, C.; Han, Z.; Liming, D.; Shuangyin, W., Facile Synthesis of Black Phosphorus: an Efficient Electrocatalyst for the Oxygen Evolving Reaction. *Angewandte Chemie* **2016,** *128* (44), 14053-14057.

40. Xu, C.; Wang, X.; Zhu, J., Graphene-Metal Particle Nanocomposites. *J. Phys. Chem. C* **2008,** *112* (50), 19841-19845.

41. Tian, Z.-Q.; Ren, B.; Wu, D.-Y., Surface-Enhanced Raman Scattering: From Noble to Transition Metals and from Rough Surfaces to Ordered Nanostructures. *J. Phys. Chem. B* **2002,** *106* (37), 9463-9483.

42. Seger, B.; Kamat, P. V., Electrocatalytically Active Graphene-Platinum Nanocomposites. Role of 2-D Carbon Support in PEM Fuel Cells. *J. Phys. Chem. C*

2009, *113* (19), 7990-7995.

43. Rolison, D. R., Catalytic nanoarchitectures - The importance of nothing and the unimportance of periodicity. *Science (Washington, DC, U. S.)* **2003,** *299* (5613), 1698-1702.

44. Joo, S. H.; Choi, S. J.; Oh, I.; Kwak, J.; Liu, Z.; Terasaki, O.; Ryoo, R., Ordered nanoporous arrays of carbon supporting high dispersions of platinum nanoparticles. *Nature (London, U. K.)* **2001,** *412* (6843), 169-172.

45. Wu, G.; Zelenay, P., Nanostructured nonprecious metal catalysts for oxygen reduction reaction. *Acc. Chem. Res.* **2013,** *46* (8), 1878-1889.

46. Peng, Z.; Yang, H., Designer platinum nanoparticles: control of shape, composition in alloy, nanostructure and electrocatalytic property. *Nano Today* **2009,** *4* (2), 143-164.

47. Matter, P. H.; Zhang, L.; Ozkan, U. S., The role of nanostructure in nitrogen-containing carbon catalysts for the oxygen reduction reaction. *J. Catal.* **2006,** *239* (1), 83-96.

48. Bing, Y.; Liu, H.; Zhang, L.; Ghosh, D.; Zhang, J., Nanostructured Pt-alloy electrocatalysts for PEM fuel cell oxygen reduction reaction. *Chem. Soc. Rev.* **2010,** *39* (6), 2184-2202.

49. Maillard, F.; Schreier, S.; Hanzlik, M.; Savinova, E. R.; Weinkauf, S.; Stimming, U., Influence of particle agglomeration on the catalytic activity of carbon-supported Pt nanoparticles in CO monolayer oxidation. *Physical Chemistry Chemical Physics* **2005,** *7* (2), 385-393.

50. Mayrhofer, K. J. J.; Arenz, M.; Blizanac, B. B.; Stamenkovic, V.; Ross, P. N.; Markovic, N. M., CO surface electrochemistry on Pt-nanoparticles: A selective review. *Electrochimica Acta* **2005,** *50* (25), 5144-5154.

51. Dubau, L.; Nelayah, J.; Moldovan, S.; Ersen, O.; Bordet, P.; Drnec, J.; Asset, T.; Chattot, R.; Maillard, F., Defects do Catalysis: CO Monolayer Oxidation and Oxygen Reduction Reaction on Hollow PtNi/C Nanoparticles. *ACS Catalysis* **2016,** *6* (7), 4673-4684.

52. Brown, D. E.; Mahmood, M. N.; Turner, A. K.; Hall, S. M.; Fogarty, P. O., Low overvoltage electrocatalysts for hydrogen evolving electrodes. *International Journal of Hydrogen Energy* **1982,** *7* (5), 405-410.

53. Faber, M. S.; Dziedzic, R.; Lukowski, M. A.; Kaiser, N. S.; Ding, Q.; Jin, S., High-Performance Electrocatalysis Using Metallic Cobalt Pyrite (CoS2) Micro- and Nanostructures. *J. Am. Chem. Soc.* **2014,** *136* (28), 10053-10061.

54. Wang, X.; Huang, X.; Gao, W.; Tang, Y.; Jiang, P.; Lan, K.; Yang, R.; Wang, B.;

Li, R., Metal-organic framework derived CoTe2 encapsulated in nitrogen-doped carbon nanotube frameworks: a high-efficiency bifunctional electrocatalyst for overall water splitting. *J. Mater. Chem. A* **2018,** *6* (8), 3684-3691.

55. Yu, L.; Zhou, H.; Sun, J.; Mishra, I. K.; Luo, D.; Yu, F.; Yu, Y.; Chen, S.; Ren, Z., Amorphous NiFe layered double hydroxide nanosheets decorated on 3D nickel phosphide nanoarrays: a hierarchical core-shell electrocatalyst for efficient oxygen evolution. *J. Mater. Chem. A* **2018**, Ahead of Print.

56. Zhang, G.; Yuan, J.; Yan, L.; Lu, W.; Fu, N.; Li, W.; Huang, H., Boosting Oxygen Evolution Reaction in Non-Precious Catalyst by Structural and Electronic Engineering. *J. Mater. Chem. A* **2018**, Ahead of Print.

57. Cherevko, S.; Geiger, S.; Kasian, O.; Kulyk, N.; Grote, J.-P.; Savan, A.; Shrestha, B. R.; Merzlikin, S.; Breitbach, B.; Ludwig, A.; Mayrhofer, K. J. J., Oxygen and hydrogen evolution reactions on Ru, RuO2, Ir, and IrO2 thin film electrodes in acidic and alkaline electrolytes: A comparative study on activity and stability. *Catal. Today* **2016,** *262*, 170-180.

58. Marshall, A. T.; Haverkamp, R. G., Electrocatalytic activity of IrO2-RuO2 supported on Sb-doped SnO2 nanoparticles. *Electrochim. Acta* **2010,** *55* (6), 1978-1984.

59. Owe, L.-E.; Tsypkin, M.; Wallwork, K. S.; Haverkamp, R. G.; Sunde, S., Iridium-ruthenium single phase mixed oxides for oxygen evolution: Composition dependence of electrocatalytic activity. *Electrochim. Acta* **2012,** *70*, 158-164.

60. Audichon, T.; Napporn, T. W.; Canaff, C.; Morais, C.; Comminges, C.; Kokoh, K. B., IrO2 Coated on RuO2 as Efficient and Stable Electroactive Nanocatalysts for Electrochemical Water Splitting. *J. Phys. Chem. C* **2016,** *120* (5), 2562-2573.

61. Wu, L.; Li, Q.; Wu, C. H.; Zhu, H.; Mendoza-Garcia, A.; Shen, B.; Guo, J.; Sun, S., Stable Cobalt Nanoparticles and Their Monolayer Array as an Efficient Electrocatalyst for Oxygen Evolution Reaction. *Journal of the American Chemical Society* **2015,** *137* (22), 7071-7074.

62. Chaudhari, N. K.; Jin, H.; Kim, B.; Lee, K., Nanostructured materials on 3D nickel foam as electrocatalysts for water splitting. *Nanoscale* **2017,** *9* (34), 12231-12247.

63. Pletcher, D., Electrocatalysis: present and future. *Journal of Applied Electrochemistry* **1984,** *14* (4), 403-415.

64. Hoang, T. T. H.; Gewirth, A. A., High Activity Oxygen Evolution Reaction Catalysts from Additive-Controlled Electrodeposited Ni and NiFe Films. *ACS Catalysis* **2016,** *6* (2), 1159-1164.

65. Lu, X.; Zhao, C., Electrodeposition of hierarchically structured three-dimensional nickel–iron electrodes for efficient oxygen evolution at high current

densities. *Nature Communications* **2015,** *6*, 6616.

66. Matsumoto, Y.; Yamada, S.; Nishida, T.; Sato, E., Oxygen Evolution on La1 − x Sr x Fe1 − y Co y O 3 Series Oxides. *Journal of The Electrochemical Society* **1980,** *127* (11), 2360-2364.

67. Ma, T.; Li, C.; Chen, X.; Cheng, F.; Chen, J., Spinel cobalt-manganese oxide supported on non-oxidized carbon nanotubes as a highly efficient oxygen reduction/evolution electrocatalyst. *Inorganic Chemistry Frontiers* **2017,** *4* (10), 1628-1633.

68. Maiyalagan, T.; Jarvis, K. A.; Therese, S.; Ferreira, P. J.; Manthiram, A., Spinel-type lithium cobalt oxide as a bifunctional electrocatalyst for the oxygen evolution and oxygen reduction reactions. *Nature Communications* **2014,** *5*, 3949.

69. Gong, M.; Li, Y.; Wang, H.; Liang, Y.; Wu, J. Z.; Zhou, J.; Wang, J.; Regier, T.; Wei, F.; Dai, H., An Advanced Ni–Fe Layered Double Hydroxide Electrocatalyst for Water Oxidation. *Journal of the American Chemical Society* **2013,** *135* (23), 8452-8455.

70. Chen, J. S.; Ren, J.; Shalom, M.; Fellinger, T.; Antonietti, M., Stainless Steel Mesh-Supported NiS Nanosheet Array as Highly Efficient Catalyst for Oxygen Evolution Reaction. *ACS Applied Materials & Interfaces* **2016,** *8* (8), 5509-5516.

71. Chen, P.; Xu, K.; Tong, Y.; Li, X.; Tao, S.; Fang, Z.; Chu, W.; Wu, X.; Wu, C., Cobalt nitrides as a class of metallic electrocatalysts for the oxygen evolution reaction. *Inorganic Chemistry Frontiers* **2016,** *3* (2), 236-242.

72. Xu, K.; Chen, P.; Li, X.; Tong, Y.; Ding, H.; Wu, X.; Chu, W.; Peng, Z.; Wu, C.; Xie, Y., Metallic Nickel Nitride Nanosheets Realizing Enhanced Electrochemical Water Oxidation. *Journal of the American Chemical Society* **2015,** *137* (12), 4119-4125.

73. McCrory, C. C. L.; Jung, S.; Ferrer, I. M.; Chatman, S. M.; Peters, J. C.; Jaramillo, T. F., Benchmarking Hydrogen Evolving Reaction and Oxygen Evolving Reaction Electrocatalysts for Solar Water Splitting Devices. *Journal of the American Chemical Society* **2015,** *137* (13), 4347-4357.

74. Zhao, Y.; Nakamura, R.; Kamiya, K.; Nakanishi, S.; Hashimoto, K., Nitrogen-doped carbon nanomaterials as non-metal electrocatalysts for water oxidation. *Nature Communications* **2013,** *4*, 2390.

75. Sheng, C.; Jingjing, D.; Mietek, J.; Shi□Zhang, Q., Nitrogen and Oxygen Dual□Doped Carbon Hydrogel Film as a Substrate□Free Electrode for Highly Efficient Oxygen Evolution Reaction. *Advanced Materials* **2014,** *26* (18), 2925-2930.

76. Sing, S. L.; An, J.; Yeong, W. Y.; Wiria, F. E., Laser and electron-beam powder-bed additive manufacturing of metallic implants: A review on processes, materials and designs. *J. Orthop. Res.* **2016,** *34* (3), 369-385.

77. Murr, L. E.; Martinez, E.; Amato, K. N.; Gaytan, S. M.; Hernandez, J.; Ramirez, D. A.; Shindo, P. W.; Medina, F.; Wicker, R. B., Fabrication of Metal and Alloy Components by Additive Manufacturing: Examples of 3D Materials Science. *J. Mater. Res. Technol.* **2012,** *1* (1), 42-54.

78. Mota, C.; Puppi, D.; Chiellini, F.; Chiellini, E., Additive manufacturing techniques for the production of tissue engineering constructs. *J. Tissue Eng. Regener. Med.* **2015,** *9* (3), 174-190.

79. Pape, F.; Noelke, C.; Kaierle, S.; Haferkamp, H.; Gesing, T. M., Influence of Foaming Agents on Laser Based Manufacturing of Closed-cell Ti Foam. *Procedia Mater. Sci.* **2014,** *4*, 97-102.

80. Brueckner, F.; Seidel, A.; Straubel, A.; Willner, R.; Leyens, C.; Beyer, E., Laser-based manufacturing of components using materials with high cracking susceptibility. *J. Laser Appl.* **2016,** *28* (2), 022305/1-022305/7.

81. Tancogne-Dejean, T.; Spierings, A. B.; Mohr, D., Additively-manufactured metallic micro-lattice materials for high specific energy absorption under static and dynamic loading. *Acta Mater.* **2016,** *116*, 14-28.

82. Ambrosi, A.; Pumera, M., Self-Contained Polymer/Metal 3D Printed Electrochemical Platform for Tailored Water Splitting. *Adv. Funct. Mater.* **2017**, Ahead of Print.

83. Thijs, L.; Verhaeghe, F.; Craeghs, T.; Van Humbeeck, J.; Kruth, J.-P., A study of the microstructural evolution during selective laser melting of Ti-6Al-4V. *Acta Mater.* **2010,** *58* (9), 3303-3312.

84. Kruth, J. P.; Froyen, L.; Van Vaerenbergh, J.; Mercelis, P.; Rombouts, M.; Lauwers, B., Selective laser melting of iron-based powder. *J. Mater. Process. Technol* **2004,** *149* (1-3), 616-622.

85. Li, R.; Liu, J.; Shi, Y.; Wang, L.; Jiang, W., Balling behavior of stainless steel and nickel powder during selective laser melting process. *The International Journal of Advanced Manufacturing Technology* **2012,** *59* (9), 1025-1035.

86. Fischer, P.; Romano, V.; Weber, H. P.; Karapatis, N. P.; Boillat, E.; Glardon, R., Sintering of commercially pure titanium powder with a Nd:YAG laser source. *Acta Materialia* **2003,** *51* (6), 1651-1662.

87. Loh, L. E.; Liu, Z. H.; Zhang, D. Q.; Mapar, M.; Sing, S. L.; Chua, C. K.; Yeong, W. Y., Selective Laser Melting of aluminium alloy using a uniform beam profile. *Virtual and Physical Prototyping* **2014,** *9* (1), 11-16.

88. A.B., S.; N., H.; G., L., Influence of the particle size distribution on surface quality and mechanical properties in AM steel parts. *Rapid Prototyping Journal* **2011,** *17* (3), 195-202.

89. Yadroitsev, I.; Yadroitsava, I., Evaluation of residual stress in stainless steel 316L and Ti6Al4V samples produced by selective laser melting. *Virtual and Physical Prototyping* **2015,** *10* (2), 67-76.

90. Shiomi, M.; Osakada, K.; Nakamura, K.; Yamashita, T.; Abe, F., Residual Stress within Metallic Model Made by Selective Laser Melting Process. *CIRP Annals* **2004,** *53* (1), 195-198.

91. Yasa, E.; Deckers, J.; Kruth, J.-P.; Rombouts, M.; Luyten, J., Investigation of Sectoral Scanning in Selective Laser Melting. **2010,** (49187), 695-703.

92. Abe, F.; Santos, E. C.; Kitamura, Y.; Osakada, K.; Shiomi, M., Influence of forming conditions on the titanium model in rapid prototyping with the selective laser melting process. *Proceedings of the Institution of Mechanical Engineers, Part C: Journal of Mechanical Engineering Science* **2003,** *217* (1), 119-126.

93. Laoui, T.; Santos, E.; Osakada, K.; Shiomi, M.; Morita, M.; Shaik, S. K.; Tolochko, N. K.; Abe, F.; Takahashi, M., Properties of Titanium Dental Implant Models Made by Laser Processing. *Proceedings of the Institution of Mechanical Engineers, Part C: Journal of Mechanical Engineering Science* **2006,** *220* (6), 857-863.

94. http://www.wirebiters.com/selective-laser-melting/.

95. Guan, K.; Wang, Z.; Gao, M.; Li, X.; Zeng, X., Effects of processing parameters on tensile properties of selective laser melted 304 stainless steel. *Materials & Design* **2013,** *50*, 581-586.

96. Liu, C.; Zhang, M.; Chen, C., Effect of laser processing parameters on porosity, microstructure and mechanical properties of porous Mg-Ca alloys produced by laser additive manufacturing. *Materials Science and Engineering: A* **2017,** *703*, 359-371.

97. Kasperovich, G.; Haubrich, J.; Gussone, J.; Requena, G., Correlation between porosity and processing parameters in TiAl6V4 produced by selective laser melting. *Materials & Design* **2016,** *105*, 160-170.

98. Yongqiang, Y.; Jian□bin, L.; Zhi□Yi, L.; Di, W., Accuracy and density optimization in directly fabricating customized orthodontic production by selective laser melting. *Rapid Prototyping Journal* **2012,** *18* (6), 482-489.

99. Li, R.; Liu, J.; Shi, Y.; Du, M.; Xie, Z., 316L Stainless Steel with Gradient Porosity Fabricated by Selective Laser Melting. *Journal of Materials Engineering and Performance* **2010,** *19* (5), 666-671.

100. Yadroitsev, I.; Bertrand, P.; Laget, B.; Smurov, I., Application of laser assisted technologies for fabrication of functionally graded coatings and objects for the International Thermonuclear Experimental Reactor components. *Journal of Nuclear Materials* **2007,** *362* (2), 189-196.

101. Smith, M.; Cantwell, W. J.; Guan, Z.; Tsopanos, S.; Theobald, M. D.; Nurick, G. N.; Langdon, G. S., The quasi-static and blast response of steel lattice structures. *Journal of Sandwich Structures & Materials* **2010,** *13* (4), 479-501.

102. Ushijima, K.; Cantwell, W. J.; Mines, R. A. W.; Tsopanos, S.; Smith, M., An investigation into the compressive properties of stainless steel micro-lattice structures. *Journal of Sandwich Structures & Materials* **2010,** *13* (3), 303-329.

103. Nofal, M.; Pan, Y.; Al-Hallaj, S., Selective Laser Sintering of Phase Change Materials for Thermal Energy Storage Applications. *Procedia Manufacturing* **2017,** *10* (Supplement C), 851-865.

104. Chen, Y.-T.; Hung, F.-Y.; Lui, T.-S.; Hong, J.-Z., Microstructures and Charge-Discharging Properties of Selective Laser Sintering Applied to the Anode of Magnesium Matrix. *MATERIALS TRANSACTIONS* **2017,** *58* (4), 525-529.

105. Ming, L.; Yang, H.; Zhang, W.; Zeng, X.; Xiong, D.; Xu, Z.; Wang, H.; Chen, W.; Xu, X.; Wang, M.; Duan, J.; Cheng, Y.-B.; Zhang, J.; Bao, Q.; Wei, Z.; Yang, S., Selective laser sintering of TiO2 nanoparticle film on plastic conductive substrate for highly efficient flexible dye-sensitized solar cell application. *Journal of Materials Chemistry A* **2014,** *2* (13), 4566-4573.

106. Ambrosi, A.; Pumera, M., Self-Contained Polymer/Metal 3D Printed Electrochemical Platform for Tailored Water Splitting. *Advanced Functional Materials*, 1700655-n/a.

107. Ohara, S.; Suzuki, J.; Sekine, K.; Takamura, T., A thin film silicon anode for Li-ion batteries having a very large specific capacity and long cycle life. *Journal of Power Sources* **2004,** *136* (2), 303-306.

108. Hu, R.; Liu, H.; Zeng, M.; Liu, J.; Zhu, M., Progress on Sn-based thin-film anode materials for lithium-ion batteries. *Chinese Science Bulletin* **2012,** *57* (32), 4119-4130.

109. Yang, C.; Zhang, C.; Xing, W.; Liu, L., 3D printing of Zr-based bulk metallic glasses with complex geometries and enhanced catalytic properties. *Intermetallics* **2018,** *94*, 22-28.

110. Lu, Z. P.; Liu, C. T., Role of minor alloying additions in formation of bulk metallic glasses: A Review. *Journal of Materials Science* **2004,** *39* (12), 3965-3974.

111. Greer, A. L., Metallic glasses…on the threshold. *Materials Today* **2009,** *12* (1), 14-22.

112. Johnson, W. L., Bulk Glass-Forming Metallic Alloys: Science and Technology. *MRS Bulletin* **2013,** *24* (10), 42-56.

113. Liu, Y. H.; Wang, G.; Wang, R. J.; Zhao, D. Q.; Pan, M. X.; Wang, W. H., Super

Plastic Bulk Metallic Glasses at Room Temperature. *Science* **2007,** *315* (5817), 1385-1388.

114. Kumar, G.; Tang, H. X.; Schroers, J., Nanomoulding with amorphous metals. *Nature* **2009,** *457*, 868.

115. Schroers, J., Processing of Bulk Metallic Glass. *Advanced Materials* **2010,** *22* (14), 1566-1597.

116. Ambrosi, A.; Pumera, M., 3D-printing technologies for electrochemical applications. *Chemical Society Reviews* **2016,** *45* (10), 2740-2755.

117. Inoue, A.; Takeuchi, A., Recent development and application products of bulk glassy alloys. *Acta Materialia* **2011,** *59* (6), 2243-2267.

118. Thijs, L.; Verhaeghe, F.; Craeghs, T.; Humbeeck, J. V.; Kruth, J.-P., A study of the microstructural evolution during selective laser melting of Ti–6Al–4V. *Acta Materialia* **2010,** *58* (9), 3303-3312.

119. Tan, X.; Cui, H., Comparative studies on biological activity of generic and branded enoxaparin in vivo and vitro. *Blood Coagul Fibrinolysis* **2015,** *26* (7), 805-10.

120. Seifi, M.; Salem, A.; Beuth, J.; Harrysson, O.; Lewandowski, J. J., Overview of Materials Qualification Needs for Metal Additive Manufacturing. *JOM* **2016,** *68* (3), 747-764.

121. Everton, S. K.; Hirsch, M.; Stravroulakis, P.; Leach, R. K.; Clare, A. T., Review of in-situ process monitoring and in-situ metrology for metal additive manufacturing. *Materials & Design* **2016,** *95*, 431-445.

122. Lewandowski, J. J.; Seifi, M., Metal Additive Manufacturing: A Review of Mechanical Properties. *Annual Review of Materials Research* **2016,** *46* (1), 151-186.

123. Körner, C.; Helmer, H.; Bauereiß, A.; Singer, R. F., Tailoring the grain structure of IN718 during selective electron beam melting. *MATEC Web of Conferences* **2014,** *14*, 08001.

124. Hagihara, K.; Nakano, T.; Suzuki, M.; Ishimoto, T.; Suyalatu; Sun, S.-H., Successful additive manufacturing of MoSi2 including crystallographic texture and shape control. *Journal of Alloys and Compounds* **2017,** *696*, 67-72.

125. Amine, T.; Newkirk, J. W.; Liou, F., Methodology for Studying Effect of Cooling Rate During Laser Deposition on Microstructure. *Journal of Materials Engineering and Performance* **2015,** *24* (8), 3129-3136.

126. Wang, P.; Nai, M. L. S.; Tan, X.; Vastola, G.; Raghavan, S.; Sin, W. J.; Tor, S.; Pei, Q.-X.; Wei, J., *Recent Progress of Additive Manufactured Ti-6Al-4V by Electron Beam Melting*. 2016.

127. Song, B.; Dong, S.; Liu, Q.; Liao, H.; Coddet, C., Vacuum heat treatment of iron parts produced by selective laser melting: Microstructure, residual stress and tensile behavior. *Materials & Design (1980-2015)* **2014,** *54*, 727-733.

128. Bernhard, M., Additive Manufacturing Technologies – Rapid Prototyping to Direct Digital Manufacturing. *Assembly Automation* **2012,** *32* (2), null.

129. Wang, X.; Chou, K., *Residual stress in metal parts produced by powder-bed additive manufacturing processes*. 2015.

3 LASER PROCESSED Ni-Fe ALLOY AS ELECTROCATALYST TOWARD OXYGEN EVOLUTION REACTION

3.1 Overview

Nowadays, the energy supply strongly depends on the combustion of fossil fuels, such as coal, petroleum and natural gas. However, the diminishing supply and pollution products from fossil fuels cause a heavy economic and environmental pressure. Therefore the exploration of renewable and clean energy sources becomes even more urgent.[1-4] However, due to the sluggish reaction kinetics of oxygen evolution reaction (OER), electrocatalyst with excellent electrocatalytic activity toward OER is of high demand[5-7].

Herein, in this chapter, a one-step laser-based manufacturing method is applied to prepare a thin layer of NiFe alloys with varied Ni and Fe ratios as the electrocatalyst toward OER for the first time. Their structures, morphologies and compositions are examined by XRD, XPS and SEM prior and after electrochemical testing. Remarkably, the laser processed Ni_6Fe_4 alloy exhibit an excellent activity with an OER current density of 100 mA/cm^2 at 464 mV overpotential in 1 M KOH aqueous solution, which is among the best-performance OER electrocatalyst reported so far, and maintains the electrochemical performance for at least 18 hours. The application of laser-based manufacturing for electrocatalyst synthesis allows great facility for both electrode design and composition optimization, which may pave a new way for the efficient and effective development of novel electrocatalyst.

3.2 Experimental

3.2.1 Fabrication of NiFe alloys

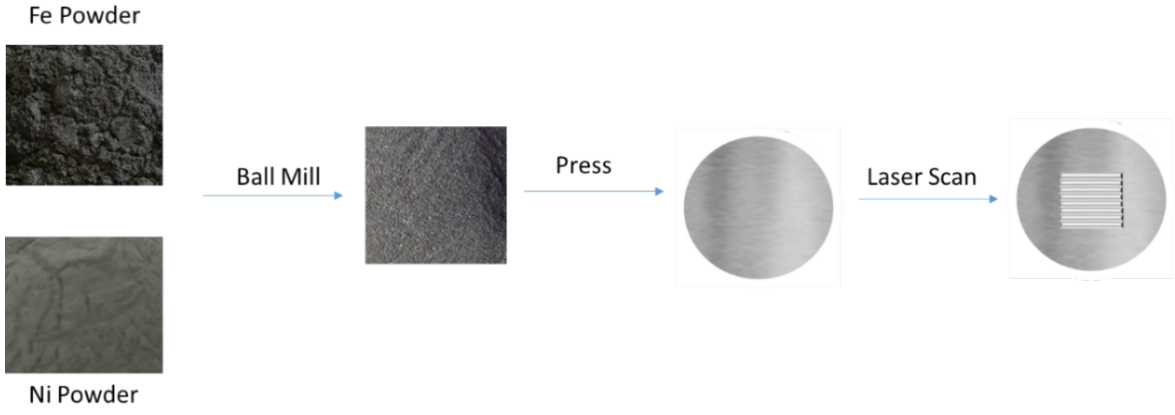

Figure 3.1 Illustration of fabrication process

To fabricate the Ni-Fe alloys by laser-based manufacturing, 0.8 g of commercial nickel (3-7 micron, Alfa Aesar, >99.9%, metals basis) and iron (power (fine), Sigma Aldrich, >99%, metals basis) powders in total, with nickel to iron atomic ratios = 10:0, 8:2, 6:4 and 4:6, were well mixed inside a polystyrene ball mill jar before melting. Then the powders were pressed in a dry pressing die with a diameter of 12.7 mm. The as-prepared die was placed into the chamber of a customer-developed laser-based manufacturing system with an ytterbium fiber laser (model: VLR-200-AC-Y11) and a ProSeries II scan head. The laser beam scanned the surface of the dies at a power of 77 W with a spot size of 50 μm at a scan speed of 200 mm/s and a hatch spacing of 0.254 mm with the chamber protected by argon gas. A square specimen with a dimension of 7 mm × 7 mm was fabricated in the center of the disk shaped sample. The resulted alloys were labeled as Ni, Ni_8Fe_2, Ni_6Fe_4 and Ni_4Fe_6, respectively.

3.2.2 Materials Characterizations

The Ni-Fe binary phase diagram is modeled by ThermoCalc™ software. The crystal structures of the as-fabricated and after used (electrochemical testing) Ni-Fe alloy samples were characterized by an X-ray diffraction (XRD) using a Panalytical Empyrean multipurpose diffractometer equipped with PreFIX modules with Cu Kα radiation. The morphologies of the fresh and used Ni-Fe alloy samples were studied using an FEI Quanta 3D FEG scanning electron microscope (SEM) equipped with energy-dispersive X-ray spectroscopy (EDXS) at an acceleration voltage of 20 kV. The chemical states of elements in the fresh and used samples were characterized by the Kratos AXIS 165 X-ray photoelectron spectroscopy (XPS) with the charge neutralization function on.

3.2.3 Electrochemical measurements

The electrochemical measurements were carried out in a three-electrode system using a CHI 650C electrochemical workstation. The as prepared NiFe alloys served as the working electrode in a 1 M KOH aqueous electrolyte, with Pt wire and saturated calomel (SCE) as counter electrode and reference electrode, respectively. Linear sweep voltammetry (LSV) was carried out in the potential range of 0 - 1V vs SCE at a scan rate of 2 mV/s. Electrochemical impedance spectra (EIS) measurements were carried out at an overpotential of 400 mV with an applied voltage aptitude of 5 mV in the frequency range from 10^5 Hz to 0.1 Hz. To study the stability of the NiFe alloy as the electrocatalyst for oxygen evolution reaction, the chronoamperometry was carried out at 438 mV overpotential for 18 hrs.

3.3 Results and Discussion

3.3.1 Fe-Ni Phase Diagram

As shown in the Fe-Ni phase diagram, the Fe-Ni system has five equilibrium phases: the liquid phase, L; the BCC δ-Fe solid solution phase, the FCC, γ-Fe,Ni solid solution; the

BCC α-Fe solid solution phase and the $FeNi_3$ phase. The melting point of Fe is at 1538℃, the melting point of Ni is at 1455℃, and the lowest point of the liquidus line is located at ~1440℃. The separation between the liquidus and solidus line are only about 5℃ to 10℃.

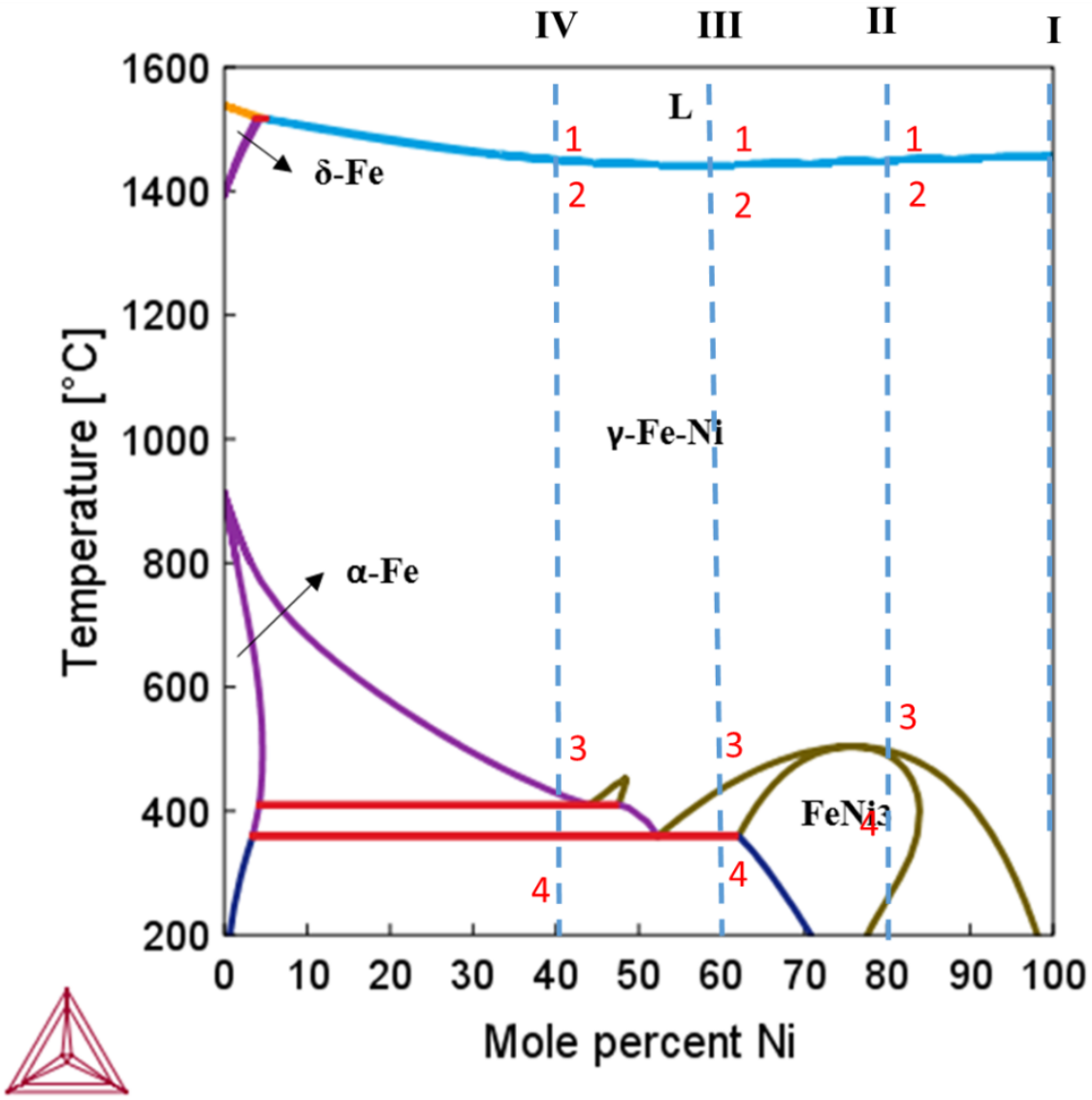

Figure 3.2 Phase diagram of binary Fe-Ni system

Under equilibrium conditions, see Fig.3.2

(I) Pure Ni solidified from melting point, γ-Ni is precipitated.

$$L \rightarrow \gamma\text{-Ni}$$

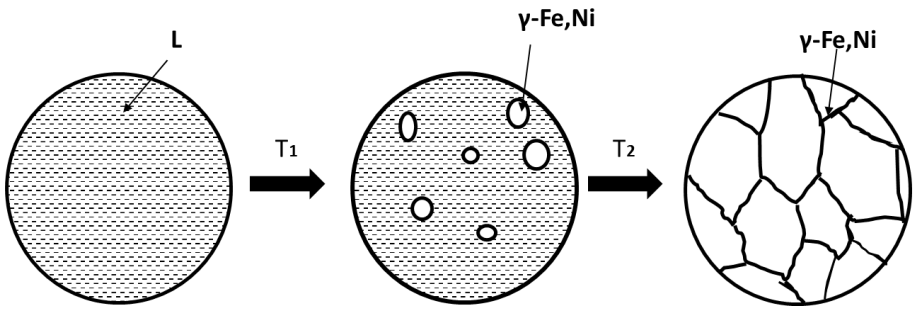

Figure 3.3 Phase transition of Ni_8Fe_2 under equilibrium conditions

(II) Ni_8Fe_2 (80% Ni - 20% Fe) solidified from above liquidus line,

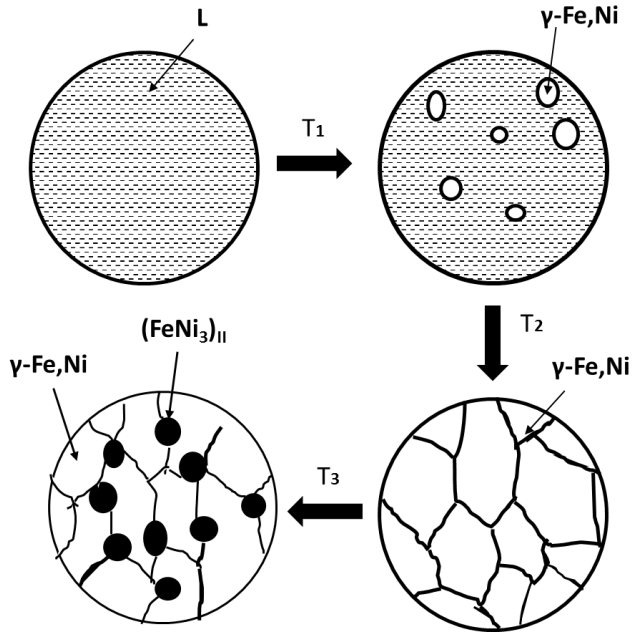

Figure 3.4 Phase transition of Ni_8Fe_2 under equilibrium conditions

When temperature reaches point 1, the isomorphous reaction of γ-Fe,Ni phase precipitation starts.

$$L \rightarrow \gamma\text{-Fe,Ni} + L$$

With the decreasing temperature, the γ-Fe,Ni phase keeps increasing with liquid phase decreasing. This process ends at point 2.

$$L + \gamma\text{-Fe,Ni} \rightarrow \gamma\text{-Fe,Ni}$$

In the temperature range of 2 to 3, γ-Fe,Ni phase is single phase system.

When the temperature decreases to point 3, the $FeNi_3$ starts to precipitate from the supersaturated γ-Fe,Ni phase to form $(FeNi_3)_{II}$ secondary crystals. This process ends at point 4.

$$\gamma\text{-Fe,Ni} \rightarrow (FeNi_3)_{II} + \gamma\text{-Fe,Ni}$$

Therefore, under equilibrium condition, the Ni_8Fe_2 sample is constituted by γ-Fe,Ni primary crystals and small $(FeNi_3)_{II}$ secondary crystals.

(III) Ni_4Fe_6 (60% Ni - 40% Fe) solidified from liquidus line, γ-Fe,Ni phase is single phase system until reaching temperature 3. At point 3, α-Fe starts to crystalize from the supersaturated γ-Fe,Ni phase to form secondary $(FeNi_3)_{II}$ crystals precipitate from the γ-Fe,Ni phase. This process ends at point 4.

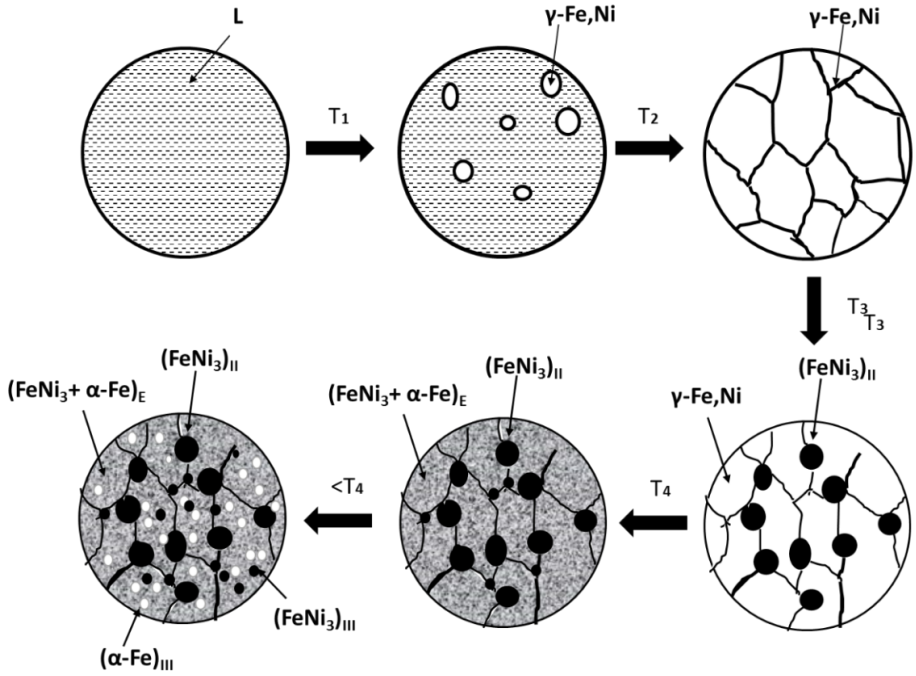

Figure 3.5 Phase transition of Ni_6Fe_4 under equilibrium conditions

$$\gamma\text{-Fe,Ni} \rightarrow (FeNi_3)_{II} + \gamma\text{-Fe,Ni}$$

When temperature reaches point 4 (the eutectic point), the γ-Fe,Ni starts to transit to the eutectic phase of $(FeNi_3)_{II}$ phase and $(FeNi_3 + \alpha\text{-Fe})_E$ eutectic phase

$$\gamma\text{-Fe,Ni} \rightarrow (FeNi_3)_{II} + (FeNi_3 + \alpha\text{-Fe})_E$$

When temperature decreasing below, $(\alpha\text{-Fe})_{III}$ phase starts to precipitate from $(FeNi_3)_{II}$ phase and $(FeNi_3 + \alpha\text{-Fe})_E$ eutectic phase,

$$(FeNi_3 + \alpha\text{-Fe})_E \rightarrow (FeNi_3)_{III} + (\alpha\text{-Fe})_{III}$$
$$(FeNi_3)_{II} \rightarrow (FeNi_3)_{II} + (\alpha\text{-Fe})_{III}$$

Therefore, under equilibrium condition, the Ni_6Fe_4 sample is constituted by $\gamma\text{-}(FeNi_3 + \alpha\text{-Fe})_E$ eutectic crystal, $(FeNi_3)_{II}$ secondary crystals and $(FeNi_3)_{III}$ and $(\alpha\text{-Fe})_{III}$ tertiary crystals.

(IV) Ni_6Fe_4 (40% Ni - 60% Fe) is solidified from liquidus line, γ-Fe,Ni phase is single phase system until reach temperature 3. At point 3, α-Fe starts to precipitate from the supersaturated γ-Fe,Ni phase to form secondary $(\alpha\text{-Fe})_{II}$ crystals among the γ-Fe,Ni phase. This process ends at point 4.

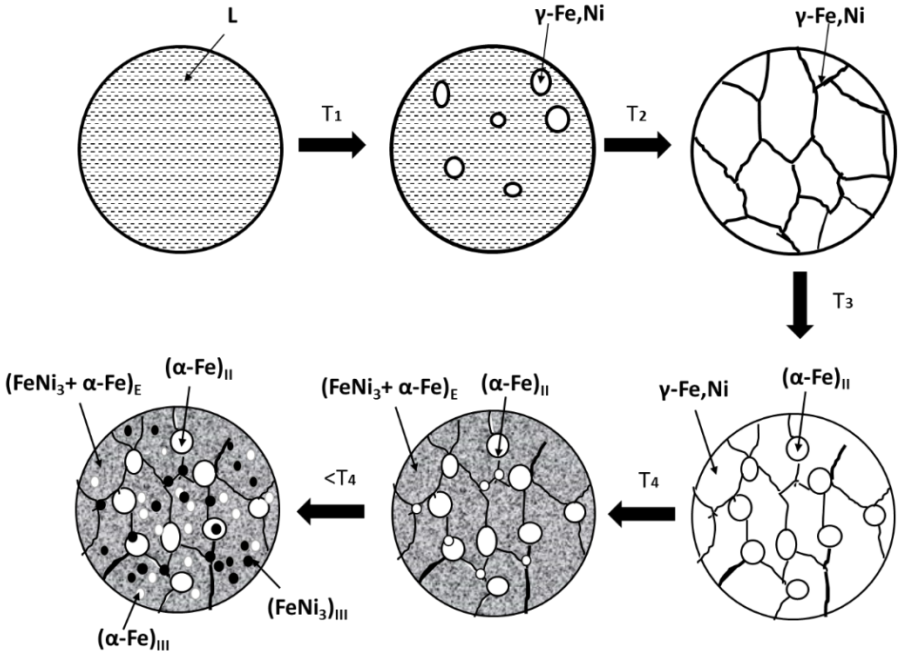

Figure 3.6 Phase transition of Ni_4Fe_6 under equilibrium conditions

$$\gamma\text{-Fe,Ni} \rightarrow (\alpha\text{-Fe})_{II} + \gamma\text{-Fe,Ni}$$

When temperature reaches point 4 (the eutectic point), the γ-Fe,Ni starts to transit to the eutectic phase of α-Fe phase and $(FeNi_3 + \alpha\text{-Fe})_E$ eutectic phase

$$\gamma\text{-Fe,Ni} \rightarrow (\alpha\text{-Fe})_{II} + (FeNi_3 + \alpha\text{-Fe})_E$$

When temperature decreasing below, $(FeNi_3)_{III}$ tertiary phase starts to precipitate from $(\alpha\text{-}Fe)_{II}$ secondary phase and $(FeNi_3 + \alpha\text{-}Fe)_E$ eutectic phase,

$$(FeNi_3 + \alpha\text{-}Fe)_E \rightarrow (\alpha\text{-}Fe)_{III} + (FeNi_3)_{III}$$

$$(\alpha\text{-}Fe)_{II} \rightarrow (\alpha\text{-}Fe)_{II} + (FeNi_3)_{III}$$

Therefore, under equilibrium condition, the Ni_4Fe_6 sample is constituted by $\gamma\text{-}(FeNi_3 + \alpha\text{-}Fe)_E$ eutectic crystals, $(\alpha\text{-}Fe)_{II}$ secondary crystals and $(\alpha\text{-}Fe)_{III}$ and $(FeNi_3)_{III}$ tertiary crystals.

3.3.2 Crystal Structure Analysis by XRD

The Ni-Fe binary phase diagram is presented in Fig 3-2, predicted using ThermoCalc package. To determine the crystal structure of Ni-Fe alloys prepared by laser-based manufacturing, the XRD patterns of Ni, Ni_8Fe_2, Ni_6Fe_4, and Ni_4Fe_6 are presented in Fig. 3-7. Peaks at $2\theta = 44.605°$, $51.979°$ and $76.591°$ are observed in the pure Ni sample, which are corresponding to planes of (111), (200) and (220) of γ-Ni (JCPDF card no. 01-070-0989) with lattice parameters of a = 3.5157 Å. For Ni_8Fe_2 sample, it consists of a primary γ phase, and a new phase with diffraction peaks at $2\theta = 44.121°$, $51.404°$ and $75.661°$, corresponding to planes of (111), (200) and (220) of cubic $FeNi_3$ alloy (JCPDF card no. 03-065-3244) with a = 3.5523 Å. By increasing the content of Fe to 40%, the relative peaks intensity of $FeNi_3$ phases is apparently enhanced, indicating the concentration of $FeNi_3$ phase in is Ni_6Fe_4 strongly increased compared to Ni_8Fe_2 sample. Ni_6Fe_4 also has a secondary eutectic phase with $2\theta = 43.173°$, $50.674°$ and $74.679°$ corresponding to (111), (200) and (220) plane of cubic taenite FeNi (JCPDF card no. 00-003-0016) with a = 3.6010 Å. In addition, minor peaks from BCC structured α-Fe is observed in the Ni_4Fe_6 sample (JCPDF card no. 00-001-1252) with $2\theta = 44.142°$ and $65.186°$ corresponding to planes of (111) and (220) with a = 2.8600 Å. The XRD spectra are in line with the simulated Ni-Fe binary phase diagram and other experimentally determined phase diagrams.[8-9] For the Ni_4Fe_6 sample, the relative peak intensity of $FeNi_3$ phase is decreased compared to Ni_6Fe_4 sample, indicating the decreased concentration of $FeNi_3$ phase. It is observed, among the tested four samples, the peak intensity of Ni sample is highest. This is due to the consisting of pure primary γ-Ni phase of relative larger grains. The peak intensities of Ni_8Fe_2 sample is getting lower, due to the precipitation of secondary $FeNi_3$ phase from the primary γ phase. The peak intensities of Ni_6Fe_4 and Ni_4Fe_6 spectra are even lower, which is due to the existence of small and ultra-small secondary grains from the rapid solidification of manufacturing process. These small grains may enable more active sites on the crystal surface that would improve the electrocatalytic activity to some degree.[10]

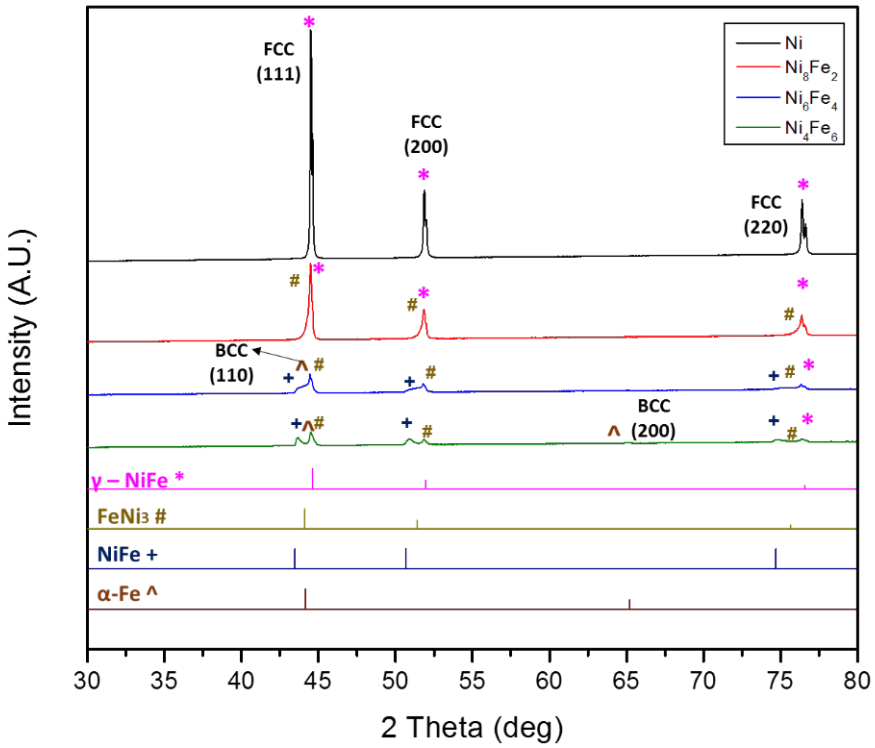

Figure 3.7 XRD spectra of Ni, Ni_8Fe_2, Ni_6Fe_4 and Ni_4Fe_6

In addition, according to the phase diagram, ultra-small grains from secondary phases would form in the Ni_6Fe_4 and Ni_4Fe_6 samples under rapid AM solidification. The minimized grain size is also confirmed by the significantly decreased peak density in the XRD spectra. Therefore, they can effectively increase the ratio of active sites on the crystal surface that improve the electrocatalytic activity to some degree. Moreover, the bond length of Ni-O is 0.208 nm[11]; The O-O single bond is 0.148 nm; The O atom centered tetrahedral shape is bent with an Ni-O-H angle of 104.5°. Therefore, the optimal lattice spacing of the catalyst is ~ 0.252 nm. With the increase of Fe content the lattice spacing of the most densely pack plane {111} is increased from to 0.247nm (γ-Fe,Ni) to 0.257 nm (NiFe), effectively increased the average lattice spacing of the FCC phases, getting close to that of optimal lattice spacing, which can effectively enhance the process of $O_{ads} + O_{ads} \rightarrow O_2$ and O_2 desorption, that expect to increase the overall catalytic activity. However, compared to Ni_6Fe_4, the significant increase of the formation of BCC α-Fe phase (most closed packed plane [12] lattice spacing = 0.248 nm) in Ni_4Fe_6 may hinder the catalytic activity, that in turn causing a decreased overall electrocatalytic activity.

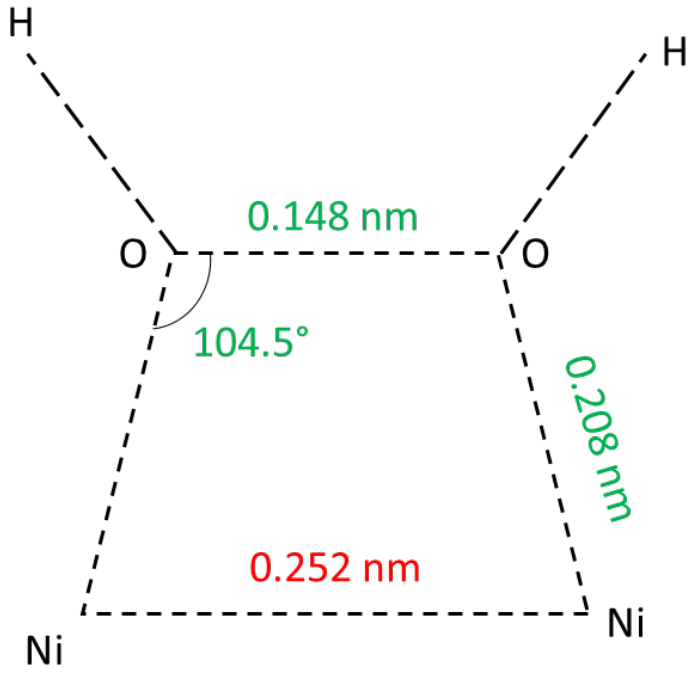

Figure 3.8 Illustration of bond lengths in Ni catalyzed OER reaction

Table 3.1 Lattice Parameters

	Crystal Structure	Most Densely Packed Plane	Lattice Spacing (nm)
γ -Ni	FCC	{111}	0.247
$FeNi_3$	FCC	{111}	0.251
NiFe	FCC	{111}	0.257
α-Fe	BCC	{110}	0.254
Optimal Structure	FCC	N/A	0.252

3.3.3 Electron Configurations

On the aspect of electron configuration, noble metals have advantageous properties to catalyze many reactions compared to transition metals. Firstly, noble metal usually has empty d orbitals, which can facilitate the s, p, d hybridization and receive a high d band occupancy. For example, the d character factor of Ru, Os, Pt and Ir are 50%, 49%, 44% and 49% respectively, much higher than that of Fe (39.5%), Co (39.7%), Ni (40%) and Ti (27%). Since the activity of a catalyst is positively relative to d%, the activity of noble metal is superior. Secondly, the work function of noble metals is relatively higher than that of transition metals. For example the work functions of Ru, Os, Pt and Ir are 4.71 eV, 5.93

eV, 5.32 eV and 5.67 eV; the work functions of Fe, Co, Ni and Ti are 4.48 eV, 4.41 eV, 4.51 eV and 4.33 eV. A larger work function has a higher potential to accept electrons that can more effectively catalyze donor reactions such as oxygen evolution reaction.

Among all first row transition metals, Ni has the most promising property toward oxygen evolution reaction, since the d%, work function and crystal structure of Ni are all most close to noble metals. In addition, the location of Ni is most close to the top of the volcano plot. To further improve the performance of Ni electrocatalyst, designing Ni-Fe alloy is one of the most effective way. During the oxygen evolution reactions, two electrons are transferred from each oxygen atom to the electrocatalyst. The activity of the catalyst is in a positive relationship to the matching-degree of reactant coordinate and catalyst d-band vacancy. Each Ni has 0.6 d-vacancy; each Fe atom has 2.2 d-vacancies. The alloying of Ni-Fe will allow electrons shift from Ni to Fe, causing the increase of d-vacancy of Ni, resulting in a catalyst matching better to the reaction electron transfer coordination. On the second hand, due to the similar work function of Fe and Ni, the Fermi level of Ni would not be affected. As a result, on the electronic aspect alloy of Ni and Fe can significantly upgrade of the electrocatalytic efficiency of transition metal based electrocatalyst for OER.

3.3.4 Chemical State Analysis by XPS

To study the surface elemental composition in fresh NiFe alloys by laser-based manufacturing, Fig. 3-9 presents XPS spectra of fresh Ni, Ni_8Fe_2, Ni_6Fe_4 and Ni_4Fe_6 samples. As shown in Fig. 3-9 (a), only peaks from Ni are observed in the survey spectrum of pure Ni, with trace amount of oxygen. After introduction of iron, Fe peaks appear and are getting intensified with increased Fe content. As shown in Fig. 3-9 (b), the Ni 2p core level spectrum of pure Ni can be deconvoluted into two main peaks at 870.18 eV and 852.88 eV for Ni $2p_{1/2}$ and $2p_{3/2}$, respectively. A doublet peak with a spin–orbital splitting of 17.3 eV, indicating metallic state of Ni.[13] Peaks at 872.09 eV and 854.02 eV indicate the formation of native nickel oxide layer due to exposure to air. Peaks at 874.26 eV and 858.51 eV are Ni 2p satellite peaks. By adding Fe, no position shift of Ni 2p peaks are observed, only with the intensity is decreased indication no chemical bonding forms between Ni and Fe, and Ni maintains metallic states in the alloy. Due to the binding energy overlapping of Fe 2p peaks with Ni LMM peaks, Fe 3p core level spectra are presented in Fig. 3-9 (c), that consists of two main peaks at 52.57 eV and 53.53 eV for Fe $3p_{1/2}$ and $3p_{3/2}$ respectively, indicating metallic state of Fe.[14] There are peaks at 54.54 eV indicating the native iron oxide layer due to exposure to air.[15] As displayed in Fig. 3-9 (d), the O 1s core spectra of pure Ni only has one peak at 531.50 eV corresponding to Ni-O bond for pure Ni sample.[16] For NiFe alloy, one more peak at 530.75 eV appears, indicating the formation of Fe-O bond.[15] It can also be observed, by increasing Fe ratio, the intensity of Fe-O is getting higher and Ni-O bond is getting lower, indicating the increased Fe content on the surface.

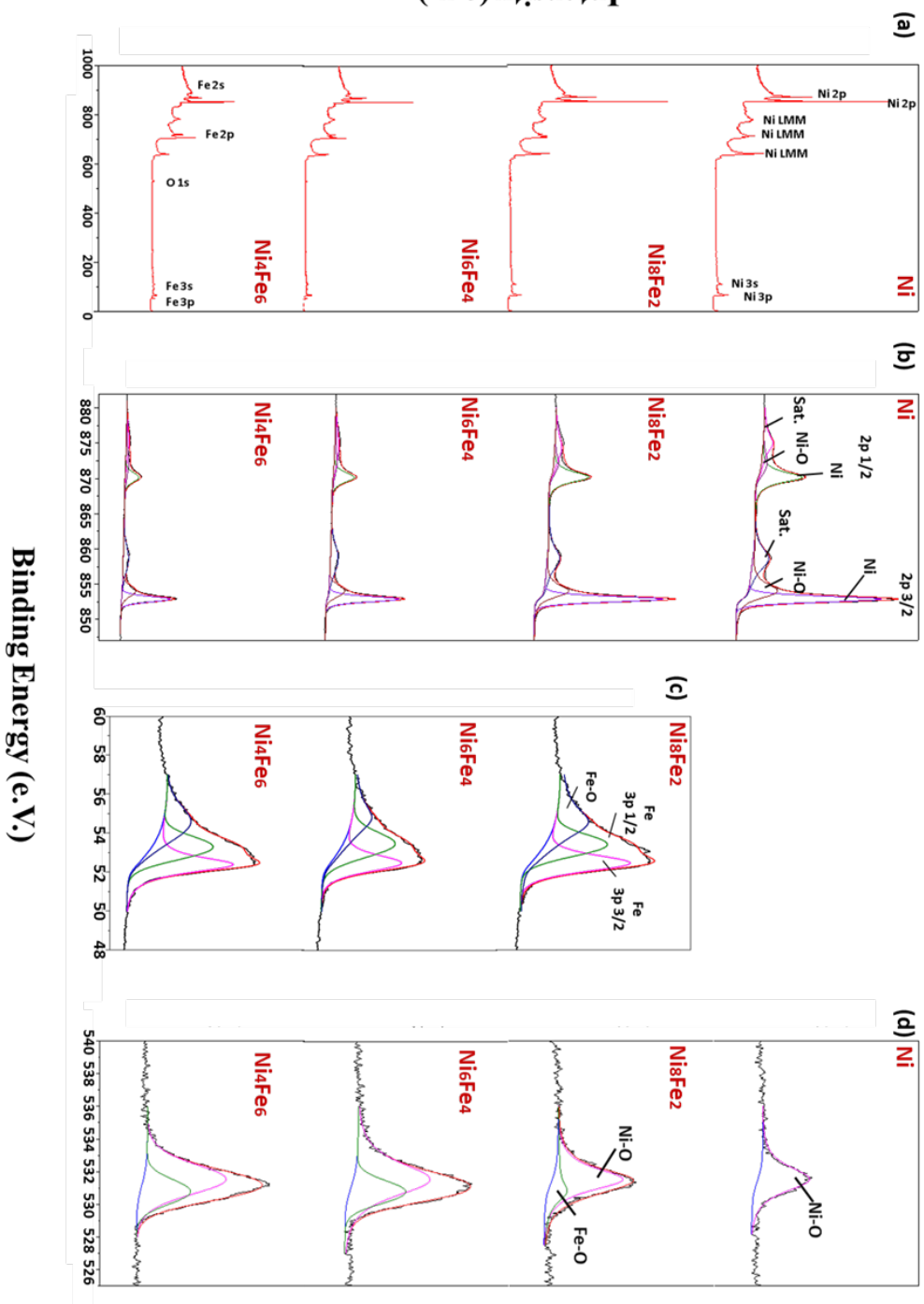

Figure 3.9 XPS spectra of (a) survey (b) Ni 2p core and Fe 3p core and O 1s core of Ni,

3.3.5 Surface Morphology Study by SEM

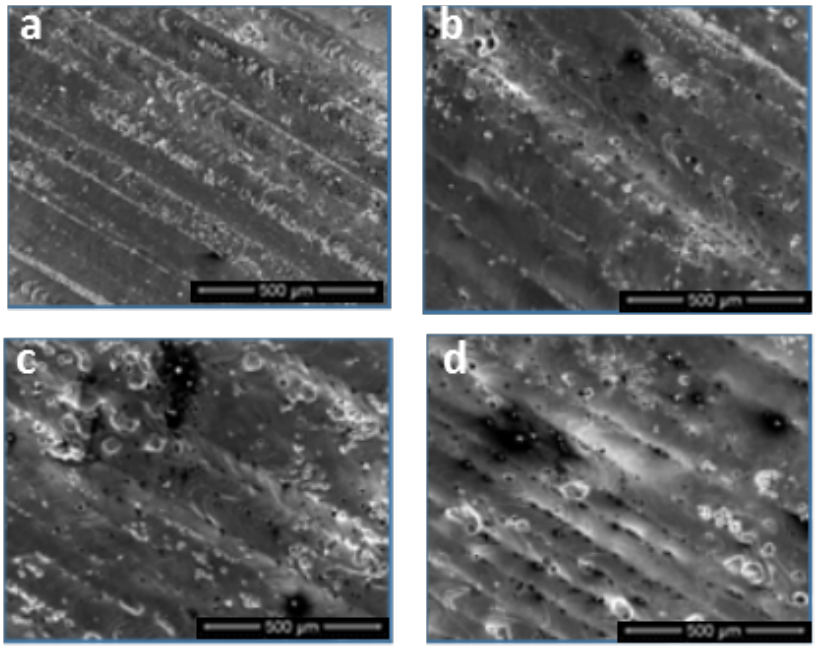

Figure 3.10 SEM images of (a) Ni, (b) Ni_8Fe_2, (c) Ni_6Fe_4 and (d) Ni_4Fe_6

The surface microstructure of the freshly processed Ni, Ni_8Fe_2, Ni_6Fe_4 and Ni_4Fe_6 samples are investigated with SEM images. As displayed in Fig. 3-10, the surfaces of the laser processed alloys are formed with parallel laser scanning tracks bonded to each other coherently. On the surface of pure Ni, the scan tracks are continuous and smooth with very small pores. However, the melting process is getting harder with increasing Fe content while keeping the same level of laser energy. The molten track surfaces become rougher. Meanwhile, the scan tracks are becoming less continuous with more balling and higher porosity with greatly enlarged pore size predominately along the edges of the molten tracks. As the Fe content is increased to 60 percent, the discontinuity of scan tracks is the most intensified with a very rough surface and large amount of pores. This is due to the fact that Ni has a relatively lower melting point (1455°C) than that of Fe (1538°C); with increased Fe content, the melting pool is less developed within the same laser dwell time. Therefore, with increased Fe content, the same laser energy density resulted in molten tracks interrupted by un-melted or sintered raw feedstock powders. However, this would not be an issue for laser-based manufacturing because an optimization process is usually conducted for different alloy compositions.

3.3.6 Elemental Distribution Study by EDXS

EDXS elemental mapping analysis was executed to characterized elemental distributions of fresh Ni_6Fe_4. Fig. 3-11 (a) displays the secondary electron (SE) image of

Ni_6Fe_4. The uniform distribution of Ni and Fe are confirmed by EDXS spectra in Fig. 3-11 (b) and (c). From the EDXS result (Fig. 3-11 (d)), the atomic percentage of Ni and Fe is 60.33% and 39.67% respectively.

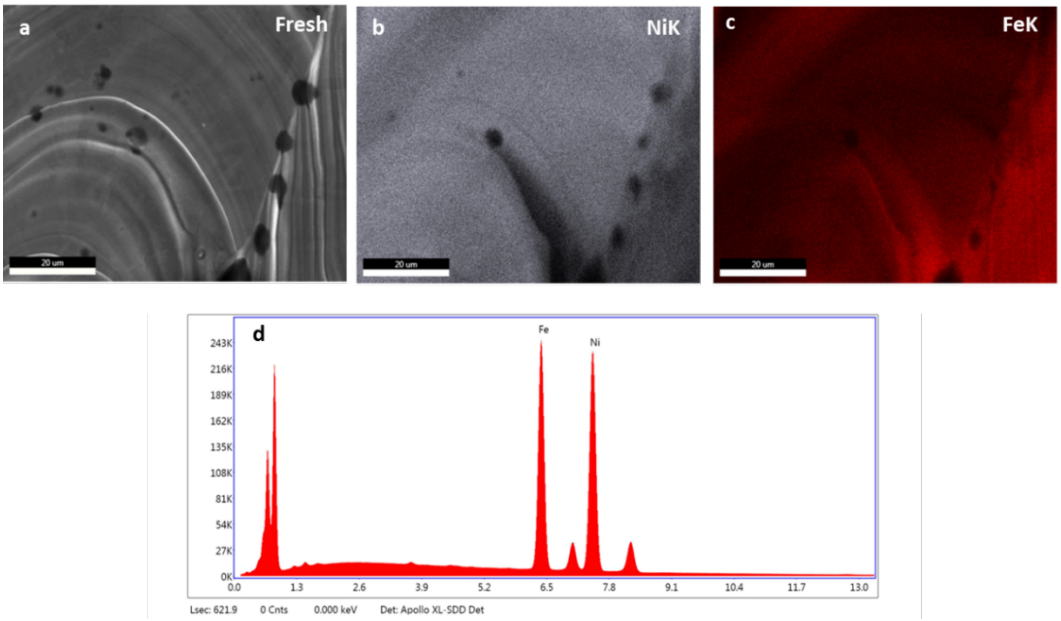

Figure 3.11 (a) (b) and(c) Energy-dispersive X-ray spectra (EDXS) elemental mappings of Ni and Fe elements in fresh Ni_6Fe_4 respectively, (d) EDXS of fresh Ni_6Fe_4

3.3.7 Catalytic Performance Study by LSV

To evaluate the catalytic performance of the laser processed Ni, Ni_8Fe_2, Ni_6Fe_4 and Ni_4Fe_6 alloys, the linear sweep voltammetry (LSV) was carried out in a 1 M KOH aqueous electrolyte using a three-electrode system. The experimental setup for LSV using an electrochemical working station with a three-electrode system to deliver a controlled potential at certain scan speed between the working electrode and reference electrode and monitor the current profile, with the studied redox reaction happening on the working electrode. At the beginning of the scan, the background current is mostly from the electron conductivity of the electrolyte. With increasing the aptitude of the potential, at the point when the applied potential reaches the onset potential of reaction, the forward direction of this redox direction would dominate, and the conversion from reactant to product will cause the staring of current rise. The flow of electrons will be further fascinated with increased potential due to increase reaction rate. The current density is the direct reflection of the electron transfer rate at the electrode/electrolyte interface. A plateau would be reached when the reaction transferred to diffusion control stage from kinetic control stage. To measure the overpotential of an electrochemistry cell, linear sweep voltammetry (LSV) is an effective technique. With the potential between working electrode and reference electrode sweeping slowly, the current is collected and peaks can be observed when redox reaction begins to happen.[17]

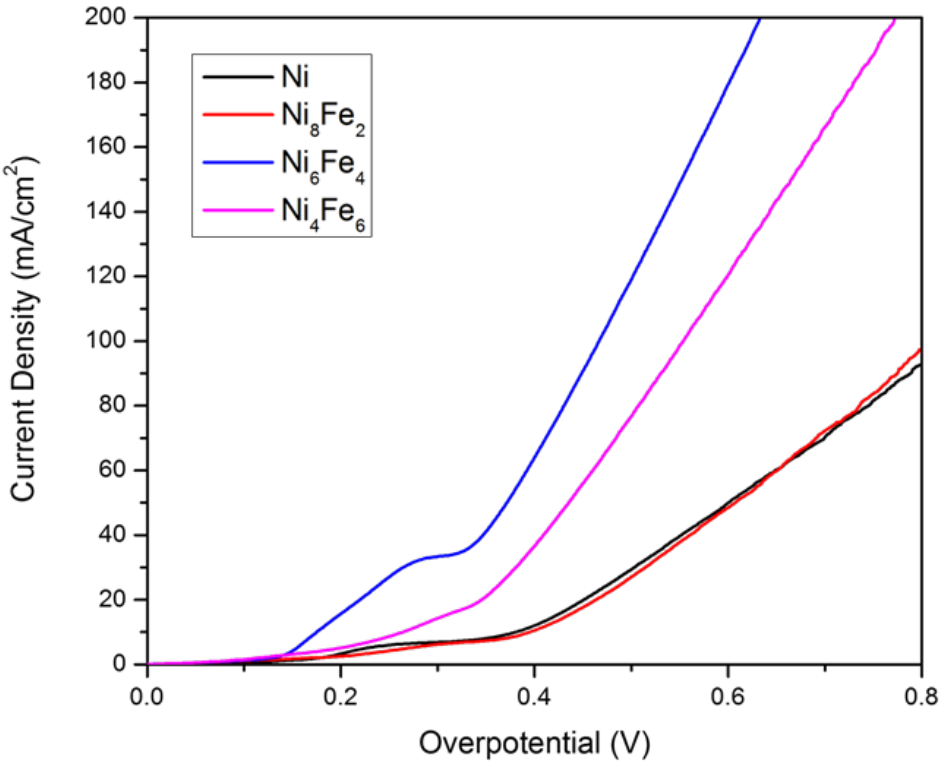

Figure 3.12 The OER polarization curves of Ni, Ni_8Fe_2, Ni_6Fe_4 and Ni_4Fe_6 electrodes

In the alkaline solution, a layer of metal hydroxides rapidly forms on the surface of the electrode.[18] It is observed in Fig. 3-13, for pure Ni electrode, $Ni(OH)_2$ is oxidized to NiOOH at an overpotential of 242 mV. With Fe introduced to the metallic system, the oxidization peak apparently shifts to higher overpotentials, which are 290 mV, 295 mV and 315 mV for Ni_8Fe_2, Ni_6Fe_4 and Ni_4Fe_6 electrode, respectively. This is due to the increased thermodynamic favorability by Fe incorporation.[19] Furthermore, the oxidization peak area is significantly enlarged for Ni_6Fe_4 electrode, suggesting an obvious increased amount of active sites on the electrode surface. [20-22] As displayed in Fig. 3-12, the pure Ni electrode exhibits a relatively low activity with an onset overpotential of 383 mV and an overpotential of 832 mV to reach an OER current density of 100 mA/cm^2. For Ni_8Fe_2, Ni_6Fe_4 and Ni_4Fe_6 working electrodes, the onset overpotentials are 386 mV, 320 mV and 340 mV, respectively, and requires overpotential of 814 mV, 464 mV and 547 mV to reach an OER current density of 100 mA/cm^2. It is observed, NiFe alloys display much higher reaction current density than pure Ni, at an overpotential of 0.5 V, the LSV current of Ni_6Fe_4 is 122 mA/cm^2, while it is only 30 mA/cm^2 for pure Ni. It is also observed, the current density is extensively correlated to Fe content in the NiFe alloys, and among which, Ni_6Fe_4 carries the highest electrochemical performance.

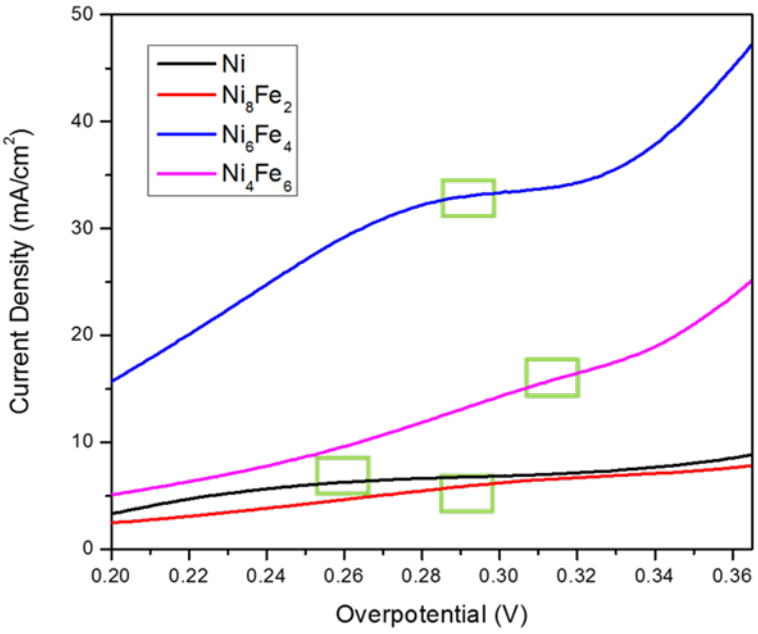

Figure 3.13 enlarged OER polarization curves Ni, Ni_8Fe_2, Ni_6Fe_4 and Ni_4Fe_6 electrodes

Table 3.2 Parameters from linear sweep voltammetry

Sample	Onset Overpotential (mV)	Overpotential for 100 mA/cm^2 OER Current Density (mV)	$Ni(OH)_2$ Oxidization Overpotential (mV)
Ni	383	832	262
Ni_8Fe_2	386	814	290
Ni_6Fe_4	320	464	295
Ni_4Fe_6	340	547	315

3.3.8 Volmer–Heyrovsky mechanism study by Tafel slope

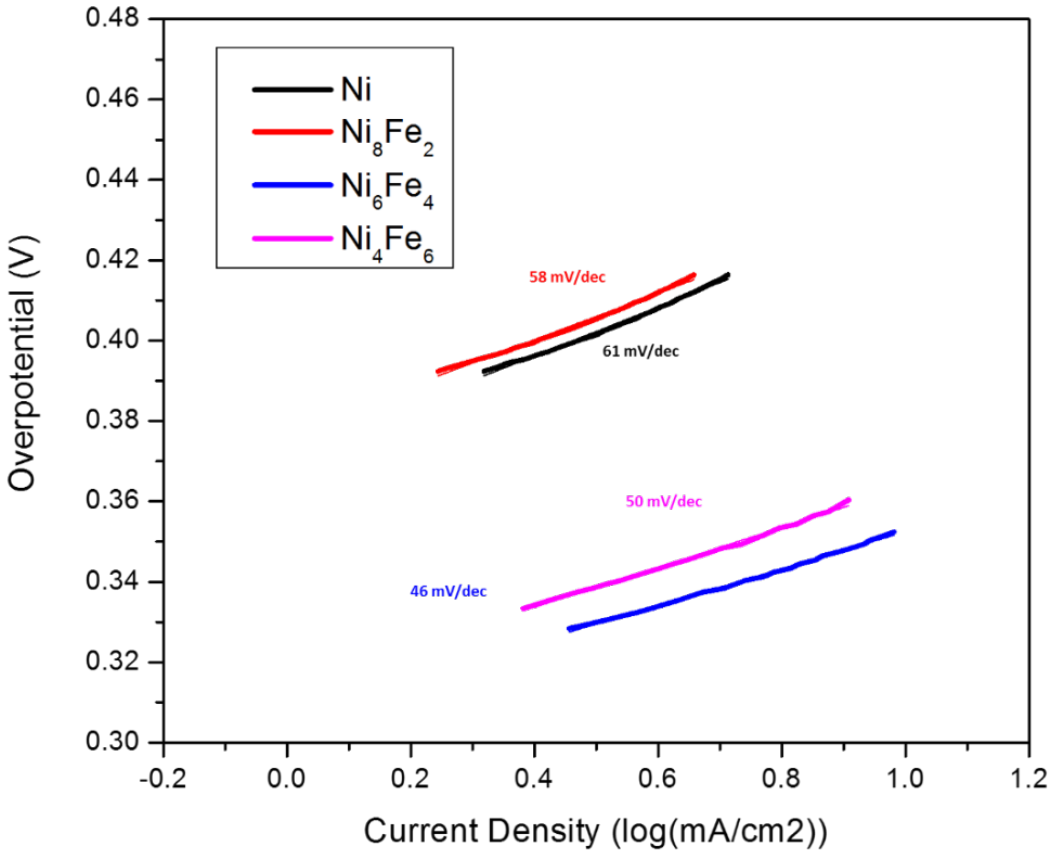

Figure 3.14 Tafel slopes of Ni, Ni_8Fe_2, Ni_6Fe_4 and Ni_4Fe_6 electrodes

The plot of overpotential η vs. log (current density) is the Tafel plot, which is used to determine the kinetic constant of electrode reactions. There is a linear region at the area close to the onset potential. Below this region, log (current density) slowing increases due to the nonnegligible background current. Once the onset potential is reached, a linear slope is well defined. In the anodic branch, the slope is $\frac{2.3\ RT}{(1-a)F}$; in the cathodic branch. The slope $-\frac{2.3RT}{aF}$, where a is the electron transfer coefficient. Therefore the kinetic of the redox reaction at the onset potential negatively correlates to the Tafel slope. To understand the electrochemical mechanism of the OER catalytic process, the linear regions of polarization curves are fitted to Tafel plots, using equation η = a + b log(j), where b is the Tafel slope.

The value of the Tafel slope for laser processed Ni, Ni_8Fe_2, Ni_6Fe_4 and Ni_4Fe_6 electrodes are 61, 58, 46 and 50 mV/decade, respectively. The Tafel slopes show that the OER process follows a Volmer–Heyrovsky mechanism, with smaller slopes indicating more rapid electron transfer at the electrode and electrolyte interface at the applied potentials.[23-24] In an OER process, the reaction activity is considerably affected by mass diffusion rate of OH^- ions and O_2 molecule through the electrode. A higher porosity of electrode surface could facilitate the mass diffusion and provide more active surface area. As a result rougher surface demonstrate higher electrocatalytic activity. On the other hand, a proper amount combination of Ni and Fe can both inhibit Fe dissolution and increase $Fe(OH)_2$/ FeOOH surface conductivity.[25] The affinity of the electrode toward O_2 and OH^- is effectively optimized. Consequently, Ni_6Fe_4 displays the highest catalytic activity of among all the electrodes. It is also observed that the alloying of Fe with Ni electrocatalyst allows electrons shift from Ni to Fe, causing the increase of d-vacancy of Ni, resulting in a catalyst matching better to the reaction electron transfer coordination. On the second hand, due to the similar work function of Fe and Ni, the Fermi lever of Ni would not be affected. As a result, on the electronic aspect alloy of Ni and Fe can significantly upgrade of the electrocatalytic efficiency of transition metal based electrocatalyst for OER. In addition, ultra-small grains from secondary and ternary phases would form in the Ni_6Fe_4 samples, which effectively increase the ratio of active sites on the crystal surface that improve the electrocatalytic activity to some degree. Moreover, with the increase of Fe content, the average lattice spacing of the most densely pack plane {111} in Ni_6Fe_4 is getting close to the optimal lattice spacing for the process of $O_{ads} + O_{ads} \rightarrow O_2$ and O_2 desorption.

Table 3.3 Tafel slope parameters

Sample	Tafel Slope (mV/dec)
Ni	63
Ni_8Fe_2	58
Ni_6Fe_4	46
Ni_4Fe_6	50

3.3.9 EIS Study by Nyquist plot

In a sinusoidal alternative current circuit, the voltage is

$$E = E_o \sin \omega t$$

Where E_o is the potential amplitude; ω is the angular frequency; and t is time. As displayed in Fig. 3-15, the AC current is not in phase with the voltage and lagged by a phase angle, ϕ, which is constant under the same frequency.

$$I = I_o \sin (\omega t + \phi)$$

In DC system $R = \frac{E}{I}$, in the AC system, impedance Z replaces resistance R. The electrochemical impedance is a very sensitive variable on the angular frequency ω.

$$Z(\omega) = \frac{E}{I} = \frac{E_o \sin \omega t}{I_o \sin (\omega t + \phi)} = \frac{E_o}{I_o} \frac{\sin \omega t}{\sin (\omega t + \phi)} = Z_o \frac{\sin \omega t}{\sin (\omega t + \phi)}$$

$$\exp (j\phi) = \cos (\phi) + j \sin (\phi)$$

$$\frac{\sin \omega t}{\sin (\omega t + \phi)} = \frac{\exp (j\omega t)}{\exp (j\omega t - \phi)} = \exp (j\phi) = \cos\phi + j \sin (\phi)$$

Therefore:

$$Z(\omega) = Z_o (\cos\phi + j \sin (\phi)) = Z_{Re} + j Z_{Im}$$

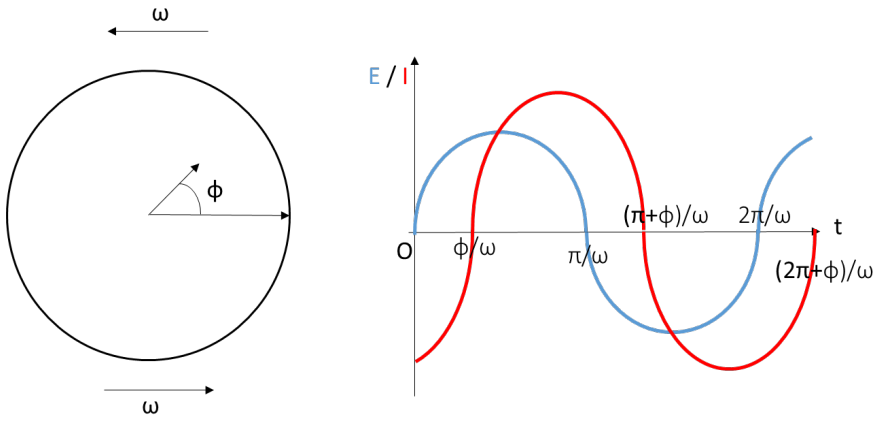

Figure 3.15 Phase diagram of current vs. voltage at angular speed of ω

The expression of electrochemical impedance of $Z(\omega)$ is composed of a real part and an imaginary part. The real part is plotted on the horizontal axis and the imaginary part is plotted on the vertical coordinate to make a Nyquist Plot, as shown in Fig. 3-16.

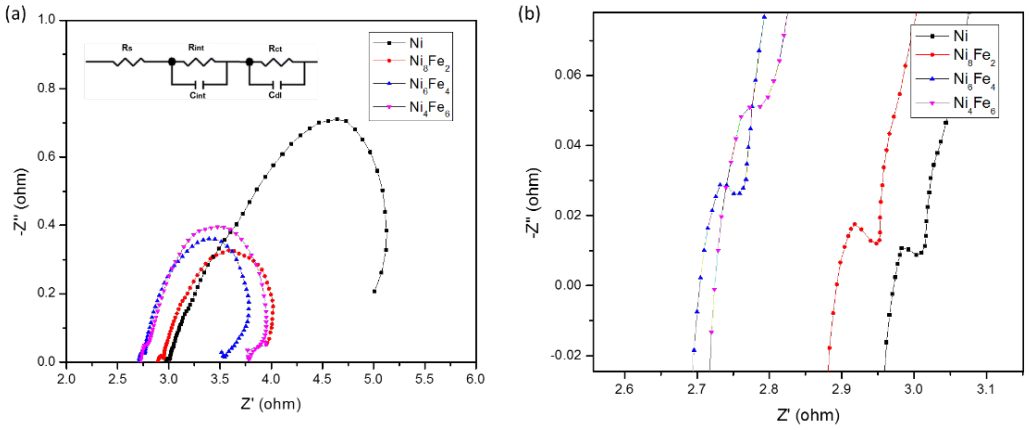

Figure 3.16 EIS spectra of Ni, Ni_8Fe_2, Ni_6Fe_4 and Ni_4Fe_6 electrodes (a) full spectra (b) enlarged area of the first semicircle

To further explore the electrochemical characteristics in the catalytic OER process on the laser processed NiFe electrodes, their Nyquist plots of EIS are taken at an overpotential of 400 mV at the frequency range of 10^5 Hz to 0.01 Hz as displayed in Fig. 3-16. The equivalent circuit is simulated by CHI 650 C electrochemical workstation, the result is listed in table 3-4.The elements in this plot include R_s - solution resistance, R_{int} – electrode/electrolyte interface resistance, R_{ct} – charge transfer resistance, C_{int} – interfacial capacity and C_{dl} – double layer capacity The intercept of the plot with the real axis at high frequency range (R_s) represents the overall ohmic resistance of the three electrode system.[2, 20] It can be observed, all electrodes have similar R_s of ~ 3 Ω. The semicircle at low frequency range could be attributed to the intermediates (MOOH, M=Ni, Fe) formation and absorption.[26] It is obvious that by increasing the amount of Fe, the size of this arc keeps increasing, indicating an apparently slower process, due to higher oxidization overpotentials for $M(OH)_2$ to MOOH. The semicircle in the high frequency range describes the charge transfer process of OH^-/O_2 redox reaction at the electrode/electrolyte interface.[26] It can be observed, the arc decreases to the smallest for the Ni_6Fe_4 electrode, illustrating its considerably improved electrocatalytic activity compared to other samples. It can be observed the effectively improved the catalytic activity of the attributed to both electron effect and structure effect. Firstly, during the oxygen evolution reactions on the cathode, two electrons are transferred from each oxygen atom to the electrocatalyst. The activity of the catalyst is in a positive relationship to the matching-degree of reactant coordinate and catalyst d-band vacancy. Each Ni has 0.6 d-vacancy; each Fe atom has 2.2 d-vacancies. The alloying of Ni and Fe allows electrons shift from Ni to Fe, causing the increase of d-vacancy of Ni, resulting in a catalyst matching better to the reaction electron transfer coordination. Secondly, the formation of ultra-small grains from secondary and ternary phases provide more grain boundaries for mass diffusion and more active sites for electrocatalytic activities. The O atom centered tetrahedral shape is bent with a Ni-O-H angle of 104.5°. Moreover, the optimized lattice spacing release the bond extra banding

and effectively fascinates the product desorption process. Therefore, overall, Ni_6Fe_4 exhibits the optimized catalytic performance.

Table 3.4 EIS parameters

Sample	R_s (Ω)	R_{int} (Ω)	R_{ct} (Ω)
Ni	2.964	0.072	2.179
Ni_8Fe_2	2.873	0.086	1.091
Ni_6Fe_4	2.696	0.056	0.928
Ni_4Fe_6	2.718	0.084	1.200

3.3.10 Stability Study by chronoamperometry

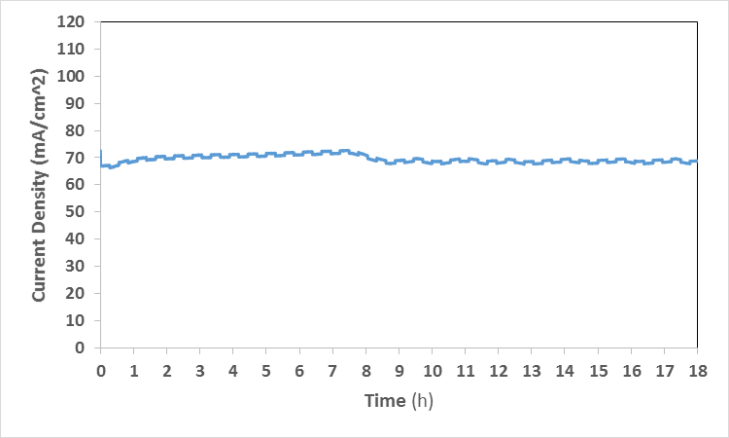

Figure 3.17 Time-dependent response during 18 hours chronoamperometric on Ni_6Fe_4 electrode at 438 mV overpotential

The stability of the laser processed Ni_6Fe_4 electrocatalyst was evaluated by chronoamperometry at a constant DC potential of 0.6 V vs SCE for 18 hrs. As shown in Fig. 3-17, the current density increases slightly in the first 0.5 hour as a result of increased

fresh surface area due to initial metal-hydroxides formation.[27] It is followed by a slight decrease after about 8 hours due to Fe dissolution and surface tension release.[28] Later on the electrode maintains a current density of ~70 mA/cm^2 without significant changes for at least 18 hours, which indicates a very high electrochemical reversibility.

3.3.11 Used Electrocatalyst Characterizations

To understand the property change of laser processed Ni_6Fe_4 electrode after being used for 18 hours as the electrode for OER, the morphology, crystallinity and chemical states of fresh and used Ni_6Fe_4 was studied by SEM, XRD and XPS. As presented in Fig.3-18, no significant morphology change can be observed after use with clear scan tracks and similar pore size. The surfaces of the used laser processed Ni_6Fe_4 alloy still maintains the parallel scan tracks bonded to each other coherently with the scan tracks are continuous and smooth.

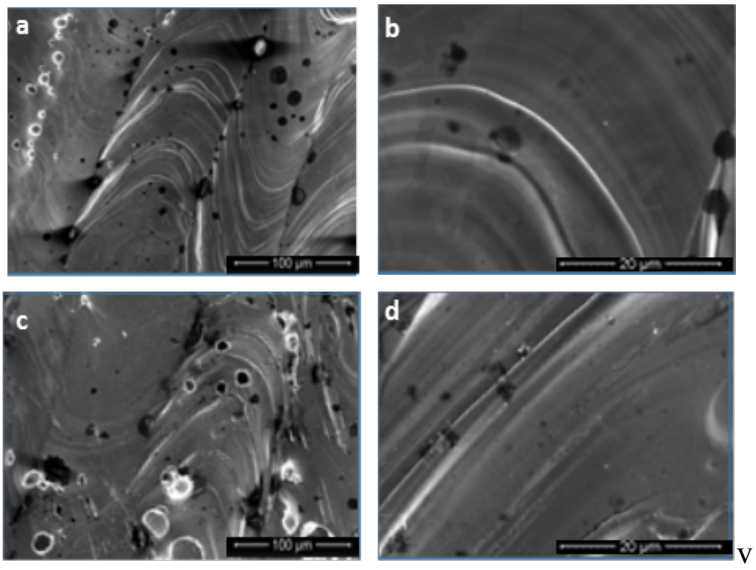

Figure 3.18 SEM images of (a) and (b) fresh Ni_6Fe_4 and (c) and (d) used Ni_6Fe_4

Meanwhile, it is observed from EDXS mapping results (Fig. 3-19), after used for 18 hours, Ni and Fe atoms are still distributed uniformly all over the surface with a certain amount of surface Fe atom dissolved into the alkaline solution, resulting in a Ni : Fe atomic ratio = 62.74% : 37.26%.

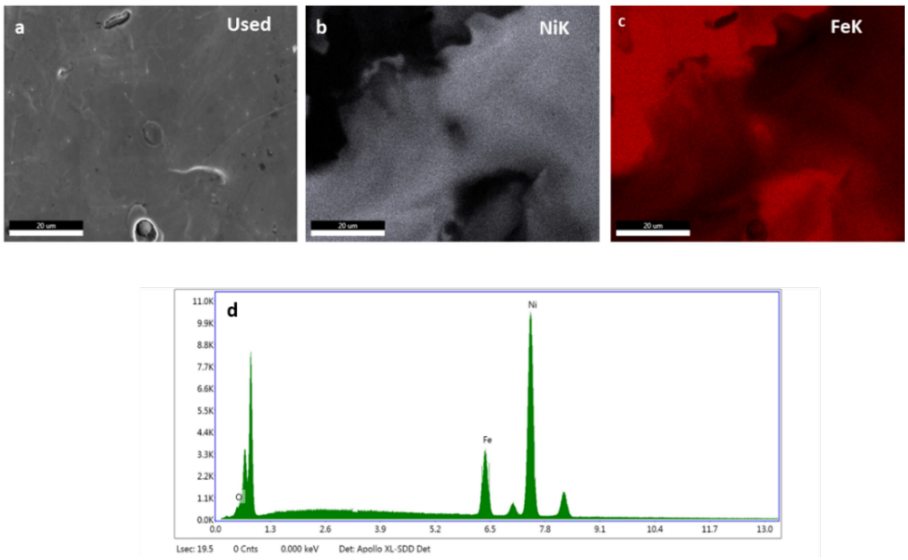

Figure 3.19 (a) (b) and(c) EDXS elemental mappings of Ni and Fe elements in used Ni_6Fe_4 respectively, (d) Energy-dispersive spectrum (EDXS) of used Ni_6Fe_4

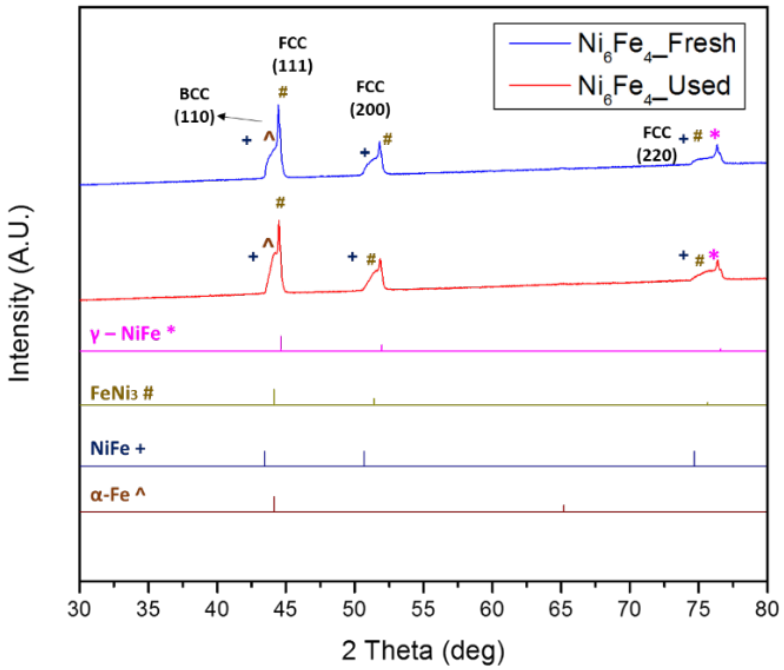

Figure 3.20 XRD spectra of fresh Ni_6Fe_4 and used Ni_6Fe_4

It is clearly observed in the XRD spectra (Fig. 3-20), the intensity of NiFe peaks and Fe peaks is apparently decreased in after-use Ni_6Fe_4 alloy, with the ratio of $FeNi_3$ peak

intensity slightly increased and Ni peaks almost unchanged, indicating NiFe is partially converted to $FeNi_3$ due to Fe dissolution.

As shown in the XPS spectra of Ni 2p core and Fe 3p core (Fig. 3-21(b) &(c)), the area ratio of Ni-O and Fe-O bond to metallic Ni and Fe are significantly increased. It can also be observed in a deconvoluted peak at higher binding energy appears in O 1s spectra (Fig. 3-21 (d)), which attributed to the formation of Ni-OH and Fe-OH bond[29-30] after being used as electrocatalysts.

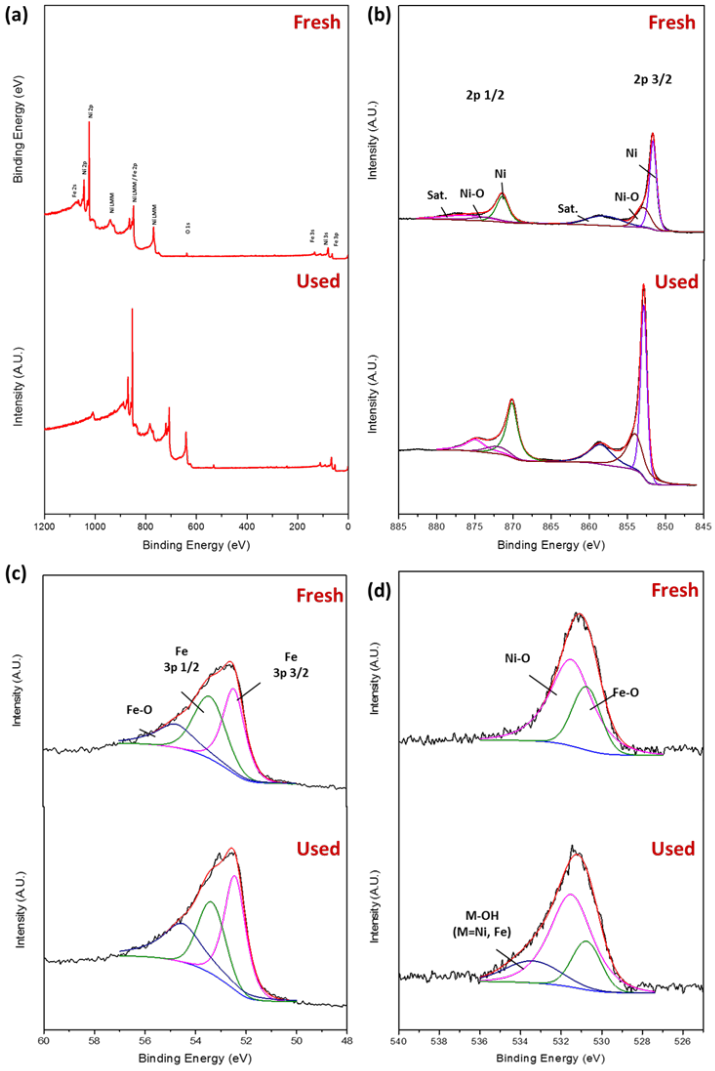

Figure 3.21 XPS spectra of (a) survey (b) Ni 2p core and Fe 3p core and O 1s core of fresh and used Ni_6Fe_4

3.4 Conclusions

In conclusion, a one-step laser processing method has been developed to prepare thin layer of Ni-Fe electrodes with varied Ni to Fe ratios as the electrocatalyst to replace high-cost noble metal based material for oxygen evolution reaction. The alloying of Ni-Fe allowed electrons shift from Ni to Fe, causing the increase of d-vacancy of Ni, resulting in a catalyst matching better to the reaction electron transfer coordination without affect the Fermi level of Ni. In addition, the alloying process, coupled with laser induced rapid solidification, promoted the formation of ultra-small $FeNi_3$ phase grains that effectively increases the number of active sites on the crystal surface; and increased the average lattice spacing to match better with the species involved in the OER reaction. Among the compositions tested, the laser processed Ni_6Fe_4 alloy exhibited an excellent activity of an OER current density of 100 mA/cm^2 at 464 mV overpotential in 1 M KOH aqueous solution, which is among the best-performance OER electrocatalyst reported to date, and maintained a stable performance for at least 18 hours. This excellent OER catalytic performance is attributed to the synergic effect from both Ni and Fe content and the unique microstructures obtain in the laser-based manufacturing process, resulting in a material with superior catalytic activity and durability. The application of laser-based manufacturing can lead to novel electrocatalyst synthesis with easy composition control, favorable microstructures, and complex 3D structures.

3.5 References

1. Cui, X.; Xu, W.; Xie, Z.; Wang, Y., Hierarchical SnO2@SnS2 Counter Electrodes for Remarkable High-efficiency Dye-sensitized Solar Cells. *Electrochimica Acta* **2015,** *186*, 125-132.

2. Cui, X.; Xie, Z.; Wang, Y., Novel CoS2 embedded carbon nanocages by direct sulfurizing metal-organic frameworks for dye-sensitized solar cells. *Nanoscale* **2016,** *8* (23), 11984-11992.

3. Wang, Z.; Spivey, J. J., Effect of ZrO2, Al2O3 and La2O3 on cobalt–copper catalysts for higher alcohols synthesis. *Applied Catalysis A: General* **2015,** *507* (Supplement C), 75-81.

4. Wang, Z.; Laddha, G.; Kanitkar, S.; Spivey, J. J., Metal organic framework-mediated synthesis of potassium-promoted cobalt-based catalysts for higher oxygenates synthesis. *Catalysis Today* **2017,** *298* (Supplement C), 209-215.

5. Zhang, J.; Zhao, Z.; Xia, Z.; Dai, L., A metal-free bifunctional electrocatalyst for oxygen reduction and oxygen evolution reactions. *Nat. Nanotechnol.* **2015,** *10* (5), 444-452.

6. Trotochaud, L.; Young, S. L.; Ranney, J. K.; Boettcher, S. W., Nickel-Iron Oxyhydroxide Oxygen-Evolution Electrocatalysts: The Role of Intentional and Incidental

Iron Incorporation. *J. Am. Chem. Soc.* **2014,** *136* (18), 6744-6753.

7. Trotochaud, L.; Ranney, J. K.; Williams, K. N.; Boettcher, S. W., Solution-Cast Metal Oxide Thin Film Electrocatalysts for Oxygen Evolution. *J. Am. Chem. Soc.* **2012,** *134* (41), 17253-17261.

8. Gulyaev, B. B.; Ganeev, A. A.; Shpakov, V. I., Phase diagrams of binary nickel alloys. *Krasnoyarsk. Inst. Tsvet. Metal. [Sb. Tr.]* **1972,** *No. 5*, 56-61.

9. Vernyhora, I.; Tatarenko, V.; M. Bokoch, S., *Thermodynamics of f.c.c.-Ni–Fe Alloys in a Static Applied Magnetic Field*. 2012; Vol. 2012.

10. Cui, X.; Xu, W.; Xie, Z.; Dorman, J. A.; Gutierrez-Wing, M. T.; Wang, Y., Effect of dopant concentration on visible light driven photocatalytic activity of Sn1-xAgxS2. *Dalton Transactions* **2016,** *45* (41), 16290-16297.

11. Caputi, L. S.; Jiang, S. L.; Amoddeo, A.; Tucci, R., Oxygen-nickel bond length in Ni(111)-O determined by electron-energy-loss fine-structure spectroscopy. *Physical Review B* **1990,** *41* (12), 8513-8515.

12. A.B., S.; N., H.; G., L., Influence of the particle size distribution on surface quality and mechanical properties in AM steel parts. *Rapid Prototyping Journal* **2011,** *17* (3), 195-202.

13. Zhang, Q.; Chen, N.; Hua, Z.; Pang, S., DOS investigation of 3d transition metals by ionization loss spectroscopy. *Vacuum* **1992,** *43* (11), 1137-9.

14. Kaurila, T.; Saeisae, L.; Vaeyrynen, J., Resonant photoemission from iron films on copper. *J. Phys.: Condens. Matter* **1994,** *6* (27), 5053-60.

15. McIntyre, N. S.; Zetaruk, D. G., X-ray photoelectron spectroscopic studies of iron oxides. *Anal. Chem.* **1977,** *49* (11), 1521-9.

16. Venezia, A. M.; Bertoncello, R.; Deganello, G., X-ray photoelectron spectroscopy investigation of pumice-supported nickel catalysts. *Surf. Interface Anal.* **1995,** *23* (4), 239-47.

17. Nahir, T. M.; Clark, R. A.; Bowden, E. F., Linear-Sweep Voltammetry of Irreversible Electron Transfer in Surface-Confined Species Using the Marcus Theory. *Analytical Chemistry* **1994,** *66* (15), 2595-2598.

18. Gong, M.; Dai, H., A mini review of NiFe-based materials as highly active oxygen evolution reaction electrocatalysts. *Nano Research* **2015,** *8* (1), 23-39.

19. Hoang, T. T. H.; Gewirth, A. A., High Activity Oxygen Evolution Reaction Catalysts from Additive-Controlled Electrodeposited Ni and NiFe Films. *ACS Catalysis*

2016, *6* (2), 1159-1164.

20. Cui, X.; Xu, W.; Xie, Z.; Wang, Y., High-performance dye-sensitized solar cells based on Ag-doped SnS2 counter electrodes. *J. Mater. Chem. A* **2016,** *4* (5), 1908-1914.

21. Xu, W.; Cui, X.; Xie, Z.; Dietrich, G.; Wang, Y., Integrated Co3O4/TiO2 Composite Hollow Polyhedrons Prepared via Cation-exchange Metal-Organic Framework for Superior Lithium-ion Batteries. *Electrochimica Acta* **2016,** *222* (Supplement C), 1021-1028.

22. Xu, W.; Xie, Z.; Cui, X.; Zhao, K.; Zhang, L.; Mai, L.; Wang, Y., Direct growth of an economic green energy storage material: a monocrystalline jarosite-KFe3(SO4)2(OH)6-nanoplates@rGO hybrid as a superior lithium-ion battery cathode. *Journal of Materials Chemistry A* **2016,** *4* (10), 3735-3742.

23. Fabbri, E.; Habereder, A.; Waltar, K.; Kotz, R.; Schmidt, T. J., Developments and perspectives of oxide-based catalysts for the oxygen evolution reaction. *Catal. Sci. Technol.* **2014,** *4* (11), 3800-3821.

24. Duan, J.; Chen, S.; Jaroniec, M.; Qiao, S. Z., Heteroatom-Doped Graphene-Based Materials for Energy-Relevant Electrocatalytic Processes. *ACS Catal.* **2015,** *5* (9), 5207-5234.

25. Gong, M.; Dai, H., A mini review of NiFe-based materials as highly active oxygen evolution reaction electrocatalysts. *Nano Res.* **2015,** *8* (1), 23-39.

26. Franco, D. V.; Da Silva, L. M.; Jardim, W. F.; Boodts, J. F. C., Influence of the electrolyte composition on the kinetics of the oxygen evolution reaction and ozone production processes. *J. Braz. Chem. Soc.* **2006,** *17* (4), 746-757.

27. Doyle, R. L.; Lyons, M. E. G., The Oxygen Evolution Reaction: Mechanistic Concepts and Catalyst Design. In *Photoelectrochemical Solar Fuel Production: From Basic Principles to Advanced Devices*, Giménez, S.; Bisquert, J., Eds. Springer International Publishing: Cham, 2016; pp 41-104.

28. Miller, E. L.; Rocheleau, R. E., Electrochemical behavior of reactively sputtered iron-doped nickel oxide. *J. Electrochem. Soc.* **1997,** *144* (9), 3072-3077.

29. Brion, D., Photoelectron spectroscopic study of the surface degradation of pyrite (FeS2), chalcopyrite (CuFeS2), sphalerite (ZnS), and galena (PbS) in air and water. *Appl. Surf. Sci.* **1980,** *5* (2), 133-52.

30. Kim, K. S.; Winograd, N., X-ray photoelectron spectroscopic studies of nickel-oxygen surfaces using oxygen and argon ion-bombardment. *Surface Sci.* **1974,** *43* (2), 625-

4 EFFECT OF PROCESSING PARAMETERS ON THE ELECTROCATALYTIC PERFORMANCE OF Ni-Fe ALLOY TOWARD OXYGEN EVOLUTION REACTION

4.1 Overview

Laser-processed alloys under different processing parameters usually experience different special thermal cycles that could produce anisotropic and heterogeneous microstructures significantly different. The processing history is a decisive factor to the resulting microstructure of a laser-processed alloy, which is affected by many factors such as laser energy density, thermal conductivity of each component in the alloy, the geometry of the produced part and the surrounding environment. Apparently, the laser power density is one of the most controllable factors during laser based manufacturing process, which is significantly affected by the laser scanning speed. Herein, in this chapter, the laser-processed Ni-Fe alloys are prepared by varied laser scanning speeds. Their microstructures and morphologies are examined by XRD and SEM. Their electrocatalytic performance toward OER electrocatalyst is studied. In addition Ni-Fe alloys prepared by arc melting and spark plasma sintering are also prepared for comparison.

4.2 Experimental

4.2.1 Fabrication of NiFe alloys

To laser process NiFe alloys, commercial nickel (3-7 micron, Alfa Aesar, >99.9%, metals basis) and iron (power (fine), Sigma Aldrich, >99%, metals basis) powders, with nickel to iron ratios = 6:4 due to its optimal performance from the results of our previous study[1], were well mixed inside a polystyrene ball mill jar. Then the powders were pressed in a dry pressing die. The as-prepared samples were placed into the chamber of a custom-developed laser processing system with an ytterbium fiber laser (model: VLR-200-AC-Y11) and a ProSeries II scan head. The chamber was protected by argon gas. The laser beam scanned the surface of the samples at a power of 175 W with a spot size of 50 μm at scan speeds of 100 mm/s, 400 mm/s and 1600 mm/s with hatch spacings of 0.120 mm, 0.064 mm and 0.035 mm, respectively. The resulted alloys were labeled as LP_100, LP_400 and LP_1600, respectively. The arc melted Ni-Fe alloys are prepared by placing the die compressed samples into the chamber of an arc melting system (model Edmund Bühler/MAM-1). During the melting process, the ingots were inverted and re-melted for 4 times to ensure homogeneity. The resulted sample is labeled as AM. The spark plasma sintered sample was prepared by a SPS-211Lx system by increasing the temperature at a ramp of 50 °C/min to 830 °C and maintain for 3 min. The samples were labeled as SPS.

4.2.2 Characterizations and Measurements

The crystal structures of the samples were characterized by an X-ray diffraction (XRD) using a Panalytical Empyrean multipurpose diffractometer equipped with PreFIX modules with Cu Kα radiation. The morphologies of the alloy samples were studied using an FEI Quanta 3D FEG scanning electron microscope (SEM) at an acceleration voltage of 20 kV. The electrochemical measurements were carried out in a three-electrode system using a

CHI 650C electrochemical workstation. The as prepared Ni-Fe alloys served as the working electrode in a 1 M KOH aqueous electrolyte, with Pt wire and saturated calomel (SCE) as counter electrode and reference electrode, respectively. Linear sweep voltammetry (LSV) was carried out in the potential range of 0 - 1V vs SCE at a scan rate of 2 mV/s. Electrochemical impedance spectra (EIS) measurements were carried out at an overpotential of 438 mV with an applied voltage aptitude of 5 mV in the frequency range from 10^5 Hz to 0.1 Hz.

4.3 Results and Discussions

4.3.1 Ni-Fe Phase Diagram

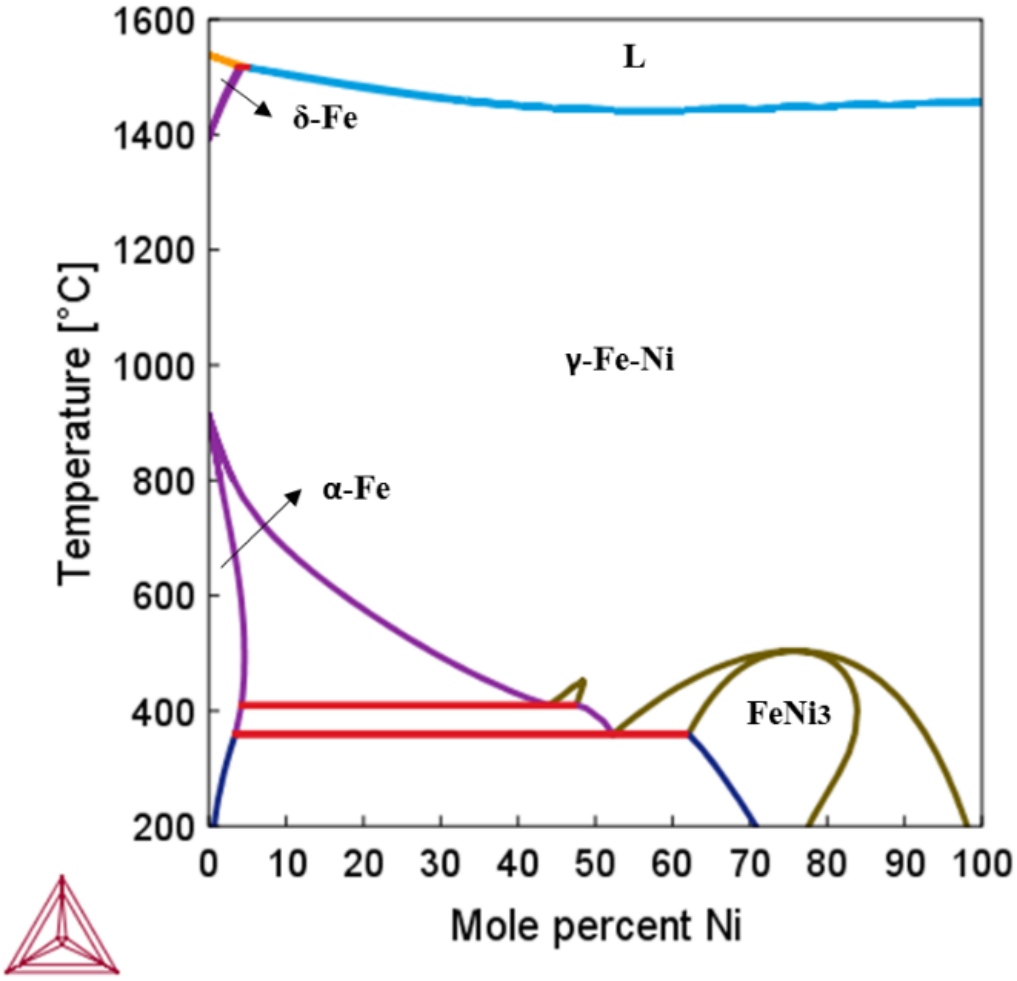

Figure 4.1 Ni-Fe phase binary phase diagram

The Ni-Fe binary phase diagram is displayed in Fig 4-1, predicted using ThermoCalc package. The melting point of Fe and Ni are 1538℃ and 1455℃, respectively. The lowest point of the liquidus line is located at ~1440℃. The separation between the liquidus and solidus line is about 5℃ to 10℃. This diagram contains five equilibrium phases: the liquid phase, L; the BCC δ-Fe solid solution phase; the FCC γ-NiFe solid solution phase; the FCC $FeNi_3$ phase and the BCC α-Fe solid solution phase. Under equilibrium conditions, upon cooling, Ni_4Fe_6 first solidifies from liquidus line to γ-NiFe phase. Then the γ-NiFe phase gradually transits to the $FeNi_3$ phase and $(FeNi_3$+ α-Fe$)_E$ eutectic phase. When temperature further decreases, α-Fe phase starts to precipitate. According to the symmetric trapezoid configuration of OER diatomic reaction in the alkaline environment, the calculated optimal lattice spacing to facilitate O_2 formation for a Ni-based electrocatalyst is ~2.52 Å. In addition, due to the higher coordination number of FCC than BCC, it is more favorable as a catalyst. The lattice spacing of its most closely packed plane (111) of the γ-NiFe and $FeNi_3$ are 2.49 Å and 2.51 Å respectively. Therefore, $FeNi_3$ is the most favorable phase toward OER due to its closest geometrical configuration to the optimal one among all phases in the Ni-Fe binary phase diagram.

4.3.2 Crystal Structure by XRD Spectra

To experimentally characterize the crystal structure of Ni-Fe alloys prepared by varied laser scanning speeds, spark plasma sintering and arc melting, their XRD patterns are displayed in Fig. 4-2. The XRD spectrum of the arc melted Ni_6Fe_4 have peaks at 2θ = 44.12°, 51.40° and 75.66°, corresponding to (111), (200) and (220) planes of FCC $FeNi_3$ (JCPDF no. 03-065-3244). It can been seen, during the arc melting process, cooling rate is relatively slow, the low temperature $FeNi_3$ phase is well developed. The spectrum of the spark plasma sintering Ni_6Fe_4 has a major FCC peak with 2θ = 44.61°, 51.98° and 76.59°, corresponding to (111), (200) and (220) planes of γ-NiFe (JCPDF no. 01-070-0989). In addition, it has peaks with minor intensity which can be identified to $FeNi_3$ and α-Fe (JCPDF no. 00-001-1252) phases. This is because under the localized spark plasma sintering process 830 °C, mass diffusion is limited. The formation of $FeNi_3$ phase is hindered. Therefore, due to a higher content of $FeNi_3$ in arc melted sample, it is expected to display a higher electrocatalytic than activity toward OER. For the laser processed sample scanned at 100 mm/s, it can be well identified to $FeNi_3$ phase. When increasing the scan speed to 400 mm/s, γ-NiFe peaks show up in the spectrum, displaying similar intensity to $FeNi_3$ peaks. Further increasing the scan speed to 1600 mm/s, the intensity of γ-NiFe peaks are getting even higher, with a small peak from α-Fe. This is because, at a low scan speed, the cooling rate is lower with the thermal process closer to the equilibrium conditions. Therefore, low temperature phases are better developed. When increasing the scan speed, the cooling rate is dramatically increased, leading to the precipitation of high temperature phases. Furthermore, a higher cooling also limits the mass diffusion and resulted in the formation of α-Fe phase.

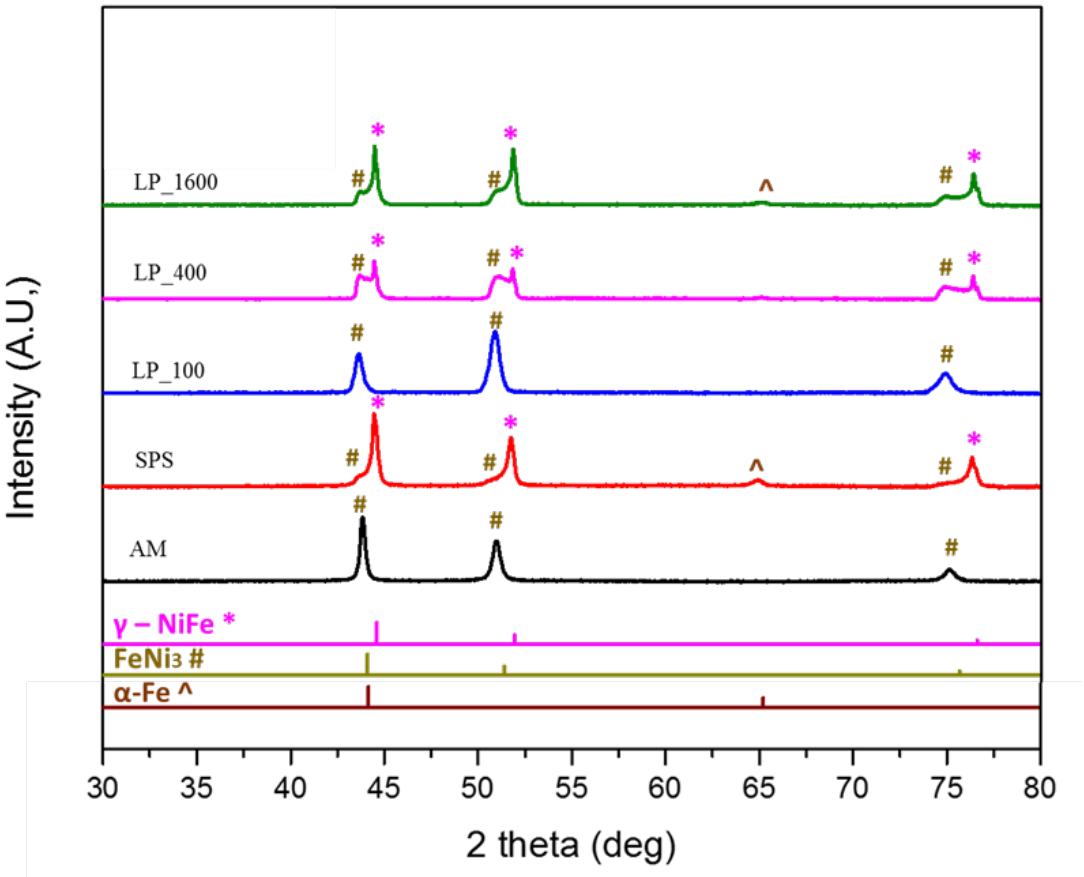

Figure 4.2 XRD spectra of laser-processed Ni_6Fe_4 with different scan speeds, arc melted and spark plasma sintered Ni_6Fe_4

4.3.3 Surface Morphology by SEM

The surface morphology of Ni-Fe alloys prepared by varied laser scanning speeds, spark plasma sintering and arc melting are characterized by SEM images in Fig 4-3. As displayed in Fig. 4-3 (a) and (b), the surfaces of laser processed sample scanned at 100 mm/s is composed of parallel scan tracks bonded to each other coherently. The majority of the pores are distributed along the molten tracks. When increasing the scan speed to 400 mm/s as shown in Fig. 4-3 (c) and (d) the surface is getting much rougher, the porosity is getting higher with decreased pore sizes. When further increasing the speed to 1600 mm/s, Fig.4-3 (e) and (f), the pores are denser resulting in a highly porous surface. Comparably, the surface of arc melted sample, Fig.4-3 (h), and spark plasma sintered sample, Fig.4-3 (g), the surfaces are relatively smooth. It can be seen, an increased scanning speed will lead to rougher and more porous surface. A highly porous surface usually have more surface active sites. Therefore the laser-processed samples may have more surface imperfectness to facilitate the heterogeneous reactions.

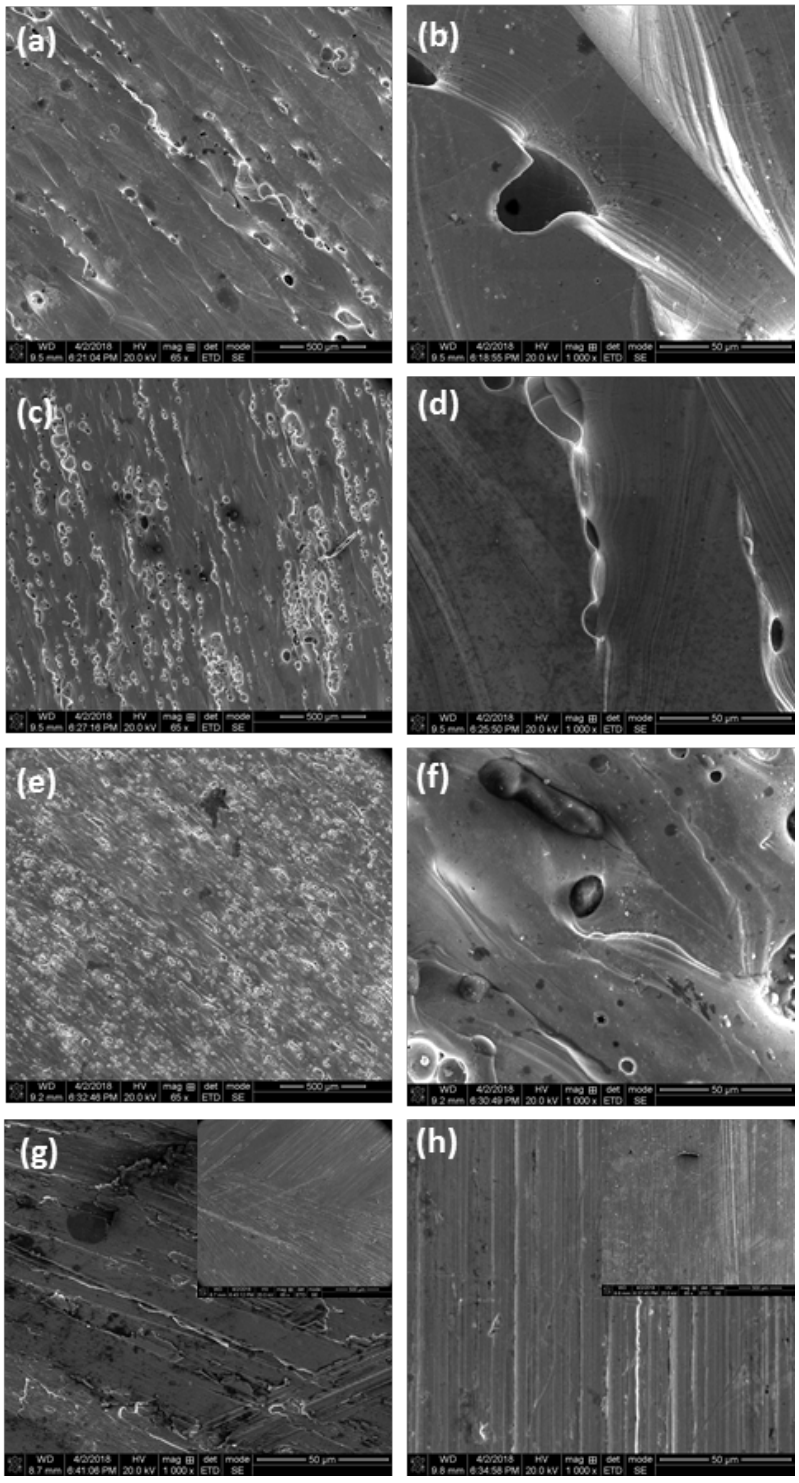

Figure 4.3 Surface morphologies of (a) &(b) LP_100, (c)&(d) LP_400, (e)&(f) LP_1600, (g) SPS and (h) AM samples

4.3.4 Catalytic Performance by LSV

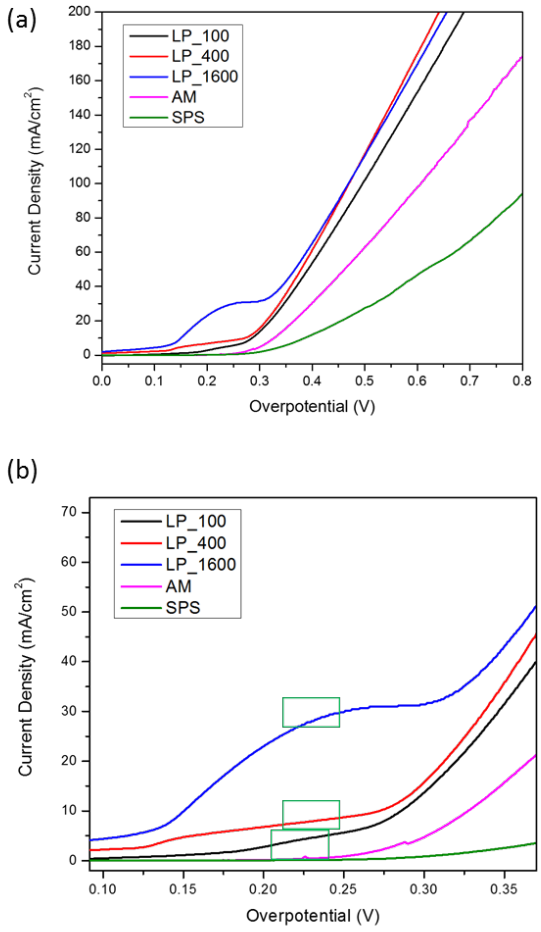

Figure 4.4 (a) LSV of laser-based additive manufactured, arc melted and spark plasma sintered Ni_6Fe_4 electrode toward OER (b) enlarged area of LSV spectra

To evaluate the electrocatalytic performance, LSV was carried out on Ni-Fe alloys prepared by varied laser scanning speeds, spark plasma sintering and arc melted electrodes in a 1 M KOH aqueous electrolyte (Fig. 4-4). It is observed in Fig. 4-4 (b), there is a peak before the onset overpotential of OER due to the oxidization of $Ni(OH)_2$ to NiOOH. It can be seen the oxidization peak area is increasing with the increasing the scanning speed, suggesting an obvious increased electrode surface area.[2-4] It is observed, the spark plasma sintered electrode exhibits the lowest activity toward OER with an onset overpotential of 308 mV. Comparably, the performance of arc melted electrode is apparently higher with an onset overpotential of 289 mV. It can be seen since arc melted sample is composed of more catalytic favorable phase ($FeNi_3$) toward OER, its crystal structure matches better with the OER coordination, which effectively facilitates the catalytic reaction. It is also observed the performance of laser processed samples are further increased due to the

significantly increased surface area as a result of more porous surface. The LP_100, LP_400 and LP_1600 samples have onset overpotentials of 269 mV, 275 mV and 297 mV, respectively. It can be seen, since LP_100 has a higher content of $FeNi_3$ phase, it requires a lower potential to initiate OER. In addition the LP_100, LP_400 and LP_1600 samples requires 495 mV, 469 mV and 459 mV to receive 100 mA/cm^2 current density, respectively. It can been, the significantly increased surface area that can increase the rate of electron transfer. In addition, due to the existence of surface imperfectness provide more active sites on the surface for catalytic reactions. Moreover, due to the fast solidification during laser processing, more residue strain is remained in the alloy, resulting in a more non-equilibrium state possessing higher potential energy that is expected to activate reactions at a faster rate. A good combination of phase and morphology could contribute to the best performance.

4.3.5 Tafel Slope and EIS spectra

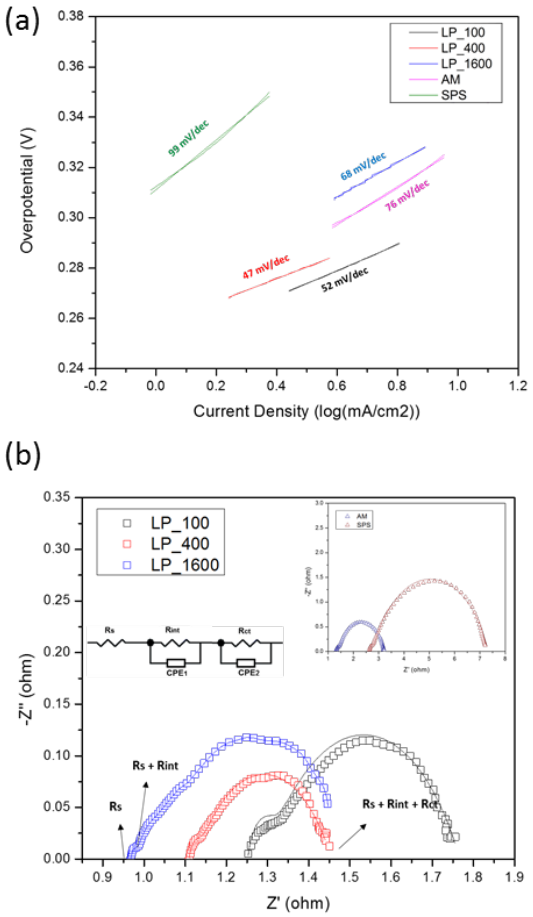

Figure 4.5 (a) Tafel slopes of laser-based additive manufactured, arc melted and spark plasma sintered Ni_6Fe_4 electrode toward OER (b) EIS spectra of laser-based processed, arc melted and spark plasma sintered Ni_6Fe_4 electrode toward OER

Table 4.1 Electrochemical characteristics

	R_s (Ω cm^2)	R_{int} (Ω cm^2)	CPE_1 (F s^{n-1} cm^{-2})	n_1	R_{ct} (Ω cm^2)	CPE_2 (F s^{n-1} cm^{-2})	n_2
LP_100	1.252	0.050	1.176	0.999	0.465	0.140	0.607
LP_400	1.094	0.019	3.467	0.999	0.327	0.283	0.592
LP_1600	0.967	0.010	3.662	0.999	0.523	0.537	0.530
AM	1.314	0.104	0.598	0.999	1.800	0.0186	0.748
SPS	2.625	0.1256	0.492	0.999	4.587	0.0148	0.724

The Tafel slopes of laser-processed, arc melted and spark plasma sintered Ni_6Fe_4 electrode are plotted in Fig. 4-5 (a). The linear regions of polarization curves fitted to Tafel plots, using the equation $\eta = a + b \log (j)$, where b is the Tafel slope to determine the kinetic constant of electrode reactions. A small slope of Tafel plot indicates rapid electron transfer at the electrode and electrolyte interface at the applied potentials. As displayed, the slope values of the SPS, AM, LP_100, LP_400 and LP_1600 electrodes are 76, 99, 52, 47 and 68 mV/decade, respectively. The lower Tafel slope of laser-processed samples is contributed by rougher surfaces, which increase active sites on the electrode surface and effectively accelerate electron transfer process at the electrode and electrolyte interface. The Nyquist plots of EIS were taken at an overpotential of 438 mV in the frequency range of 10^5 Hz to 0.1 Hz on different electrodes shown in Fig. 4-5 (b). The equivalent circuit is simulated by CHI 650 C electrochemical workstation with the fitted results listed in Table 1. The equivalent circuit is composed of R_s - solution resistance, R_{int} – electrode/electrolyte interface resistance, R_{ct} – charge transfer resistance, C_{int} – interfacial capacitance and C_{dl} – double layer capacitance. The intercept of the plot with the real axis at high frequency range (R_s) represents the overall ohmic resistance, including the bulk resistance of the material, series resistance and contact resisitance.[5] The semicircle at medium frequency range is from metal hydroxide intermediates formation and absorption process, whose diameter (R_{int}) indicates the rate of the electrode/electrolyte interfacial process.[6] It is observed, the overall resistance of laser processed samples are significantly smaller than that of AM and SPS samples, indicating their overall better catalytic performance. Firstly, the R_{int} of laser processed samples are significantly smaller, indicating a faster OH^- absorption and intermediates formation at the electrode/electrolyte interface. The

semicircle on low frequency range describes the electron charge transportation process of OH^-/O_2 redox reaction at the electrode/electrolyte interface[6], with a diameter of R_{ct} representing the charge transfer resistance between reactant to product. A smaller R_{ct} indicates a faster electron transfer. It is found, due to formation of more pores during laser processing, the overall electrocatalytic activity is apparently improved by the effectively increased specific surface area and active sites. The nanostructure enhances the reactant absorption and intermediates formation, and accelerates the electrode/electrolyte interface electron transfer. And the interconnected micro channels increase the pathways for mass transfer and facilitate the ion diffusion and gas transportation.

4.4 Conclusions

In conclusion, the processing history is a decisive factor to the microstructure of a laser-processed alloy. The laser power density significantly impact the phase composition and surface morphology of the electrocatalyst. It can be seen, the arc melted sample displayed much higher activity than spark plasma sintered samples due to its more favorable composition toward oxygen evolution reaction. It is also observed, the laser-processed samples displayed apparent higher electrocatalytic activity toward the oxygen evolution reaction, due to its rougher surface and more residue strain as a result of the special thermal cycle during laser processing. Herein, laser-processing may provide new insight on develop novel electrocatalyst by controlling the microstructures.

4.5 References

1. Cui, X.; Zhang, B.; Zeng, C.; Wen, H.; Yao, H.; Guo, S., Laser processed Ni-Fe alloys as electrocatalyst toward oxygen evolution reaction. *Materials Research Express* **2018**.

2. Cui, X.; Xu, W.; Xie, Z.; Wang, Y., High-performance dye-sensitized solar cells based on Ag-doped SnS2 counter electrodes. *J. Mater. Chem. A* **2016,** *4* (5), 1908-1914.

3. Xu, W.; Cui, X.; Xie, Z.; Dietrich, G.; Wang, Y., Integrated Co3O4/TiO2 Composite Hollow Polyhedrons Prepared via Cation-exchange Metal-Organic Framework for Superior Lithium-ion Batteries. *Electrochimica Acta* **2016,** *222* (Supplement C), 1021-1028.

4. Xu, W.; Xie, Z.; Cui, X.; Zhao, K.; Zhang, L.; Mai, L.; Wang, Y., Direct growth of an economic green energy storage material: a monocrystalline jarosite-KFe3(SO4)2(OH)6-nanoplates@rGO hybrid as a superior lithium-ion battery cathode. *Journal of Materials Chemistry A* **2016,** *4* (10), 3735-3742.

5. Cui, X.; Xie, Z.; Wang, Y., Novel CoS2 embedded carbon nanocages by direct sulfurizing metal-organic frameworks for dye-sensitized solar cells. *Nanoscale* **2016,** *8* (23), 11984-11992.

6. Franco, D. V.; Da Silva, L. M.; Jardim, W. F.; Boodts, J. F. C., Influence of the

electrolyte composition on the kinetics of the oxygen evolution reaction and ozone production processes. *J. Braz. Chem. Soc.* **2006,** *17* (4), 746-757.

5. MONOLITHIC NANOPOROUS Ni-Fe ALLOY BY DEALLOYING LASER PROCESSED Ni-Fe-Al AS ELECTROCATALYST TOWARD OXYGEN EVOLUTION REACTION

5.1 Overview

Besides an ideal composition, an optimal OER catalysis requires sufficient active surface area.[1-4] The catalytic activity of an electrocatalyst is significantly affected by the size, which not only influences the localized electronic structure on the surface, but also alters the availability of active sites. The most effective and straightforward strategy to increase the surface area of the catalyst is to develop nanostructures to decrease the particle size and increase porosity. The catalyst with particle size above or below the optimal size range would cause the loss of activity. During the particle size reduction process, more kink structure starts to expose on the surface to serve as catalytic active centers. However, if the particle size is below the minimum range, it can cause the d-band center shift and Fermi level change to some degree, which may leads to an ineffective interaction between the electrocatalyst surface and adsorbed species. In addition, the catalytic activity of the metal electrocatalyst is significantly affected by the shape of particles. An exposed surface composed of more steps can effectively increase the catalytic performance. The nanostructure is usually seeded by the nucleation center from aggregation of atoms, which can give rise to different nanostructures, such as nanowires, nanosheets, nanocube and nanoflowers. The shapes of the final structures are decided by the surface energies of different crystal planes. The crystal surface can usually get rid of planes with high surface energies; planes with low-index planes lead the formation of shapes of crystals.

Compared to traditional powder-based electrocatalysts, monolithic electrocatalyst displays great advantages in simplifying the electrode assembling process and avoiding electrical connection issues.[5] For example, for hydrogen generation, Xie et al. reported a self-standing monolithic cobalt oxide array for $NaBH_4$ hydrolysis that effectively inhibited catalyst aggregation and avoided the tedious and time-consuming process for catalyst separation.[6] As a rapidly developing manufacturing method, laser-based additive manufacturing is an excellent technique to prepare complex templates for monolithic electrocatalyst. In addition, laser-based additive manufacturing can achieve the desired alloy compositions without tedious chemical synthesis and can achieve a strong metallic bond to the substrate avoiding the usage of binders. For instance, Laser Powder Stream, or LENS®-Laser Engineered Net Shaping™ process is advantaged in free forming/coating capability to make large and complex parts. Due to the small laser spot size and thus a rapid cooling rate, laser processed parts have unique microstructures and material properties. For example, Cebollero et al. developed thin ceramic membranes for electrolyte-supported solid oxide fuel cells through laser processing which effectively improved the electrolyte-electrode contact and thus reduced cathodic polarizations.[7] Dealloying is an efficient strategy to develop nanostructures, which can develop microscale channels to facilitate mass transfer and nanoscale features to provide more active sites at the same time.[8-10] In

this regard, Xu et al. fabricated nanoporous PtCo and PtNi alloy ribbons through a mild dealloying process. Those materials displayed excellent activity and stability toward methanol electroxidation.[11]

Herein, in this chapter, nanoporous NiFe electrocatalyst is developed by dealloying Ni-Fe-Al alloy prepared by laser-based manufacturing as the electrocatalyst for oxygen evolution reactions for the first time. Their micro- and nano-structures, the surface morphologies and chemical compositions of the nanoporous NiFe electrocatalyst are characterized by SEM, XRD and EDXS. Compared to bulk Ni_6Fe_4 printed by laser-based manufacturing, which requires 464 mV overpotential to receive an OER current density of 100 mA/cm^2, the porous NiFe alloy only requires and overpotential of 442 mV to receive the same performance in 1 M KOH aqueous solution. Preparing the nanoporous NiFe electrocatalyst by dealloying laser processed alloys displays great potential for developing monolithic nanoporous electrode for energy conversion reactions, and provides new insights on electrode structure and composition engineering, which may pave a new way for the efficient and effective development of electrocatalyst.

5.2 Experimental

5.2.1 Fabrication of $Ni_6Fe_4Al_{10}$ alloys

To fabricate the $Ni_6Fe_4Al_{10}$ alloy by laser-based manufacturing, commercial nickel (3-7 micron, Alfa Aesar, >99.9%, metals basis), iron (power (fine), Sigma Aldrich, >99%, metals basis) and aluminum (325 mesh, Alfa Aesar, 99.5%, metals basis) powders, with nickel: iron : aluminum ratios = 6:4:10, were well mixed inside a polystyrene ball mill jar. Then the powders were pressed in a dry pressing die with a diameter of 0.5 inch. The as-prepared samples were placed into the chamber of a custom-developed laser processing system with an ytterbium fiber laser (model: VLR-200-AC-Y11) and a ProSeries II scan head. The laser beam scanned the surface of the pressed samples at a power of 77 W with a spot size of 50 μm at a scan speed of 200 mm/s and a hatch spacing of 0.254 mm with the chamber protected by argon gas. A square specimen with a dimension of 7 mm × 7 mm was fabricated in the center of the disk shaped sample. The resulted alloys were labeled as $Ni_6Fe_4Al_{10}$. The bulk Ni_6Fe_4 was fabricated the same way without adding aluminum, and labeled as Ni_6Fe_4_B.

5.2.2 Synthesis of Nanoporous NiFe Electrocatalyst by Dealloying

The bulk Ni-Fe alloy sample was fabricated the same way without adding aluminum, and labeled as NiFe_B. The Ni:Fe ratio is 6:4 due to its optimal performance based on our previous study.[12] To fabricate the monolithic nanoporous Ni-Fe alloy samples, the laser processed NiFeAl alloy samples were dealloyed in 10 wt% KOH aqueous solution for 24 hours. The dealloyed samples were labeled as NiFe_P.

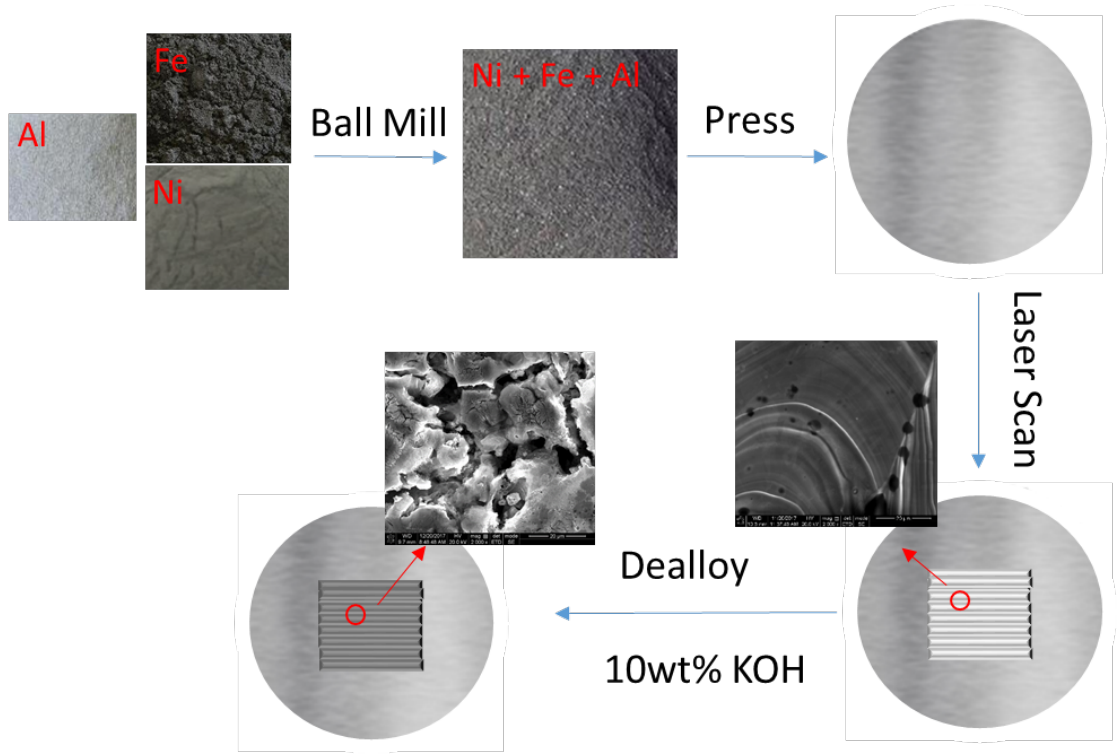

Figure 5.1 Illustration of the fabrication process

5.2.3 Materials Characterizations

The crystal structures of the samples were characterized by an X-ray diffraction (XRD) using a Panalytical Empyrean multipurpose diffractometer equipped with PreFIX modules with Cu Kα radiation. The morphologies of the samples were studied by an FEI Quanta 3D FEG scanning electron microscope (SEM) equipped with energy-dispersive X-ray spectroscopy (EDXS) at an acceleration voltage of 20 kV.

5.2.4 Electrochemical measurements

The electrochemical measurements were carried out in a three-electrode system using a CHI 650C electrochemical workstation. The as prepared samples served as the working electrode in a 1 M KOH aqueous electrolyte, with Pt wire and saturated calomel (SCE) as counter electrode and reference electrode, respectively. Linear sweep voltammetry (LSV) was carried out in the potential range of 0 - 1V vs SCE at a scan rate of 2 mV/s. Electrochemical impedance spectra (EIS) measurements were carried out at an overpotential of 400 mV with an applied voltage aptitude of 5 mV in the frequency range from 10^5 Hz to 0.1 Hz.

5.3 Results and Discussion

5.3.1 Mechanism of Dealloying Process

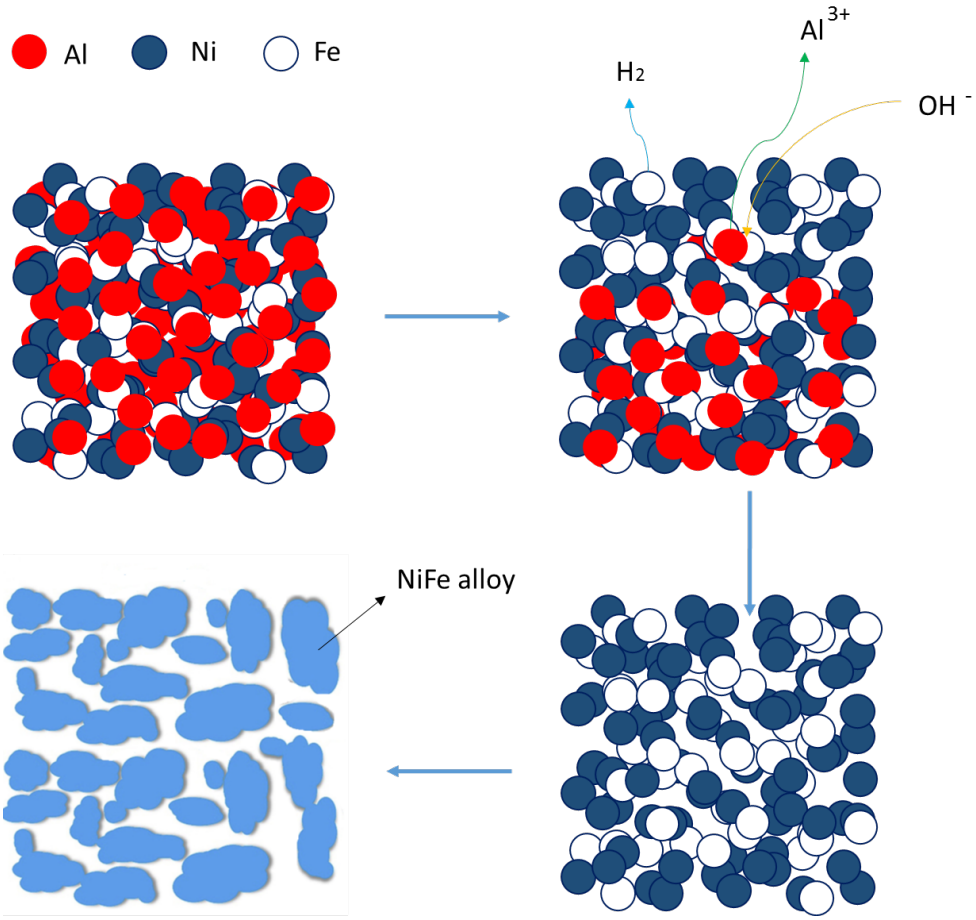

Figure 5.2 Illustration of Ni-Fe-Al dealloying process

The dealloying mechanism is illustrated in Fig. 5-2. At the beginning, Al atoms are rapidly dissolved into the alkaline solution from the alloy matrix, leaving Ni and Fe atoms with a high rate of vacancy. Then, the continuous dissolving of Al causes Ni and Fe enrichment at the solid and liquid interface. Next, Ni and Fe atoms aggregate into more stable crystal nucleus to minimize the surface energy and then grow into grains of Ni-Fe intermetallic compounds. By extending this process, the grains tend to grow into ordered nanostructures. The following reaction happens in the dealloying process:

$$2Al\,(s) + 2OH^-\,(aq) + 2H_2O\,(l) \rightarrow 2AlO_2^-\,(aq) + 3H_2\,(g).$$

5.3.2 Morphology Study by SEM

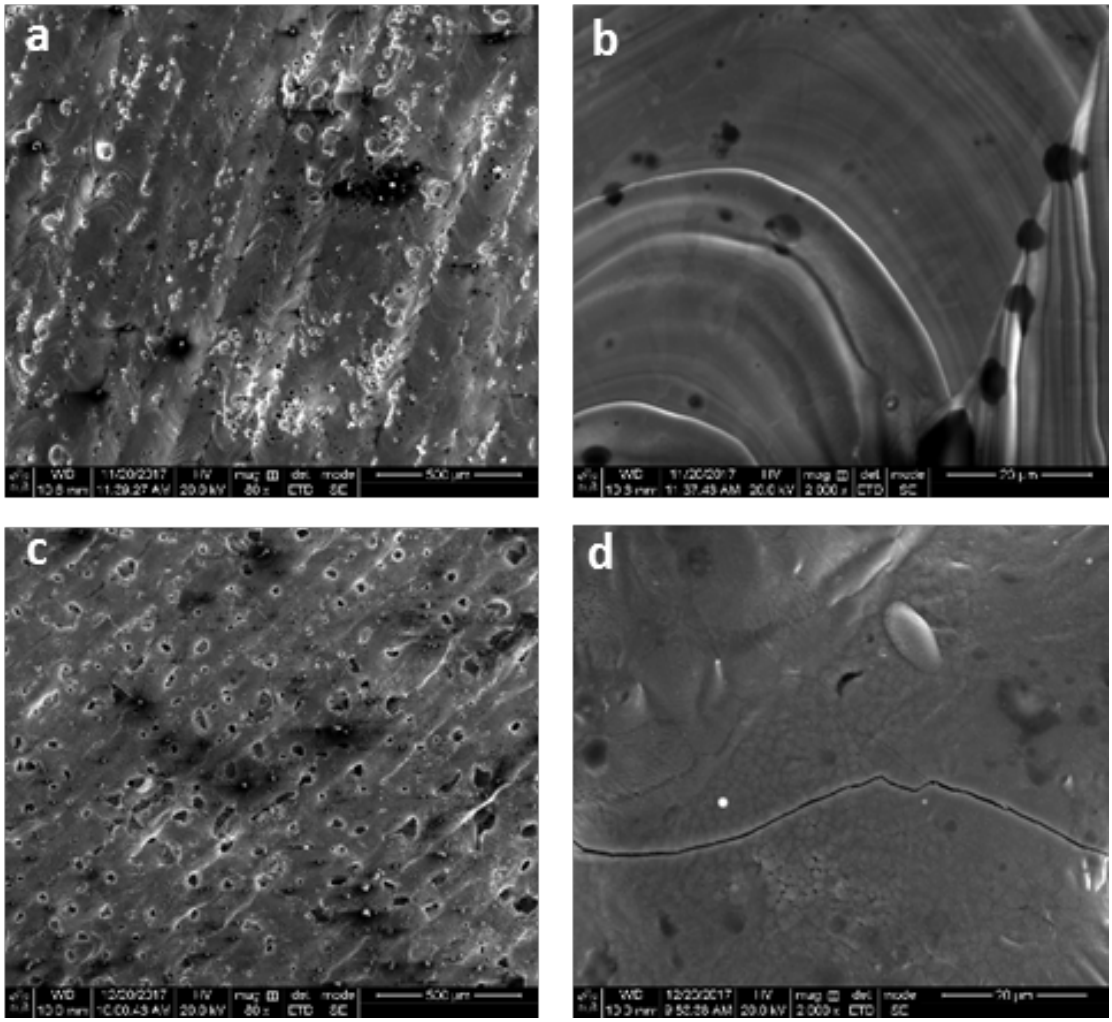

Figure 5.3 SEM images of (a) and (b) Ni_6Fe_4_B, (c) and (d) $Ni_6Fe_4Al_{10}$

The surface morphology of the as-printed Ni_6Fe_4_B and $Ni_6Fe_4Al_{10}$ are characterized by the SEM images. As displayed in Fig. 5-3, the surfaces of Ni_6Fe_4_B and $Ni_6Fe_4Al_{10}$ are both porous composed of parallel scan tracks bonded to each other coherently. In addition, the majority of the pores are distributed along the molten track. It can be seen for the sample added with 50 at. % Al, the surface is much rougher than that of Ni_6Fe_4_B, with the scan tracks very disconnected to each other and a significantly increased porosity. It can also be observed, both the number and size of pores on the $Ni_6Fe_4Al_{10}$ are much higher than those of Ni_6Fe_4_B, resulting in a coarser surface with highly intensified balling, which illustrating the high instability of the melting pool during the melting process of Ni-Fe-Al alloy. Because the melting point of Al (660°C) is critically lower than that of Ni (1455°C) and Fe (1538°C), during the solidification process, Ni and Fe solidify preferentially, leading

to the unsolidified liquid phase enriched with Al, resulting in interrupted melting pools with balls and caves. On the other hand, due to the much larger thermal expansion coefficient of Al (α= 23.1× 10^{-6}/ K, at 20°C) than that of Ni (α= 13× 10^{-6}/ K) and Fe (α= 11.8× 10^{-6}/ K), the thermal coefficient mismatch leads to a large residue stress and surface tension during the rapid cooling of laser processing, resulting in cracks and pores. With the same dwell time of laser on the surface and cooling time, metals suffer a large temperature gradient. The huge difference of the thermal coefficient between Al and other elements leads to a large residue stress and surface tension after cooling done, resulting in the formation of surface cracks. Moreover, in the ternary alloy of Ni-Fe-Al, the phase composition is getting more complicated than Ni-Fe binary alloy, the possibility of secondary and ternary crystals formation is getting higher, the continuity of grain is further disturbed, resulting in a more discontinuous structure. However, as a template for further dealloying process, these structure imperfectness can serve as reaction centers for initializing dealloying process and promoting the formation of nanostructures and micro-channels.

The SEM images of NiFe alloy after dealloying the as-printed $Ni_4Fe_6Al_{10}$ are displayed in Fig. 5-4 (Ni_4Fe_6_P). As observed in Fig. 5-4 (a), the surface of Ni_4Fe_6_P is getting more porous than $Ni_4Fe_6Al_{10}$, and more negative charges build up on Ni_4Fe_6_P, demonstrating a more disconnected metallic structure is formed after the removal of Al, resulted in an apparently decreased electrical conductivity compared to $Ni_4Fe_6Al_{10}$. After slightly increasing the SEM magnitude to Fig. 5-4 (b), it is observed a lot of micro-scale pores are formed throughout the electrode, which can serve as efficient channels for both OH^- ion diffusion through the electrolyte and the produced O_2 gas transportation, which effectively improve the mass conduction in the system. After further increasing the magnification of the images, its clearly observed, different nano/micro-structures are formed. As displayed in Fig. 5-4 (c) (d) and (e) for the area along/inside molten tracks or surface pores, well-defined coral-like structured nanoparticles are clearly observed. The nanocorals have a unit size about 5 microns, with each blade having a size of about 500 nanometer and an ultra-thin thickness. This ultra-small features can effectively increase the surface area of the electrocatalyst by providing more active sites and more material defects such as kinks and steps to enhance catalytic activity. As displayed in Fig. 5-4 (f) (g) and (h) for the area on the top surface with relatively uniform structure, the majority of the surface changed into a nanoarray structure, with ultra-small nanorods with diameters of about 100 nanometer. In addition, ultrathin nanowires are distributed in the array. Therefore, with the dealloying process, a well-defined nanostructure is developed, which significantly improve the surface area of this electrocatalyst and provide more active sites of electrocatalytic reactions. On the other hand, the micro-porous structure effectively increases the pathway for mass transfer and facilitates the ionic diffusion. Overall, through the dealloying process on the laser manufactured Ni-Fe-Al parts, a Ni-Fe based nanoporous electrocatalyst with ultra-high surface area for electrocatalytic reaction and interconnected porous structure for facilitated mass diffusion is derived.

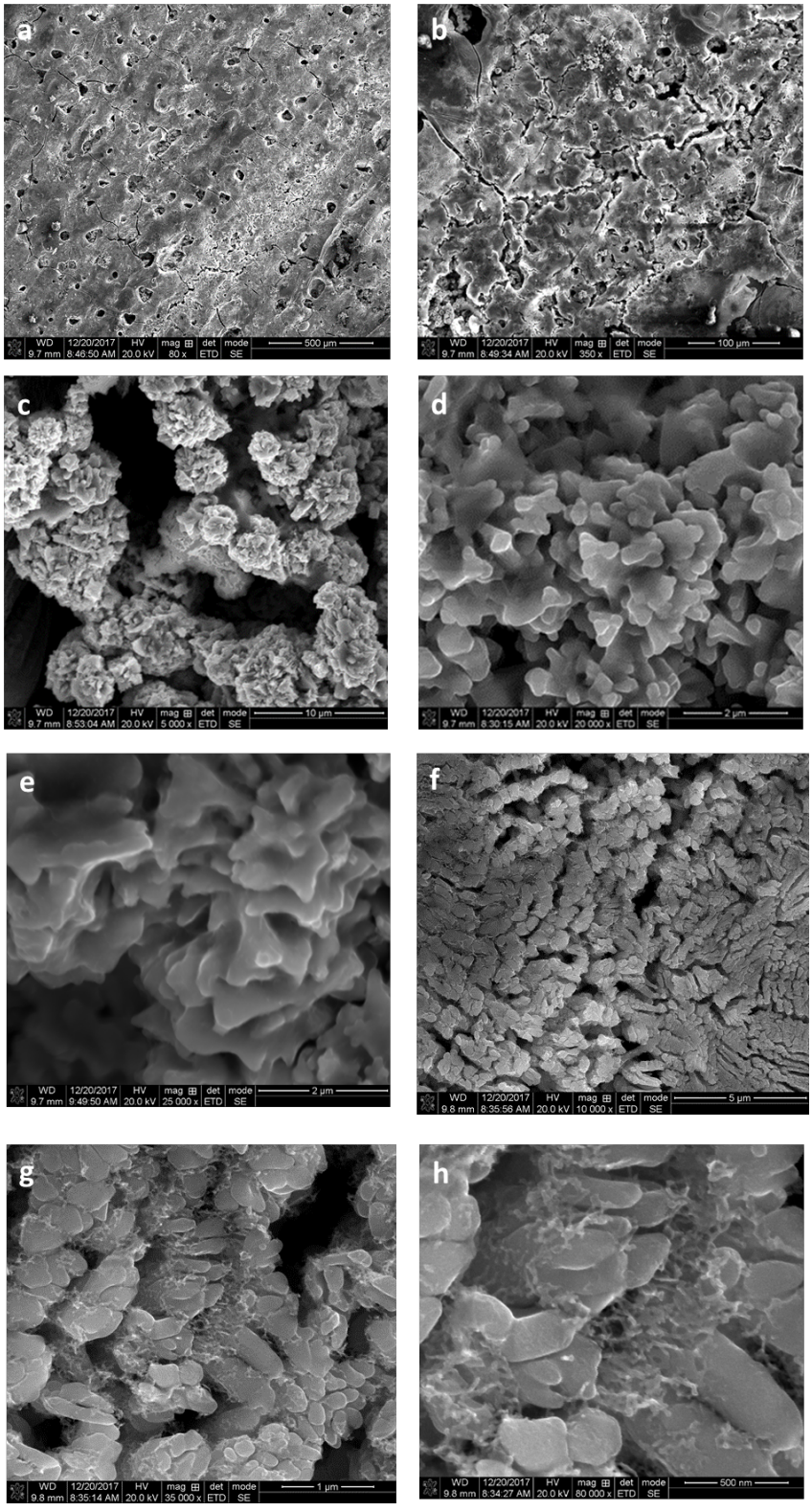

Figure 5.4 SEM images of Ni_6Fe_4_P

5.3.3 Fe-Ni-Al Phase Diagrams

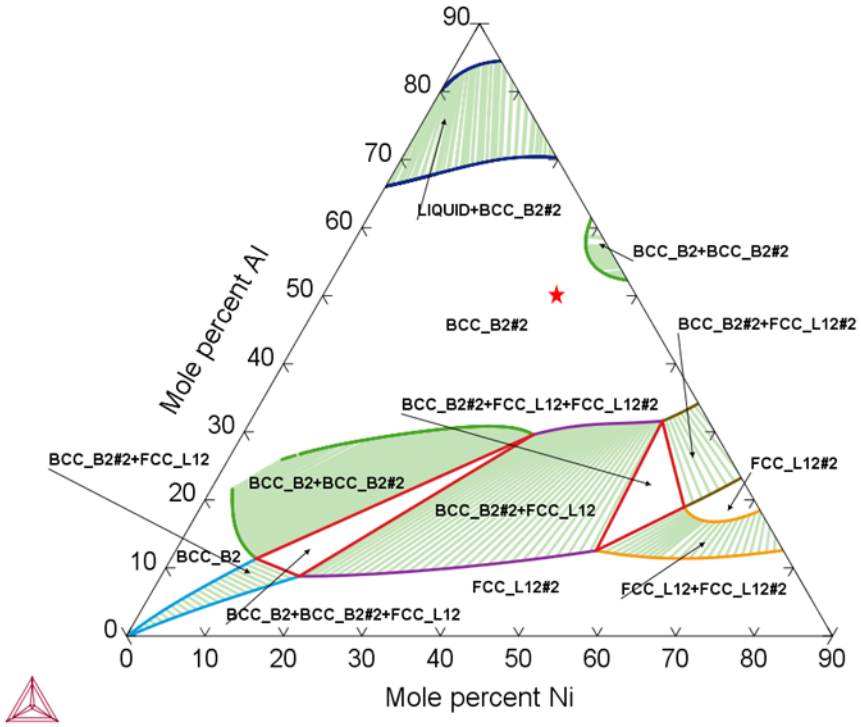

Figure 5.5 Phase diagram of Ni-Fe-Al

Figure5-5 displays the calculated ternary Ni-Fe-Al phase diagram at 900 °C. It can be seen upon solidification, the Ni-Fe-Al alloy with a Ni: Fe: Al atomic ratio = 6:4:10 marked with a red star falls into the region of β_2 phase, with secondary α and γ phases and an Al rich liquidus phase.

5.3.4 Crystal Structure Analysis by XRD

The XRD patterns of NiFe_B, NiFeAl and NiFe_P are displayed in Fig. 5-6. It can be seen that the bulk NiFe_B sample is mainly composed of a FCC structure composed of a γ-Ni (JCPDF card no. 01-070-0989) phase with 2θ = 44.605°, 51.979° and 76.591° corresponding to (111), (200) and (220) planes with the lattice parameter of a = 3.516 Å; a cubic $FeNi_3$ phase (JCPDF card no. 03-065-3244) with 2θ = 44.121°, 51.404° and 75.661° corresponding to (111), (200) and (220) planes with a = 3.552 Å; a cubic taenite FeNi phase (JCPDF card no. 00-003-0016) with 2θ = 43.173 °, 50.674° and 74.679° corresponding to (111), (200) and (220) planes with a = 3.601 Å and trivial amount of α-Fe phase (JCPDF card no. 00-001-1252) with 2θ = 44.142 ° and 65.186° corresponding to (111) and (220) planes with a = 2.860 Å. It is observed from the NiFeAl spectrum, it is composed of a BCC matrix with 2θ =31.101 °, 44.496 ° and 65.059 ° corresponding to (110), (200) and (202)

planes with a=4.060 Å, an FCC structure matrix 2θ = 44.765°, 52.216 and 77.063° corresponding to (111), (200), (220) planes with a = 3.503 Å and a high-intensity cubic Al phase (JCPDF card no. 04-013-0326) with 2θ = 38.510°, 44.765°, 65.165 and 78.317° corresponding to (111), (200), (220) and (311) planes with a = 4.0458 Å. This is because during the rapid thermal cycle of laser processing, the diffusion is highly insufficient and non-equilibrium Al segregations occur. Therefore, the Ni and Fe atoms tend to grow into Ni-Fe intermetallic compounds resulting in a Ni-Fe based BCC and FCC matrixes with minor amount of Al atoms altering lattice distances. For the spectrum of NiFe_P sample, it is clearly found that the Al phase disappeared from the BCC and FCC structures, indicating a successful dealloying process that has removed majority of Al atoms from the alloy matrix. As a result, the nanoporous NiFe_P is mainly composed of Ni-Fe based alloys, which are active components toward OER in the alkaline environment.

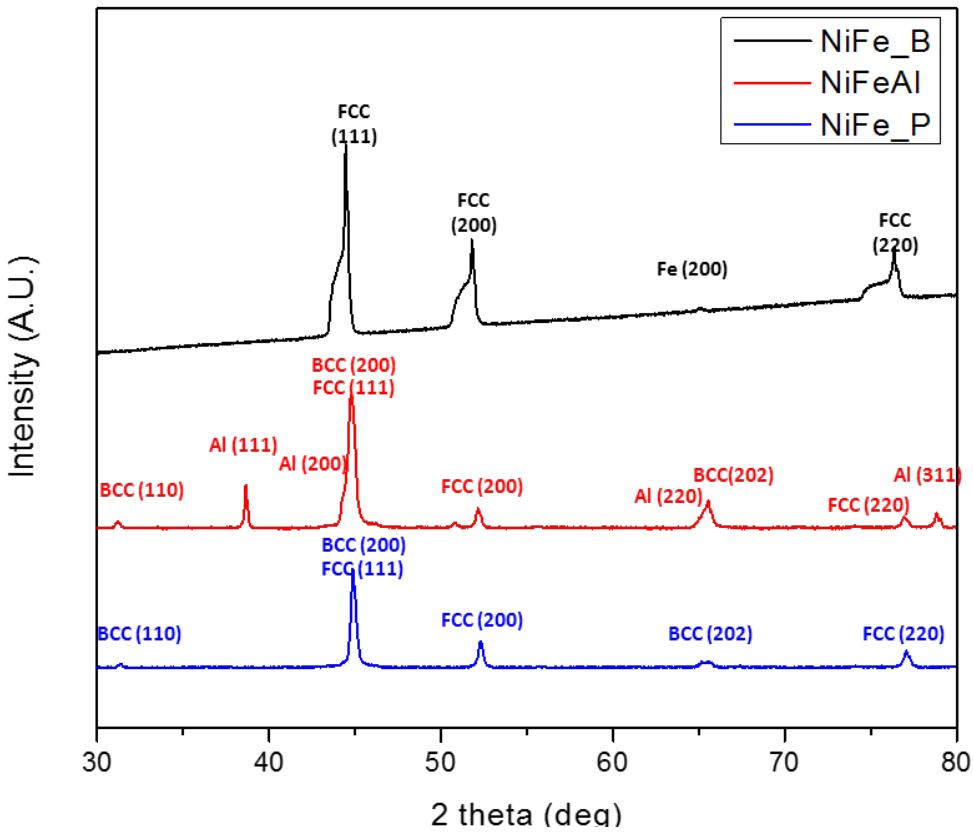

Figure 5.6 XRD spectra of Ni_6Fe_4_B, $Ni_6Fe_4Al_{10}$ and Ni_6Fe_4_P

5.3.5 Elemental Distribution Study by EDXS

EDXS elemental mapping analysis and energy-dispersive spectrum were executed to characterize elemental composition and distribution in the nanoporous NiFe_P sample. It is observed the atomic ratios of Ni, Fe, Al, O are 45 %, 17 %, 8 %, 30%, respectively. The

loss of Fe during the dealloying process is due to the dissolution of Fe into the alkaline solution. As shown in Fig. 5-7 (a) and (b), Ni and Fe atoms are distributed uniformly all over the surface. As shown in Fig. 5-7 (c), the vast majority of surface Al atoms have been dissolved and the signal of Al is mainly from the underneath substrate in the areas exposed through pores of the printed layer. In addition, due to the in-situ metal oxidation and hydroxylation in the dealloying process, oxygen signal is also observed uniformly distributed all over the sample as shown in Fig. 5-7 (d), indicating the formation of M-O (M = Al, Ni, Fe) and M-OH bonds.

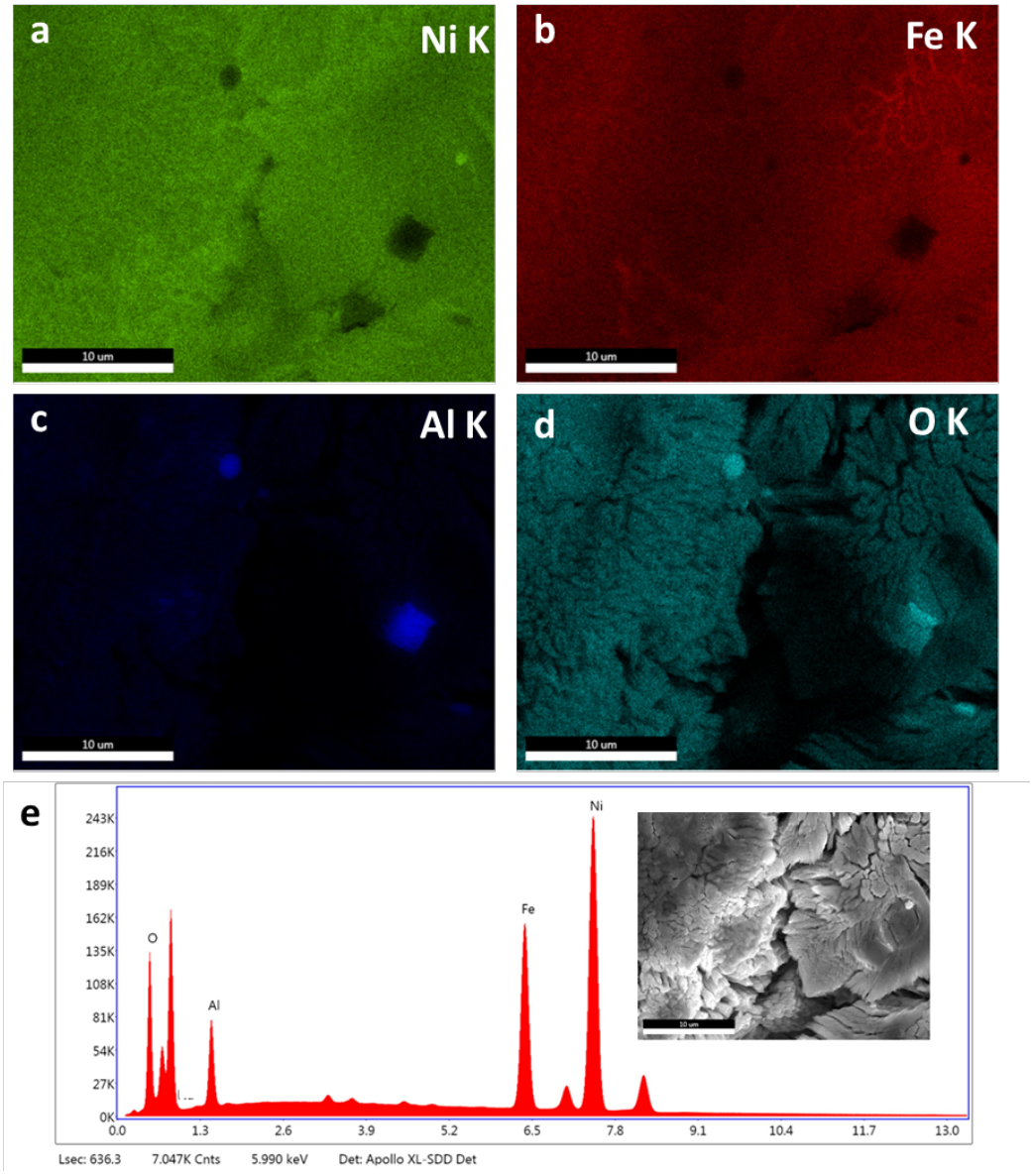

Figure 5.7 (a) (b) (c) and (d) EDXS elemental mappings of Ni, Fe, Al and O elements in used Ni_6Fe_4_P respectively, (e) energy-dispersive spectrum of Ni_6Fe_4_P

5.3.6 Catalytic Performance Study by LSV

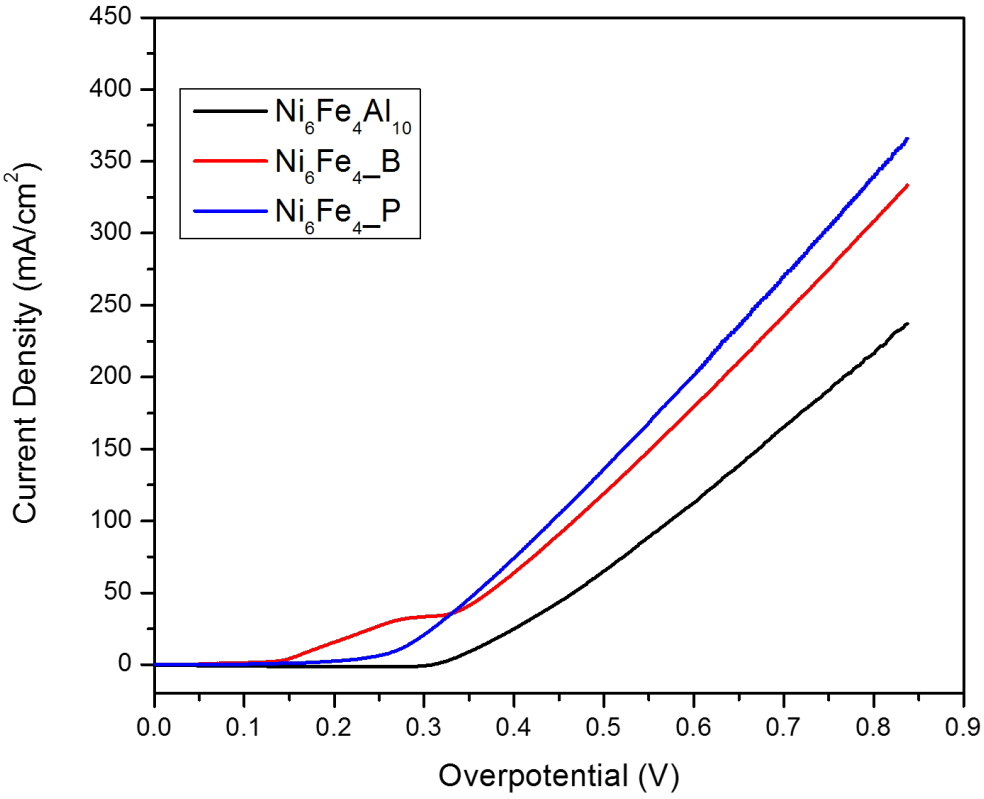

Figure 5.8 The OER polarization curves of $Ni_4Fe_6Al_{10}$, the Ni_4Fe_6_B and Ni_4Fe_6_P electrodes

To evaluate the electrocatalytic performance, LSV was carried out on the NiFeAl, the NiFe_B and NiFe_P electrodes in a 1 M KOH aqueous electrolyte (Fig. 5-8). It is firstly observed that in the alkaline solution, a layer of metal hydroxides rapidly forms on the surface of the NiFe_B electrode at an OER overpotential of ~295 mV due to the oxidation of $Ni(OH)_2$ into NiOOH. No peaks were observed on the spectrum of NiFe_P or NiFeAl due to a full hydroxylation during the dealloying process for NiFe_P sample and thermodynamic hydroxylation favorability of Fe and Al over Ni for NiFeAl sample[13]. It is also observed, the NiFe_B electrode exhibits an apparently lower activity toward OER compared to the nanoporous NiFe_P electrode. The NiFe_B electrode requires an overpotential of 464 mV to reach a 100 mA/cm^2 current density. For nanoporous NiFe_P electrode, it only requires an overpotential of 442 mV to reach an OER current density of 100 mA/cm^2, which is comparable to reported OER electrocatalyst to date[13-17]. At an

overpotential of 500 mV, the LSV current density of NiFe_P is 142 mA/cm^2, while it is only 122 mA/cm^2 and 61 mA/cm^2 for NiFe_B and NiFeAl electrodes. With increased surface area and amount of surface active sites, electron transfer process at the electrode and electrolyte interface is effectively accelerated. In addition, the interconnected microchannel structure increases the amount of pathways for ion and gas diffusion.

Table 5.1 Parameters from linear sweep voltammetry

Sample	Onset Overpotential (mV)	Overpotential for 100 mA/cm^2 OER Current Density (mV)	$Ni(OH)_2$ Oxidization Overpotential (mV)
Ni_6Fe_4_B	320	464	295
$Ni_6Fe_4Al_{10}$	316	575	N/A
Ni_6Fe_4_P	251	442	N/A

5.3.7 Tafel Slopes

The overpotential η vs. log (current density) is plotted in Fig. 5-9. To understand the electrochemical mechanism of the OER catalytic process, the linear regions of polarization curves were fitted to Tafel plots, using the equation $\eta = a + b \log (j)$, where b is the Tafel slope to determine the kinetic constant of electrode reactions. A small slope of Tafel plot indicates rapid electron transfer at the electrode and electrolyte interface at the applied potentials. On a Tafel plot, once the onset potential is reached, a linear slope is well defined, where electrochemical reaction is the rate determining step.[18] As shown in Fig. 5-9, the slope values of the Tafel regions at low overpotential range for NiFeAl, NiFe_B and NiFe_P electrodes are 158, 46 and 36 mV/decade, respectively. The lower Tafel slope of NiFe_P is contributed by ultra-small nanoparticles, which increase active sites on the electrode surface and effectively accelerate electron transfer process at the electrode and electrolyte interface. By increasing the overpotential, the rate determining step evolves from electrochemical reaction to mass diffusion[18-21], with the slope gradually increasing to ~ 600 mV/dec. It can be seen, NiFe_P reaches the mass diffusion control region at a lower overpotential than that of NiFe_B. Because the higher surface roughness and wider distribution of microchannels of NiFe_P enhance the oxygen gas repelling and mass diffusion, leading to a full surface coverage earlier.

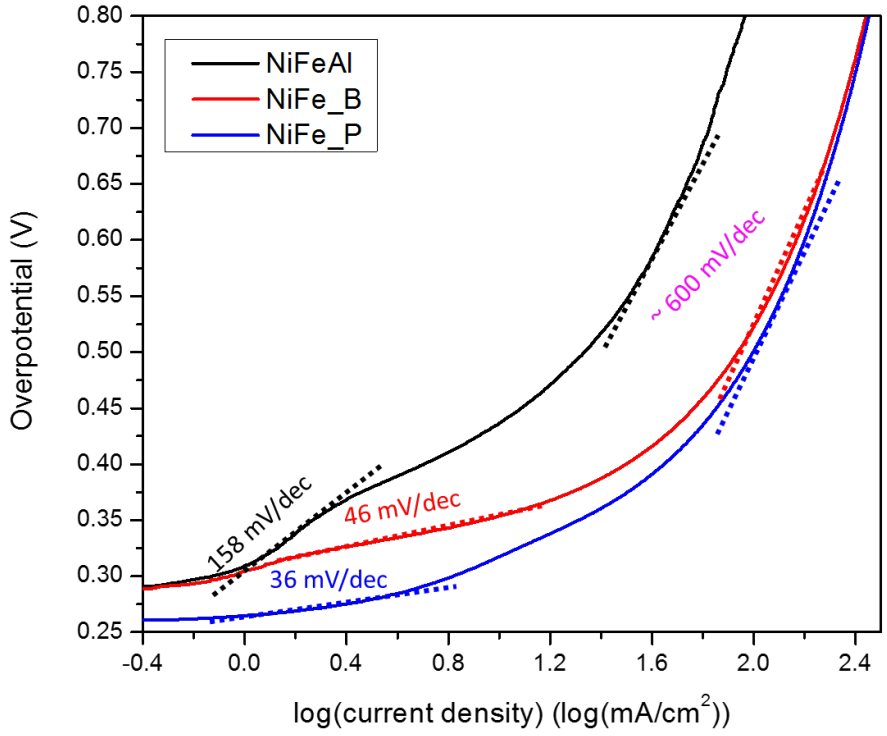

Figure 5.9 Tafel Slope of NiFeAl, NiFe_B and NiFe_P electrodes

5.3.8 Nyquist Plot of EIS

As shown in Fig. 5-10, The Nyquist plots of EIS were taken at an overpotential of 438 mV in the frequency range of 10^5 Hz to 0.1 Hz on the NiFeAl, NiFe_B and NiFe_P electrodes. The equivalent circuit is calculated using the CHI 650 C electrochemical workstation software package with the fitted results listed in Table 1. The equivalent circuit is composed of R_s - solution resistance, R_{int} – electrode/electrolyte interface resistance, R_{ct} – charge transfer resistance, CPE_1 – constant phase element for interfacial capacitance, and CPE_2 – constant phase element for double layer capacitance.[22] The intercept of the plot with the real axis (R_s) represents the overall ohmic resistance, including the bulk resistance of the material, series resistance, and contact resisitance.[23] The semicircle at high frequency range is from metal hydroxide intermediates formation and absorption process, whose diameter (R_{int}) indicates the rate of the electrode/electrolyte interfacial process.[24] It is observed, the R_{int} of NiFe_P (0.010 Ω cm^2) spectrum is smaller than that of Ni_4Fe_6_B (0.023 Ω cm^2), indicating a faster OH^- absorption and intermediates formation at the electrode/electrolyte interface. It is also noticed, the CPE_1 of NiFe_P (3.061 mF s^{n-1} cm^{-2}) is much higher than that of NiFe_B (2.041 mF s^{n-1} cm^{-2}), indicating more surface atoms on NiFe_P electrode are exposed for reaction species absorption and intermediates formation, attributed to the enlarged specific surface area from the nanoporous structure.

Since the n_1 values are close to the value of unity, the CPE_1 is close to pure capacitance. The semicircle on low frequency range describes the electron charge transfer process of OH^-/O_2 redox reaction at the electrode/electrolyte interface[24], with a diameter of R_{ct} representing the charge transfer resistance between reactant to product.[25] A smaller R_{ct} indicates a faster electron transfer. It can be seen, the R_{ct} of NiFe_P (0.490 Ω cm^2) is smaller than that of NiFe_B electrode (0.573 Ω cm^2). The CPE_2 illustrates the double layer capacitance, which doesn't contribute to electrochemical reaction kinetics [26-27]. The n_2 value of NiFe_P (0.608) is much lower than that of NiFe_B (0.802), indicating its rougher and more porous surface. It is found, due to formation of nanostructures, the overall electrocatalytic activity is apparently improved by the increased specific surface area and active sites. The nanostructure enhances the reactant absorption and intermediates formation, and accelerates the electrode/electrolyte interface electron transfer; the interconnected micro channels increase the pathways for mass transfer and facilitate the ion diffusion and gas transportation.

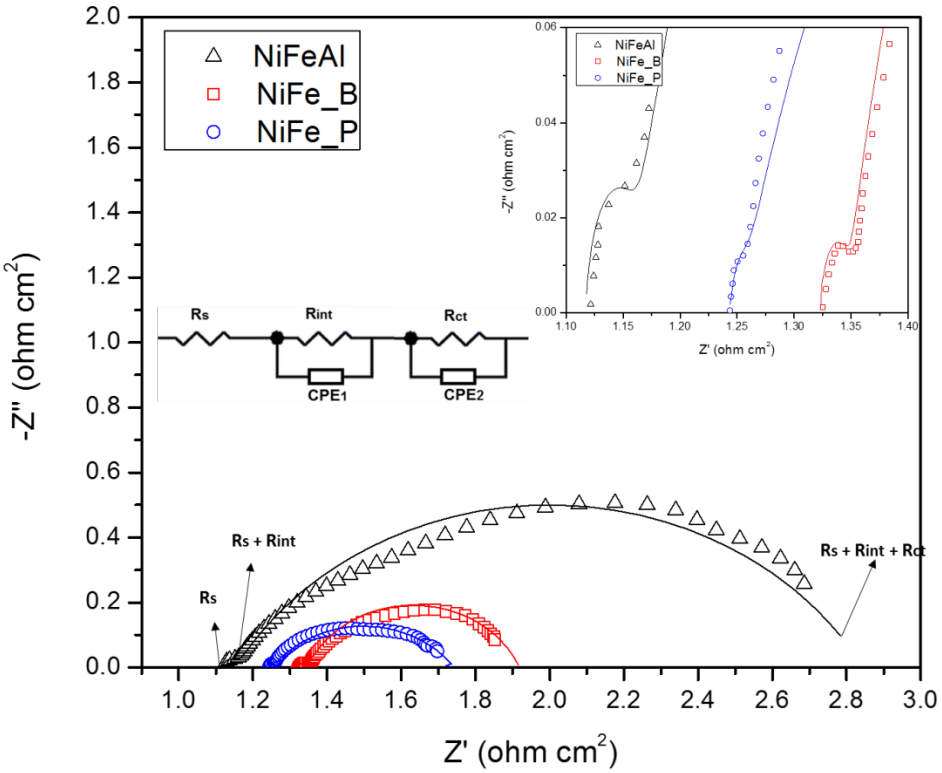

Figure 5.10 The EIS spectra of the NiFeAl, NiFe_B and NiFe_P electrodes. Symbols: experimental data; solid line: fitting data; inset: equivalent circuit and enlarged image of high frequency range

Table 5.2 Table of EIS parameters

	R_s (Ω cm^2)	R_{int} (Ω cm^2)	CPE_1 (mF s^{n-1} cm^{-2})	n_1	R_{ct} (Ω cm^2)	n_2	CPE_2 (F s^{n-1} cm^{-2})
NiFeAl	1.117	0.037	0.612	0.999	1.690	0.680	0.085
NiFe_B	1.323	0.023	2.041	0.999	0.573	0.752	0.160
NiFe_P	1.243	0.010	3.061	0.999	0.490	0.608	0.198

5.3.9 Stability Test

The stability of the nanoporous NiFe_P electrocatalyst was evaluated by chronoamperometry at a 288 mV overpotential. As shown in Fig. 5-11, it has an initial current density of 10 mA/cm^2. Although the current density experienced a slight decay in the first three hours, the current density maintains fairly constant ~ 10 mA/cm^2 to 15 hours.

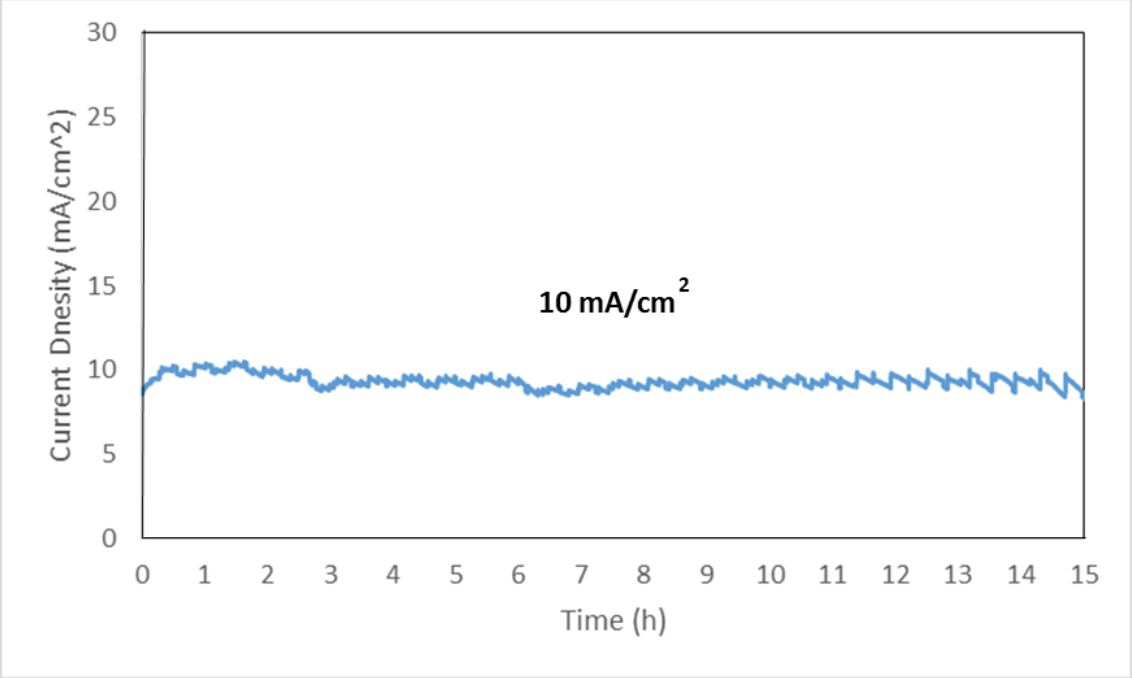

Figure 5.11 Time-dependent potential response during 15-hour chronoamperometric water-splitting reaction, at a constant DC potential of 288 mV overpotential

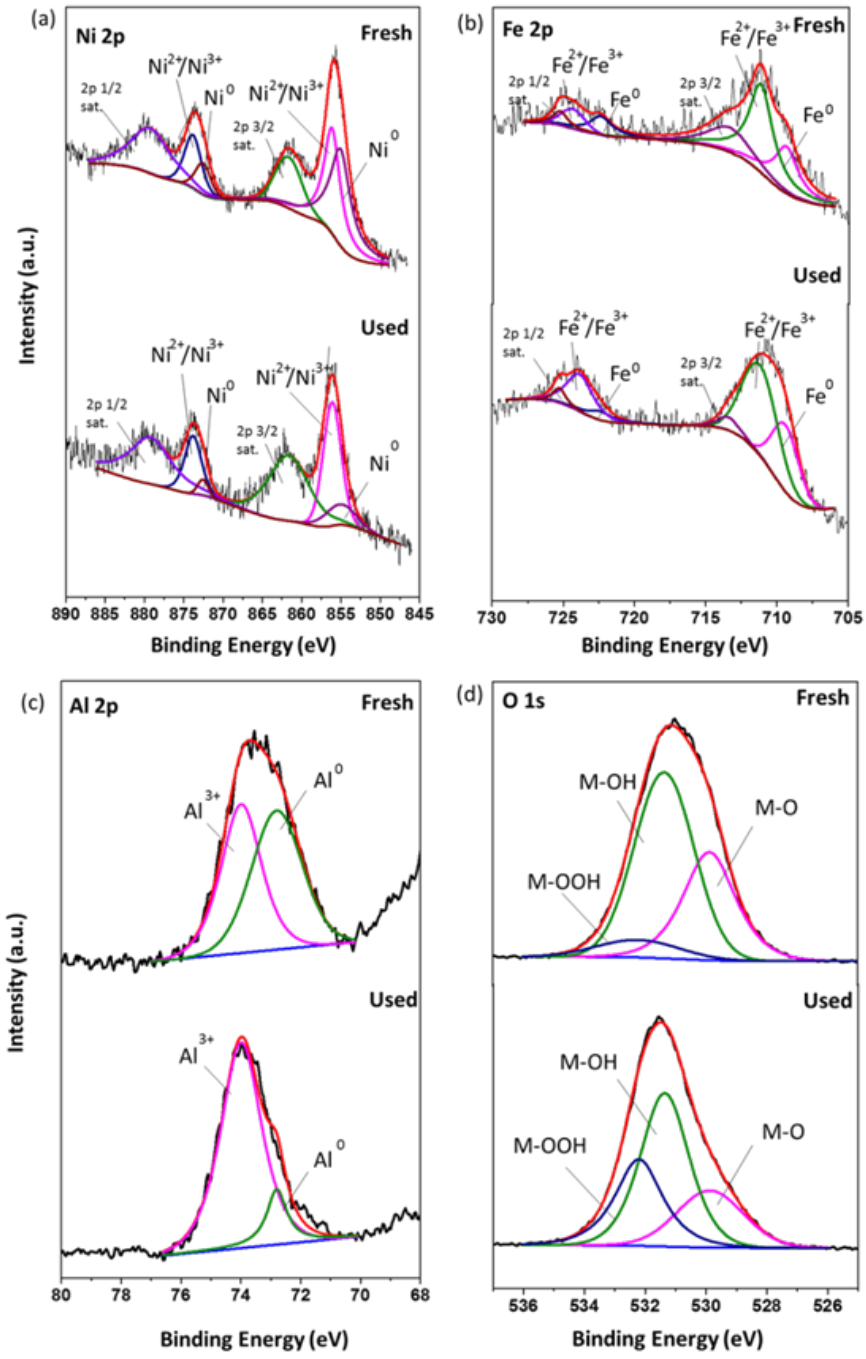

Figure 5.12 XPS core spectra of (a) Ni 2p, (b) Fe 2p, (c) Al 2p, and (d) O 1s of as-prepared fresh NiFe_P and NiFe_P after 15-hour chronoamperometric water-splitting reaction

To study the chemical compositions of as-prepared fresh NiFe_P and NiFe_P after 15-hour chronoamperometric water-splitting reaction, XPS spectra are displayed in Fig. 5-12. As displayed in Fig. 5-12 (a), the Ni 2p spectrum of fresh NiFe_P sample has two main pairs of de-convoluted peaks, which can be attributed to Ni^0 and Ni^{2+}/Ni^{3+}, respectively.[28-29] It can be seen, after 15-hour chronoamperometric water-splitting reaction, the relative intensity of Ni^{2+}/Ni^{3+} peaks to Ni^0 peaks are getting higher, indicating more Ni atoms have been oxidized/hydro-oxidized during the water-splitting process. As displayed in Fig. 5-12 (b), the Fe 2p spectrum has two main pair of de-convoluted peaks attributed to Fe^0 and Fe^{2+}/Fe^{3+}, respectively[30]. The chronoamperometric process slightly increased the ratio of Fe^{2+}/Fe^{3+} to Fe^0. As displayed in Fig. 5-12 (c), the Al atoms are mostly oxidized/hydro-oxidized to Al^{3+} with little metallic Al remaining in the alloy after 15 hours. It can be seen, the O 1s core spectra are composed of M-O (M=Ni, Fe, Al), M-OH and M-OOH bonds[31-32]; the increased ratio of M-OOH bonds and decreased ratio of M-O bonds confirm that metals are further oxidized/hydro-oxidized after the 15-hour chronoamperometric water-splitting reaction.

5.4 Conclusions

In conclusion, monolithic nanoporous Ni-Fe alloy electrocatalyst is developed by dealloying laser processed Ni-Fe-Al alloy for OER. The nanoscale pores derived from dealloying process can provide high specific surface area and more active sites for catalytic reactions. The microscale channels can provide more pathways for gas diffusion and ion transportation. In addition, as a monolithic electrode, the electron conduction can be effectively facilitated and the use of substrate and binders can be eliminated. Compared to bulk Ni-Fe electrocatalyst, the nanoporous Ni-Fe electrode, even at a less favorable Ni:Fe composition after the dealloying process, exhibits an apparently improved electrocatalytic activity and only requires 442 mV overpotential to achieve an OER current density of 100 mA/cm^2 in 1 M KOH aqueous solution, which is comparable to the performance of reported electrocatalysts to date. Overall, the laser-based manufacturing method possesses high flexibility in developing complex shaped preforms for monolithic nanoporous electrodes, which provides a new fabrication method for next generation electrode design and electrocatalyst engineering. It's well known that nanoporous structures are prone to structure degradation. Further process optimization can be performed to improve the composition and stability of monolithic nanoporous electrocatalysts.

5.5 References

1. Esswein, A. J.; McMurdo, M. J.; Ross, P. N.; Bell, A. T.; Tilley, T. D., Size-Dependent Activity of Co3O4 Nanoparticle Anodes for Alkaline Water Electrolysis. *J. Phys. Chem. C* **2009,** *113* (33), 15068-15072.

2. Zhuang, Z.; Sheng, W.; Yan, Y., Synthesis of Monodisperse Au@Co3O4 Core-Shell Nanocrystals and Their Enhanced Catalytic Activity for Oxygen Evolution Reaction. *Adv.*

Mater. (Weinheim, Ger.) **2014,** *26* (23), 3950-3955.

3. Masa, J.; Xia, W.; Sinev, I.; Zhao, A.; Sun, Z.; Gruetzke, S.; Weide, P.; Muhler, M.; Schuhmann, W., MnxOy/NC and CoxOy/NC Nanoparticles Embedded in a Nitrogen-Doped Carbon Matrix for High-Performance Bifunctional Oxygen Electrodes. *Angew. Chem., Int. Ed.* **2014,** *53* (32), 8508-8512.

4. Deng, X.; Tueysuez, H., Cobalt-Oxide-Based Materials as Water Oxidation Catalyst: Recent Progress and Challenges. *ACS Catal.* **2014,** *4* (10), 3701-3714.

5. Matthias, S.; Mueller, F.; Jamois, C.; Wehrspohn, R. B.; Goesele, U., Large-area three-dimensional structuring by electrochemical etching and lithography. *Adv. Mater. (Weinheim, Ger.)* **2004,** *16* (23-24), 2166-2170.

6. Xie, L.; Wang, K.; Du, G.; Asiri, A. M.; Sun, X., Self-standing cobalt oxide nanosheet array: An monolithic catalyst for effective hydrolysis of NaBH4 in alkaline media. *International Journal of Hydrogen Energy* **2017,** *42* (52), 30639-30645.

7. Cebollero, J. A.; Lahoz, R.; Laguna-Bercero, M. A.; Peña, J. I.; Larrea, A.; Orera, V. M., Characterization of laser-processed thin ceramic membranes for electrolyte-supported solid oxide fuel cells. *International Journal of Hydrogen Energy* **2017,** *42* (19), 13939-13948.

8. Rosen, J.; Hutchings, G. S.; Jiao, F., Ordered Mesoporous Cobalt Oxide as Highly Efficient Oxygen Evolution Catalyst. *J. Am. Chem. Soc.* **2013,** *135* (11), 4516-4521.

9. Tueysuez, H.; Hwang, Y. J.; Khan, S. B.; Asiri, A. M.; Yang, P., Mesoporous Co3O4 as an electrocatalyst for water oxidation. *Nano Res.* **2013,** *6* (1), 47-54.

10. Zhao, Y.; Xu, L.; Mai, L.; Han, C.; An, Q.; Xu, X.; Liu, X.; Zhang, Q., Hierarchical mesoporous perovskite La0.5Sr0.5CoO2.91 nanowires with ultrahigh capacity for Li-air batteries. *Proc. Natl. Acad. Sci. U. S. A.* **2012,** *109* (48), 19569-19574, S19569/1-S19569/6.

11. Xu, C.; Hou, J.; Pang, X.; Li, X.; Zhu, M.; Tang, B., Nanoporous PtCo and PtNi alloy ribbons for methanol electrooxidation. *Int. J. Hydrogen Energy* **2012,** *37* (14), 10489-10498.

12. Cui, X.; Zhang, B.; Zeng, C.; Wen, H.; Yao, H.; Guo, S., Laser Processed Ni-Fe Alloys as Electrocatalyst toward Oxygen Evolution Reaction. *Submitted to Material Research Express, Under Review* **2018**.

13. Hoang, T. T. H.; Gewirth, A. A., High Activity Oxygen Evolution Reaction Catalysts from Additive-Controlled Electrodeposited Ni and NiFe Films. *ACS Catalysis* **2016,** *6* (2), 1159-1164.

14. Lim, T.; Sung, M.; Kim, J., Oxygen Evolution Reaction at Microporous Pt Layers:

Differentiated Electrochemical Activity between Acidic and Basic Media. *Scientific Reports* **2017,** *7*, 15382.

15. Zhao, Y.; Chen, S.; Sun, B.; Su, D.; Huang, X.; Liu, H.; Yan, Y.; Sun, K.; Wang, G., Graphene-Co3O4 nanocomposite as electrocatalyst with high performance for oxygen evolution reaction. *Scientific Reports* **2015,** *5*, 7629.

16. Reier, T.; Oezaslan, M.; Strasser, P., Electrocatalytic Oxygen Evolution Reaction (OER) on Ru, Ir, and Pt Catalysts: A Comparative Study of Nanoparticles and Bulk Materials. *ACS Catalysis* **2012,** *2* (8), 1765-1772.

17. Favaro, M.; Valero-Vidal, C.; Eichhorn, J.; Toma, F. M.; Ross, P. N.; Yano, J.; Liu, Z.; Crumlin, E. J., Elucidating the alkaline oxygen evolution reaction mechanism on platinum. *J. Mater. Chem. A* **2017,** *5* (23), 11634-11643.

18. Navarro-Flores, E.; Chong, Z.; Omanovic, S., Characterization of Ni, NiMo, NiW and NiFe electroactive coatings as electrocatalysts for hydrogen evolution in an acidic medium. *Journal of Molecular Catalysis A: Chemical* **2005,** *226* (2), 179-197.

19. Fabbri, E.; Habereder, A.; Waltar, K.; Kotz, R.; Schmidt, T. J., Developments and perspectives of oxide-based catalysts for the oxygen evolution reaction. *Catal. Sci. Technol.* **2014,** *4* (11), 3800-3821.

20. Duan, J.; Chen, S.; Jaroniec, M.; Qiao, S. Z., Heteroatom-Doped Graphene-Based Materials for Energy-Relevant Electrocatalytic Processes. *ACS Catal.* **2015,** *5* (9), 5207-5234.

21. Qaseem, A.; Chen, F.; Wu, X.; Johnston, R. L., Pt-free silver nanoalloy electrocatalysts for oxygen reduction reaction in alkaline media. *Catalysis Science & Technology* **2016,** *6* (10), 3317-3340.

22. Jin, C.; Lu, F.; Cao, X.; Yang, Z.; Yang, R., Facile synthesis and excellent electrochemical properties of NiCo2O4 spinel nanowire arrays as a bifunctional catalyst for the oxygen reduction and evolution reaction. *Journal of Materials Chemistry A* **2013,** *1* (39), 12170-12177.

23. Cui, X.; Xie, Z.; Wang, Y., Novel CoS2 embedded carbon nanocages by direct sulfurizing metal-organic frameworks for dye-sensitized solar cells. *Nanoscale* **2016,** *8* (23), 11984-11992.

24. Franco, D. V.; Da Silva, L. M.; Jardim, W. F.; Boodts, J. F. C., Influence of the electrolyte composition on the kinetics of the oxygen evolution reaction and ozone production processes. *J. Braz. Chem. Soc.* **2006,** *17* (4), 746-757.

25. Xu, K.; Loh, A.; Wang, B.; Li, X., Enhancement of Oxygen Transfer by Design Nickel Foam Electrode for Zinc−Air Battery. *Journal of The Electrochemical Society* **2018,**

165 (5), A809-A818.

26. Kotz, R.; Carlen, M., Principles and applications of electrochemical capacitors. *Electrochim. Acta* **2000,** *45* (15-16), 2483-2498.

27. Conway, B. E.; Pell, W. G., Double-layer and pseudocapacitance types of electrochemical capacitors and their applications to the development of hybrid devices. *J. Solid State Electrochem.* **2003,** *7* (9), 637-644.

28. Zhang, Q.; Chen, N.; Hua, Z.; Pang, S., DOS investigation of 3d transition metals by ionization loss spectroscopy. *Vacuum* **1992,** *43* (11), 1137-9.

29. St, U.; Scharfschwerdt, C.; Neumann, M.; Illing, G.; Freund, H. J., The influence of defects on the Ni 2p and O 1s XPS of NiO. *Journal of Physics: Condensed Matter* **1992,** *4* (40), 7973.

30. Kaurila, T.; Saeisae, L.; Vaeyrynen, J., Resonant photoemission from iron films on copper. *J. Phys.: Condens. Matter* **1994,** *6* (27), 5053-60.

31. Liang, Y.; Sherwood, P. M. A.; Paul, D. K., Valence and core photoemission of the films formed electrochemically on nickel in sulfuric acid. *Journal of the Chemical Society, Faraday Transactions* **1994,** *90* (9), 1271-1278.

32. N. Mansour, A.; Melendres, C., *Characterization of Electrochemically Prepared γ-NiOOH by XPS*. 1994; Vol. 3, p 271-278.

6. ELECTROCATALYTIC ACTIVITY OF HIGH-ENTROPY ALLOY TOWARD OXYGEN EVOLUTION REACTION

6.1 Overview

Recently, many low-cost materials have been explored to replace noble metals for OER.[1] Among them, first row transition metals, such as Ni, Fe, Co, Cu, Mn, are especially appealing, due to their special electronic structures and the abundance on earth. [2] High-entropy alloys (HEAs), a new type of alloys, constructed of five or more metallic elements at equal or near-equal molecular ratios, are emerging into an attractive category of functional metallic materials in the past decade. [3] Due to the varied atomic radius and geometrical configurations of different elements, the crystal lattices of HEAs can be finely tuned over a certain range, and the crystal lattices of HEAs can be severely distorted with significant residual strain remaining. [4] Such a high level of crystal imperfection could effectively increase the amount of active catalytic sites. [5] Moreover, due to the highly complex combination of transition metals with different electron configurations, the d-band vacancy number of HEA can be altered to tune its binding strength toward reaction species. [6] Because few studies have been conducted on the catalytic performance of HEAs, this chapter examines the hypothesis that by tuning the HEAs compositions, an improved OER performance would be achieved.

6.2 HEA Design for Improved OER Performance

The binding strength of the reaction species toward the surfaces of an electrocatalyst determines the activity of the electrocatalyst. For selected metallic catalysts, the volcano plot of catalytic activity vs. the absorption energy of atomic oxygen [7] reveals that a moderate binding strength leads to a high catalytic activity. For OER applications, a too weak binding between the reaction species and the electrocatalyst surface would result in difficult stabilization of intermediates, while a too strong binding would hinder the release of O_2. The binding strength is affected by several factors. Firstly, it's affected by the electronic structures of the electrocatalyst. The existence of d-band vacancy in transition metals enables the formation of intermediate species to lower the activation energy, and a moderate d-vacancy number is preferable for OER applications.[8] Secondly, in the heterogeneous reactions, the lattice spacing of the electrocatalyst and the reaction species should match. In other words, too large an interatomic distance would impede diatomic reactant adsorption and the bond formation between oxygen atoms, while too closely packed atoms would cause strong repulsions between intermediates and inhibit product formation.[8] Thirdly, a certain degree of intrinsic structural defects could contribute to an improved catalytic performance.[9] Therefore, compared to the traditional metals and alloys, a well-designed HEA with proper compositions is highly possible to combine the merits of each constitute element and meet the above criteria for improved OER performance.

Based on the criterion No.1, two HEAs were selected to demonstrate that HEA compositions would impact the OER performance. The first HEA would have a non-

transition metal element and the second HEA would be formed by pure transition metals. In this regard, the classical FeCoNiCrAl HEA, with non-transition metal element Al, was chosen as the starting point to investigate how HEAs could be designed to have an improved OER performance. For FeCoNiCrAl HEA, Fe, Co, Ni and Cr are all on the left side of the peak on the volcano plot[7], indicating their over-strong binding strength toward the reactant. Also, being a main group element, Al is a strong electron donor which can bind strongly to electron accepters to form stable compounds. All these may aggravate the difficulty of O_2 formation and release.

Based on the criterion No.2, the bond length of M-O (M=metal) for Fe, Co, Ni, Cr and Al is 2.08 Å, 2.13 Å, 2.09 Å, 2.02 Å and 1.89 Å respectively[10-12] with an average of 2.04 Å. Considering the symmetric trapezoid configuration of OER diatomic reaction in the alkaline environment[13], the calculated optimal lattice spacing to facilitate O_2 formation for a perfectelectrocatalyst is ~2.50 Å. However, from the XRD testing results, to be shown in later section, FeCoNiCrAl mainly composes a FCC phase with $a = 3.3183 \pm 0.0013$ Å, demonstrating the lattice spacing for the most densely packed plane (111) to be 2.35 Å. Therefore, tuning the baseline FeCoNiCrAl HEA compositions with elements which can slightly decrease the d-vacancy number and enlarge the lattice spacing is expected to improve the activity of HEA electrocatalyst.

To design an HEA with more favorable features as an electrocatalyst toward OER, Co and Al were replaced with Mn and Cu. Because Cu has fully filled d orbitals, the electrons in Cu can transit to the d-band of other transition metals to reduce the d-vacancy number and the overall binding strength can be reduced. In addition, Mn (r=161 pm) is among the few low-cost elements with an apparent larger radius than that of Al (r =118 pm) and Co (r=152 pm) and has an acceptable affinity toward O atom. With more matched d-vacancy number and lattice spacing toward OER, the FeNiMnCrCu HEA is expected to have a better performance than the baseline FeCoNiCrAl HEA.

6.3 Experimental

6.3.1 Synthesis of High-entropy Alloys

To synthesize the FeNiMnCrCu HEA, commercial iron (powder (fine), Sigma Aldrich, >99%, metals basis), nickel (3-7 micron, Alfa Aesar, >99.9%, metals basis), manganese (325 mesh, Alfa Aesar, 99.95%, metals basis), chromium (325 mesh, Alfa Aesar, 99%, metals basis), and copper (~170 + 400 mesh, Alfa Aesar, 99.5%, metals basis) powders with the ratio of 1:1:1:1:1, were well mixed inside a polystyrene ball mill jar by a high-speed ball milling machine for 2 mins. Then the mixed powders were pressed in a dry pressing die with a diameter of 12.7 mm. Next, the as-prepared sample was placed into the chamber of an arc melting system (model Edmund Bühler/MAM-1). During the melting process, the ingots were inverted and re-melted for four times to ensure homogeneity. The FeCoNiCrAl HEA was prepared the same way by using equivalent mole amount of iron, cobalt (325 mesh, Alfa Aesar, 99.5%, metals basis), nickel, chromium, and aluminum (325 mesh, Alfa Aesar, 99.5%, metals basis).

6.3.2 Materials Characterizations and Electrochemical measurements

The HEA phase diagrams are calculated by ThermoCalc^{TM} software. The crystal structures of the samples were characterized by an X-ray diffraction (XRD) using a Panalytical Empyrean multipurpose diffractometer equipped with PreFIX modules with Cu Kα radiation. To prepare the HEA electrode, a copper wire was attached to each of the arc-melted ingots by tin soldering. Then the ingots with the connecting wire were mounted into an epoxy resin (SamplKwick fast cure acrylic resin, Buehler). At last, for each sample, a flat surface was exposed by cutting through the ingot using a low-speed saw. The electrochemical measurements were carried out in a three-electrode system using a CHI 650C electrochemical workstation. The HEAs served as the working electrode in a 1 M NaOH aqueous electrolyte, with Pt wire and saturated calomel electrode (SCE) as counter electrode and reference electrode, respectively. Linear sweep voltammetry (LSV) and Tafel measurement were carried out at a scan rate of 5 mV/s in the potential range of 0 to 1V vs. SCE. Commercial Pt was tested the same way for comparison. Electrochemical impedance spectra (EIS) measurements were carried out at 438 mV overpotential in the frequency range from 105 Hz to 0.01 Hz. To study the stability of the HEAs, the chronoamperometry was carried out at 438 mV overpotential for 10 hours.

6.4 Results and Discussion

6.4.1 Quinary Phase Diagrams

CALPHAD method was adopted to calculate the phase diagram and the phase composition during an equilibrium solidification process. For the baseline quinary HEA system $FeCoNiCrAl_x$, with increasing of the Al content, the phase structure of the system gradually changes from a single FCC into a single BCC structure. This predicted has been proved experimentally by other researchers [14]. Figure 6-1 (a) shows the pseudobinary phase diagram of FeCoNiCr-Al_x system calculated using ThermoCalc software. While keeping the molecular ratio of FeCoNiCr constant, the phase structure change, along with the (FeCoNiCr) and Al ratio, was presented as an ordinary binary phase diagram. Using the phase diagram, the equimolar $FeCoNiCrAl_{x=1}$ can be seen consisting of both FCC and BCC structures, with FCC phase as the primary phase. Under the sample preparation condition with a rapid cooling rate, equilibrium phase transformation at low temperatures is usually inhibited, leading to the precipitation of high temperature phases.

Figure 6-1(b) shows the equilibrium solidification process of FeNiMnCrCu, starting from the liquidus temperature at ~1458K. Both FCC and BCC phases start to form almost simultaneously, with a secondary FCC phase forms at ~1297K, which is almost the solidus temperature (1295K). Considering the rapid cooling rate of the sample made in the water-cooled copper hearth of the arc melting furnace, the diffusion introduced phase transformation at low temperatures could be neglected. Thus the phase structures of FeNiMnCrCu should consist mainly of double FCC phases and a BCC phase. It is also interesting to see, the intrinsic residual strain of FeNiMnCrCu is reported to be

3.18%[15] that is higher than the FeCoNiCrAl case value of 2.96% [15]. Therefore, the FeNiMnCrCu HEA is in a more non-equilibrium state possessing higher potential energy that is expected to activate reactions at a lower applied potential.[16]

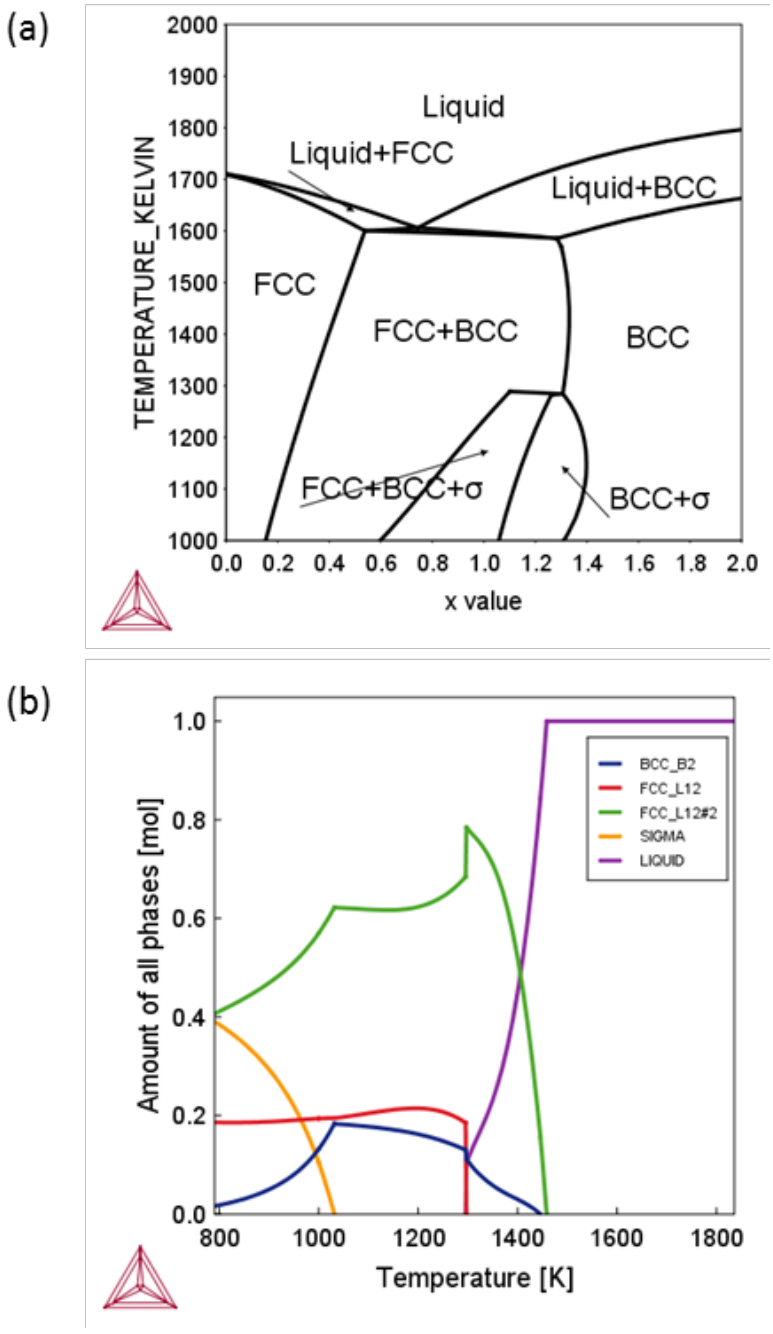

Figure 6.1(a) pseudobinary phase diagram of FeCoNiCr-Alx (b) phase composition during equilibrium solidification of FeNiMnCrCu

6.4.2 Crystal Structure by XRD

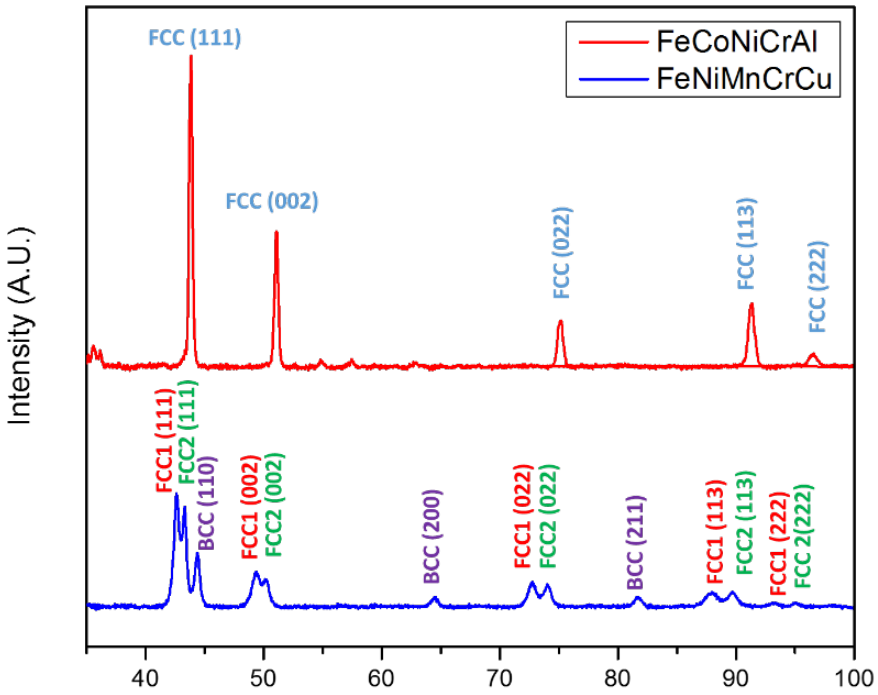

Figure 6.2 XRD spectra of FeCoNiCrAl and FeNiMnCrCu

The XRD patterns are presented in Fig. 6-2. The XRD spectrum of FeCoNiCrAl indicates a complete dissolution of all five elements and the formation of a single FCC phase. This differs from the equilibrium prediction shown in Fig.6-1a. Based on other researchers, FCC is the major structure of the FeCoNiCrAl HEA annealed at a temperature higher than 800 °C and then free cooled to room temperature[17]. Under the arc melting process, the rapid cooling rate inhibits phase transformation to BCC and leads to the domination of the FCC phase. Peaks at 2θ = 43.85°, 51.08°, 75.09° 91.34° and 96.59° corresponding to planes of (111), (200), (220), (311) and (222) of the FCC can be observed. The lattice parameter is calculated to be a = 3.3183 ± 0.0013 Å.

For the FeNiMnCrCu HEA, it has a more complicated structure and is composed of two FCC and one BCC phases. The first FCC phase has peaks at 2θ = 42.59°, 49.40°, 72.78°, 87.89° and 93.34° corresponding to planes of (111), (200), (220), (311) and (222). The lattice parameter is calculated to be a = 3.4160 ± 0.0055 Å. The second FCC phase has peaks at 2θ = 43.43°, 50.24°, 74.05°, 89.77° and 95.02° corresponding to planes of (111), (200), (220), (311) and (222). The lattice parameter is calculated to be a = 3.3601 ± 0.0076 Å. The BCC phase has peaks at 2θ = 44.38°, 64.51° and 81.81° corresponding to planes of (110), (200) and (211). The lattice parameter is calculated to be a = 2.678 ± 0.0020 Å. Therefore, the lattice constants of the FCC phases in the FeNiMnCrCu are larger than that of FeCoNiCrAl. This is due to the replacement of Al (r =118 pm) and Co (r=152 pm) by Cu (145 pm) and Mn (161 pm), whose radius are relatively larger, causing the extension of lattice. In addition, due to the higher atomic

packing density of FCC (74%) than that of BCC (68%), the replacing of Al and Co with Cu and Mn leads to a mixture of FCC and BCC phases and causes larger residual strains. This gives a higher lattice distortion energy. Therefore, to release the distortion energy, some of the FCC phase splits to two different FCC phases, with the rest transfers to a more stable BCC phase.[18] It can be seen the lattice spacing of {111} planes in FCC1 and FCC2 phases of FeNiMnCrCu HEA are 2.38 Å and 2.42 Å respectively, which are closer to the optimal lattice spacing (2.50 Å) than that of FeCoNiCrAl HEA (2.35 Å).

6.4.3 Catalytic Performance Study by LSV

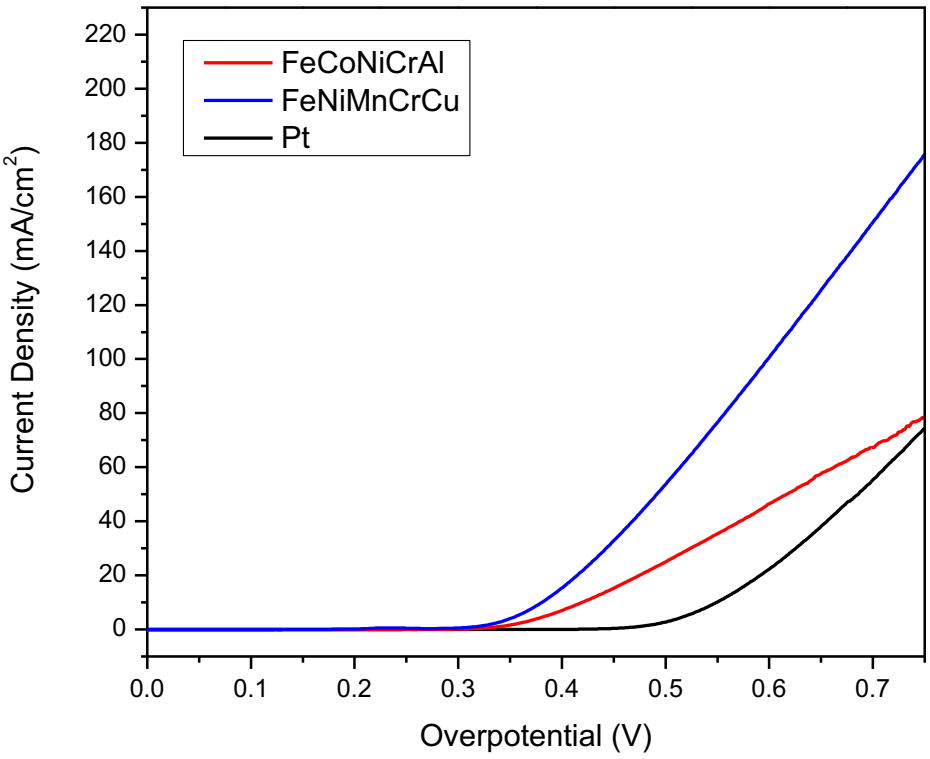

Figure 6.3 The OER polarization curves of FeCoNiCrAl and FeNiMnCrCu electrodes

To evaluate the electrocatalytic performance of FeCoNiCrAl and FeNiMnCrCu HEAs, the LSV results are shown in Fig. 6-3. It is seen the onset overpotentials for FeCoNiCrAl and FeNiMnCrCu HEAs are 317 mV and 342 mV, respectively, which are significantly lower than that of the Pt electrode (471 mV), indicating a lower activation energy needed by the HEA electrocatalysts to initial the OER redox reaction.[19] The FeCoNiCrAl electrode exhibits a relatively lower activity with slowly increased current density and is not able to reach an OER current density of 100 mA/cm^2 in the tested voltage range. It is observed, the FeNiMnCrCu electrode possesses a better electrocatalytic activity with the current density increasing rapidly after the onset potential and reaches 40 mA/cm^2 and 100 mA/cm^2 OER current density at 466 mV and 599 mV overpotential, respectively. For comparison, FeCoNiCrAl and Pt electrodes require 580 mV and 656 mV to achieve 40 mA/cm^2, respectively. It can

be seen that HEAs have great potential in serving as OER electrocatalyst due to their much improved performance than the Pt electrocatalyst. In addition, as expected, the performance of the FeNiMnCrCu HEA electrocatalyst is significantly higher than that of FeCoNiCrAl, due to its higher residual strain, better matched d-vacancy number and lattice spacing toward OER.

6.4.4 Mechanism Study by Tafel Slope

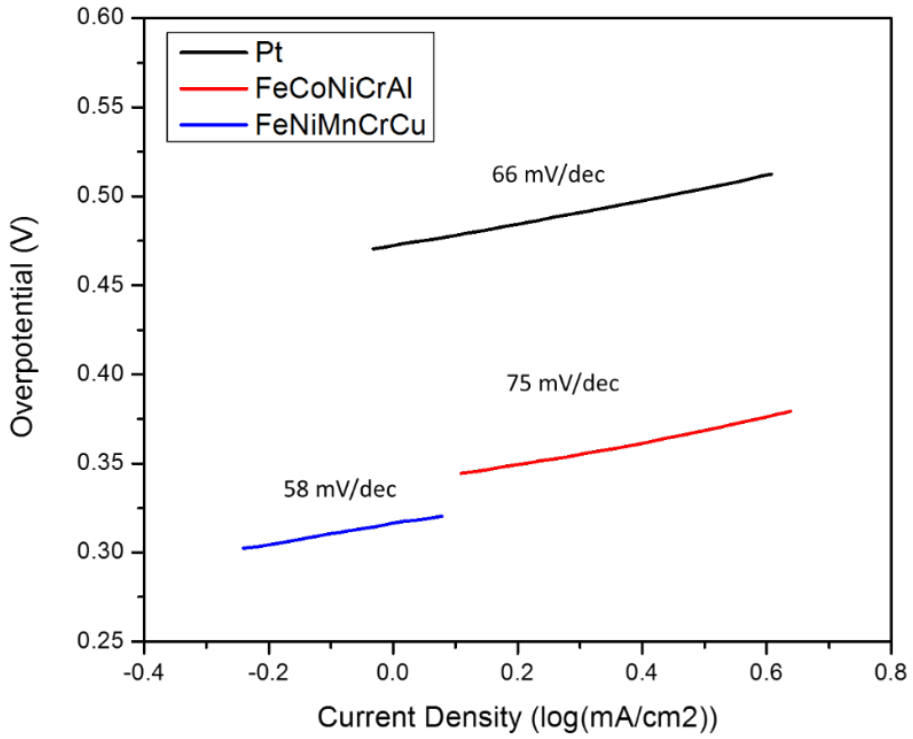

Figure 6.4 Tafel slopes of FeCoNiCrAl and FeNiMnCrCu electrodes

To study the kinetic of the OER with HEA electrocatalysts, the Tafel plots are provided in Fig. 6-4. In the Tafel plots, a smaller slope indicates a more rapid electron transfer at the electrode and electrolyte interface at the applied potentials, which suggesting a better catalytic activity of the electrocatalyst.[20] Tafel slopes for FeCoNiCrAl, FeNiMnCrCu and Pt electrodes are 75 mV/decade, 58 mV/decade and 66 mV/decade, respectively. It can be seen, the Tafel slope of FeNiMnCrCu is smaller than Pt.

6.4.5 Electrochemical Characteristics by EIS

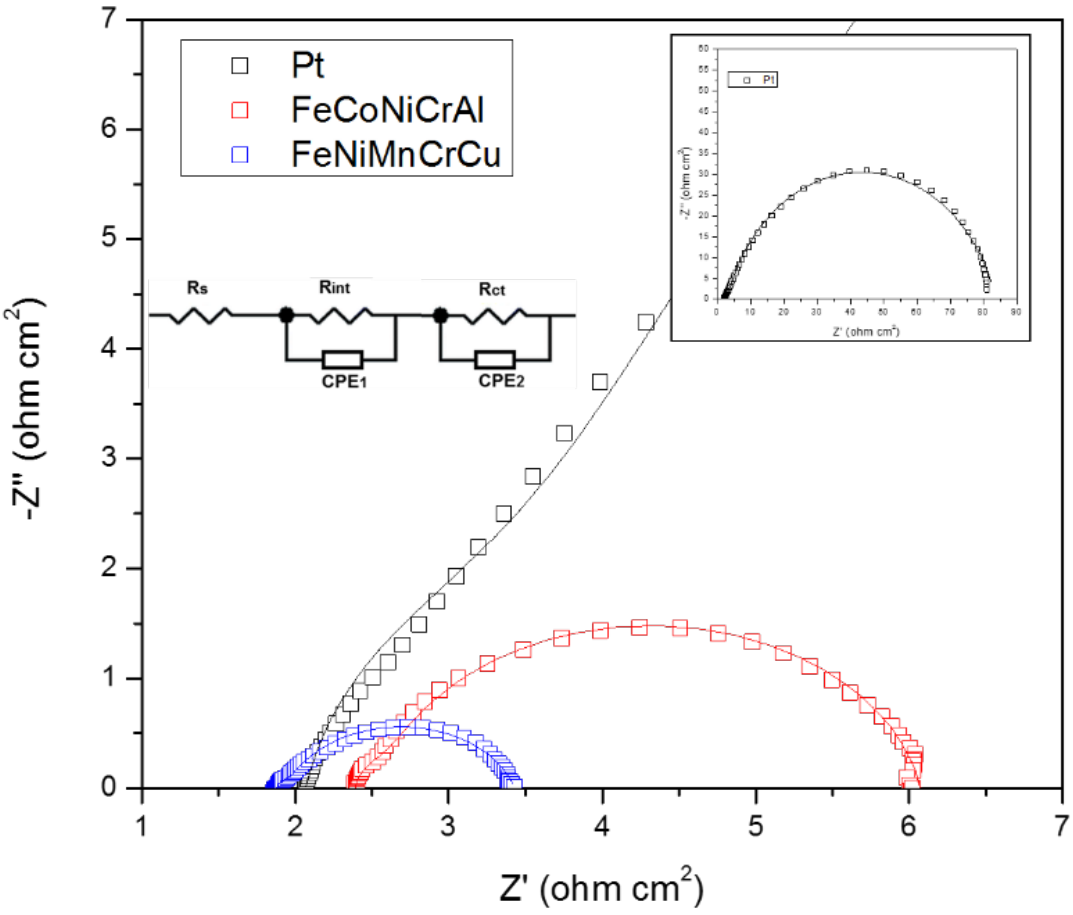

Figure 6.5 The EIS spectra of FeCoNiCrAl and FeNiMnCrCu electrodes; symbols: experimental data; solid lines: simulated data; inset: equivalent circuit

The electrochemical process is further studied by EIS at an overpotential of 438 mV in the frequency range of 10^5 Hz to 0.01 Hz as displayed in Fig. 6-5. The equivalent circuit elements are fitted by CHI 650 C electrochemical workstation software package with the results listed in Table 1. The intercept of the plot with the horizontal axis at high frequency (R_s) is the overall series resistance, including material bulk resistance and contact resisitance.[21-22] The first semicircle with a diameter of R_{int} is due to the metal hydroxide intermediates formation.[23] It is noticed, the R_{int} of FeNiMnCrCu (0.065 Ω cm^2) is apparently lower than that of FeCoNiCrAl (0.177 Ω cm^2), demonstrating a more facilitated OH^- absorption and intermediate formation at the electrode and electrolyte interface, which could effectively lower down the activation energy of the electrochemical reaction. It is also noticed, the CPE_1 of FeNiMnCrCu (1.393 mF s^{n-1} cm^{-2}) is larger than that of FeCoNiCrAl (0.650 mF s^{n-1} cm^{-2}), indicating more atoms on FeNiMnCrCu surface are involved in reaction species absorption, attributed to its more distorted crystal structure. The second semicircle describes the electron charge transportation process of the OER redox reaction, with a diameter of R_{ct} representing

the charge transfer resistance.[23] It can be seen, the R_{ct} of FeNiMnCrCu (1.482 Ω cm^2) is much smaller than that of FeCoNiCrAl electrode (3.505 Ω cm^2), indicating a faster electron transfer rate from reactant to product. As it is observed, the superior electrochemical characteristics of FeNiMnCrCu is the result of its optimized binding strength toward reaction species. A better matched d-vacancy number effectively accelerates electron transfers and the matched lattice spacing facilitates the reactant absorption and product desorption. And the high residual strain contributes to a higher potential energy that can activate OER at a lower overpotential.

6.4.6 Stability Study by chronoamperometry

The stability of the FeNiMnCrCu HEA electrocatalyst was evaluated by the chronoamperometry at a potential of 438 mV overpotential for 10 hours. The FeNiMnCrCu HEA displays an initial current density of ~ 26 mA/cm^2 and maintains this performance without significant changes for 10 hours, which indicates a good electrochemical reversibility in the extensive OER durability testing.

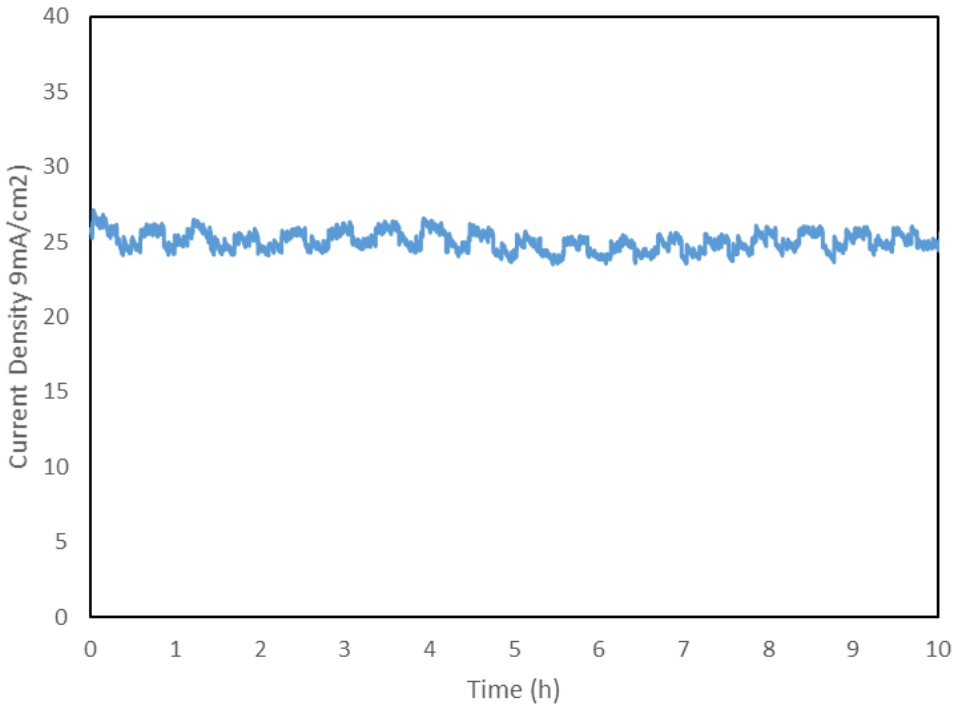

Figure 6.6 Time-dependent potential response during 10 hour chronoamperometric water-splitting of FeNiMnCrCu electrodes

Table 6.1 EIS parameters

Sample	R_s (Ω cm^2)	R_{int} (Ω cm^2)	CPE_1 (mF s^{n-1} cm^{-2})	n_1	R_{ct} (Ω cm^2)	CPE_2 (mF s^{n-1} cm^{-2})	n_2
FeCoNiCrAl	2.393	0.177	0.650	0.999	3.505	1.764	0.891
FeNiMnCrC	1.882	0.065	1.393	0.999	1.482	9.516	0.820
Pt	2.065	0.995	0.295	0.999	80.627	0.865	0.825

6.4.7 Discussions

It can be seen, compared to traditional metals and alloys, a well-designed HEA can combine the merits of each constitute element and become an efficient electrocatalyst toward OER. Firstly, since the atomic structure in HEAs is highly complex with random occupancies of elements in the lattice, the crystal structure of a HEA can be highly distorted with non-negligible residual strain. As a result, the atoms are in a thermodynamically metastable state possessing higher potential energy and more catalytic active sites. It is noticed, the lattice distortion in FeNiMnCrCu is more severe that leads to its higher catalytic activity than FeCoNiCrAl. Secondly, due to combination of different elements, the atomic lattice spacing and electronic configuration can be tuned to match better with OER.

6.5 Conclusions

Due to the unique crystal structures with severe lattice distortions, HEA based electrocatalysts may possess attractive electrocatalytic properties. In this chapter, based on a set of oxygen evolution reaction (OER) criteria, two transition metal based HEAs, namely FeNiMnCrCu and FeCoNiCrAl, are selected to demonstrate that the compositions of HEAs could be tuned to improve the OER performance. Both FeNiMnCrCu and FeCoNiCrAl samples are prepared and tested. Their crystal structures and electrocatalytic performance are examined. Owing to the replacement of Al and Co by Cu and Mn, the d-vacancy number and lattice spacing for FeNiMnCrCu are more suitable for improved OER performances. In comparison to the baseline FeCoNiCrAl and the platinum, FeNiMnCrCu needs less activation energy to initial the OER reactions and its current density increases more rapidly with potential than that of FeCoNiCrAl and platinum. As predicted, FeNiMnCrCu exhibits a good activity toward OER, which demonstrates the potential of using finely tuned HEAs for electrocatalytic applications.

6.6 References

1. Faber, M. S.; Jin, S., Earth-abundant inorganic electrocatalysts and their nanostructures for energy conversion applications. *Energy Environ. Sci.* **2014,** *7* (11), 3519-3542.

2. Fei, L.; Min, Z.; Yuxue, Z.; Xianghua, Z., First□Row Transition Metal Based Catalysts for the Oxygen Evolution Reaction under Alkaline Conditions: Basic Principles and Recent Advances. *Small* **2017,** *13* (45), 1701931.

3. Miracle, D. B.; Senkov, O. N., A critical review of high entropy alloys and related concepts. *Acta Materialia* **2017,** *122*, 448-511.

4. Wang, Z.; Qiu, W.; Yang, Y.; Liu, C. T., Atomic-size and lattice-distortion effects in newly developed high-entropy alloys with multiple principal elements. *Intermetallics* **2015,** *64*, 63-69.

5. Bak, T.; Nowotny, J.; Sucher, N. J.; Wachsman, E., Effect of Crystal Imperfections on Reactivity and Photoreactivity of TiO2 (Rutile) with Oxygen, Water, and Bacteria. *The Journal of Physical Chemistry C* **2011,** *115* (32), 15711-15738.

6. Lv, Z. Y.; Liu, X. J.; Jia, B.; Wang, H.; Wu, Y.; Lu, Z. P., Development of a novel high-entropy alloy with eminent efficiency of degrading azo dye solutions. *Scientific Reports* **2016,** *6*, 34213.

7. Nørskov, J. K.; Rossmeisl, J.; Logadottir, A.; Lindqvist, L.; Kitchin, J. R.; Bligaard, T.; Jónsson, H., Origin of the Overpotential for Oxygen Reduction at a Fuel-Cell Cathode. *The Journal of Physical Chemistry B* **2004,** *108* (46), 17886-17892.

8. Thomas, J. M.; Thomas, J. W.; Editors, *Principles and Practice of Heterogeneous Catalysis*. VCH: 1996; p 400 pp.

9. Cui, X.; Xu, W.; Xie, Z.; Dorman, J. A.; Gutierrez-Wing, M. T.; Wang, Y., Effect of dopant concentration on visible light driven photocatalytic activity of Sn1-xAgxS2. *Dalton Transactions* **2016,** *45* (41), 16290-16297.

10. D., B. I.; D., S. R., Empirical bond□strength–bond□length curves for oxides. *Acta Crystallographica Section A* **1973,** *29* (3), 266-282.

11. Mejias, J. A.; Staemmler, V.; Freund, H. J., Electronic states of the Cr 2 O 3 (0001) surface from ab initio embedded cluster calculations. *Journal of Physics: Condensed Matter* **1999,** *11* (40), 7881.

12. Caputi, L. S.; Jiang, S. L.; Amoddeo, A.; Tucci, R., Oxygen-nickel bond length in Ni(111)-O determined by electron-energy-loss fine-structure spectroscopy. *Physical Review B* **1990,** *41* (12), 8513-8515.

13. Cui, X.; Zhang, B.; Zeng, C.; Wen, H.; Yao, H.; Guo, S., Laser Processed Ni-Fe

Alloys as Electrocatalyst toward Oxygen Evolution Reaction. *Submitted to Material Research Express, Under Review* **2018**.

14. Chou, H.-P.; Chang, Y.-S.; Chen, S.-K.; Yeh, J.-W., Microstructure, thermophysical and electrical properties in AlxCoCrFeNi ($0 \leq x \leq 2$) high-entropy alloys. *Materials Science and Engineering: B* **2009,** *163* (3), 184-189.

15. Ye, Y. F.; Liu, C. T.; Yang, Y., A geometric model for intrinsic residual strain and phase stability in high entropy alloys. *Acta Materialia* **2015,** *94*, 152-161.

16. Egami, T., Atomic level stresses. *Progress in Materials Science* **2011,** *56* (6), 637-653.

17. Ji, W.; Fu, Z.; Wang, W.; Wang, H.; Zhang, J.; Wang, Y.; Zhang, F., Mechanical alloying synthesis and spark plasma sintering consolidation of CoCrFeNiAl high-entropy alloy. *Journal of Alloys and Compounds* **2014,** *589*, 61-66.

18. Zhang, K. B.; Fu, Z. Y.; Zhang, J. Y.; Wang, W. M.; Wang, H.; Wang, Y. C.; Zhang, Q. J.; Shi, J., Microstructure and mechanical properties of CoCrFeNiTiAlx high-entropy alloys. *Materials Science and Engineering: A* **2009,** *508* (1), 214-219.

19. Zhou, T.; Cao, Z.; Zhang, P.; Ma, H.; Gao, Z.; Wang, H.; Lu, Y.; He, J.; Zhao, Y., Transition metal ions regulated oxygen evolution reaction performance of Ni-based hydroxides hierarchical nanoarrays. *Scientific Reports* **2017,** *7*, 46154.

20. Fabbri, E.; Habereder, A.; Waltar, K.; Kotz, R.; Schmidt, T. J., Developments and perspectives of oxide-based catalysts for the oxygen evolution reaction. *Catal. Sci. Technol.* **2014,** *4* (11), 3800-3821.

21. Cui, X.; Xu, W.; Xie, Z.; Wang, Y., High-performance dye-sensitized solar cells based on Ag-doped SnS2 counter electrodes. *J. Mater. Chem. A* **2016,** *4* (5), 1908-1914.

22. Cui, X.; Xie, Z.; Wang, Y., Novel CoS2 embedded carbon nanocages by direct sulfurizing metal-organic frameworks for dye-sensitized solar cells. *Nanoscale* **2016,** *8* (23), 11984-11992.

23. Franco, D. V.; Da Silva, L. M.; Jardim, W. F.; Boodts, J. F. C., Influence of the electrolyte composition on the kinetics of the oxygen evolution reaction and ozone production processes. *J. Braz. Chem. Soc.* **2006,** *17* (4), 746-757.

7. CONCLUSIONS AND FUTURE WORKS

7.1 Conclusions

In this dissertation, laser-based manufacturing was applied to develop NiFe-based alloys, with focuses on studying their electrochemical characteristics toward oxygen evolution reaction in the water electrocatalysis process.

Firstly, a one-step laser-based manufacturing method to prepare a thin layer of NiFe electrodes with varied Ni to Fe ratios as the electrocatalyst to replace high-cost noble metal based material for oxygen evolution reaction is developed. The alloying of Ni-Fe will allow electrons shift from Ni to Fe, causing the increase of d-vacancy of Ni, resulting in a catalyst matching better to the reaction electron transfer coordination without affect the Fermi level of Ni. The formation of ultra-small secondary and ternary phase grains due to the rapid AM solidification process can effectively increase the ratio of active sites on the crystal surface, increase the average lattice spacing to match better with the species involve in OER reaction. Remarkably, the laser-based manufactured Ni_6Fe_4 alloys exhibit an excellent activity of an OER current density of 100 mA/cm^2 at 464 mV overpotential in 1 M KOH aqueous solution, which is among the best-performance OER electrocatalyst reported to date, and maintain a stable performance for at least 18 hours. Such an excellent OER catalytic performance is attributed to the synergic effect from both Ni and Fe content, resulting in a material with superior catalytic activity and durability. It can be seen, synthesizing electrocatalyst by laser-based manufacturing doesn't require a tedious process to receive desired material composition nor a careful control of supporting platform/binder properties. Thus it enables a higher efficiency and flexibility for novel 3D electrocatalyst/electrode development.

Secondly, the laser processed Ni-Fe alloys are prepared by varied laser scanning speeds. Their microstructures and morphologies are examined by XRD and SEM. Their electrocatalytic performance toward OER electrocatalyst is studied. In addition Ni-Fe alloys prepared by arc melting and spark plasma sintering are also prepared for comparison. It is found temperature gradient is a decisive factor to the microstructure of a laser-processed alloy. The laser power density significantly impact the phase composition and surface morphology of the electrocatalyst. It can be seen, the arc melted sample displayed much higher activity than spark plasma sintered samples due to its more favorable composition toward oxygen evolution reaction. It is also observed, the laser-processed samples displayed apparent higher electrocatalytic activity toward the oxygen evolution reaction, due to its rougher surface as a result of the special thermal cycle during laser processing. Herein, laser-processing may provide new insight on develop novel electrocatalyst by controlling the microstructures.

Thirdly, monolithic nanoporous NiFe electrocatalyst is developed by dealloying Ni-Fe-Al prepared by laser-based manufacturing for the first time. The nanoscale pores derived from dealloying process provide high surface areas and more active sites for

catalytic reactions. At the same time the microscale pores provide sufficient channels for gas diffusion to accelerate the mass diffusion. Moreover, as a monolithic electrode/electrocatalyst system, the electron conduction can be effective facilitated and eliminates the use of substrate binders. Compared to bulk Ni_6Fe_4 printed by laser-based manufacturing, the nanoporous NiFe electrode exhibits an improved electrocatalytic activity with an OER current density of 100 mA/cm^2 at 442 mV overpotential in 1 M KOH aqueous solution. Preparing the nanoporous NiFe electrocatalyst by dealloying laser-based manufactured alloys displays great potential for developing self-stand nanoporous electrode for energy conversion reactions, and provides new insights on electrode structure and composition engineering, which may pave a new way for the efficient and effective development of electrocatalyst.

Fourthly, Ni, Fe with other earth-abundant transition metal based HEAs, including FeNiMnCrCu and FeCoNiCrAl, synthesized via arc melting, were for the first time applied as the electrocatalyst material toward OER. A good combination of reaction favorable elements can significantly boost the catalytic performance of transition metal based electrocatalyst. Remarkably, the FeNiMnCrCu HEA exhibits an excellent activity and stability toward OER, which is comparable to Pt electrocatalyst, and much better than FeCoNiCrAl HEA. These results suggest the HEA materials are very promising as next generation functional materials, especially in chemistry and electrochemistry area.

7.2 Future Work

In this dissertation, laser-based manufacturing has been successfully applied for printing single layer electrocatalyst for oxygen evolution reactions. As a prototyping manufacturing method, laser-based manufacturing has a great potential in becoming an established fabrication technique to develop 3D structured electrocatalyst for various electrochemical systems. In the future, the following works are suggested.

1. Develop micro-scale 3D structured electrode by laser-based manufacturing with different structure and morphology design to maximize the catalytic active area and facilitate electron and mass transfer.

2. Develop nanoporous structure on 3D features of the selective laser printed electrodes by various techniques, such as chemical vapor deposition, dealloying, electrodeposition to further improve the performance of the electrocatalyst to nanometer scale.

3. Improve the alloy composition by researching other earth-abundant metals or include other functional materials, such as ceramic, carbon-based materials, to facilitate advanced structure design.

4. Electrocatalyst for other energy related reactions, such as hydrogen evolution reactions, CO_2 reduction reaction are suggested to be developed by laser-based manufacturing.

VITA

Xiaodan Cui was born and grew up in Dandong, Liaoning, China. In the year of 2012, Xiaodan graduated with a B.S. degree in Chemical Engineering from Tianjin University in China. During her undergraduate study, she participated in summer research program in University of Melbourne in 2011. In 2012, she turned to graduate school and joined the Advanced Material Research Lab at University of Illinois at Chicago. Her research was focusing on thin film material fabricated by atomic layer deposition. Xiaodan graduated with a M.S. degree in Chemical Engineering in 2015. She joined the Department of Mechanical and Industrial Engineering at Louisiana State University (LSU) in 2015. Xiaodan has received honors during her Ph.D. study at LSU including Graduate Enrichment Award and Graduate Travel Award. During her graduate study at LSU, Xiaodan has gained research expertise in the areas of advanced manufacturing, laser-based manufacturing and catalysis. Xiaodan expects to graduate with the degree of Ph.D. in Mechanical Engineering from LSU in Fall 2018.